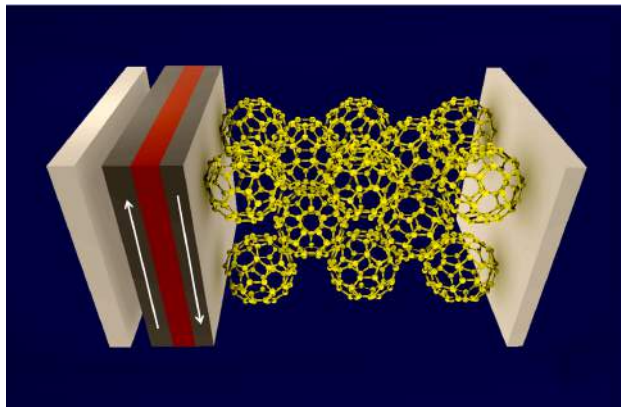


eman ta zabal zazu



Universidad del País Vasco Euskal Herriko Unibertsitatea

# Spintronic devices based on fullerene $C_{60}$



Marco Gobbi

PhD Thesis

Thesis Supervisor: Prof. Luis E. Hueso

2013









**AUTORIZACION DEL/LA DIRECTOR/A DE TESIS  
PARA SU PRESENTACION**

Dr/a. Luis E. Hueso con N.I.F. \_\_\_\_\_

como Director/a de la Tesis Doctoral: Spintronic devices based on fullerene C<sub>60</sub>

realizada en el Departamento Física de Materiales

por el Doctorando Don/ña. Marco Gobbi

autorizo la presentación de la citada Tesis Doctoral, dado que reúne las condiciones necesarias para su defensa.

En Donostia-San Sebastián a 18 de Marzo de 2013

EL/LA DIRECTOR/A DE LA TESIS

Fdo.: Luis E. Hueso



**AUTORIZACION DEL PONENTE DE TESIS  
PARA SU PRESENTACION**

Dr/a. **Prof. Jose M. Pitarke**

---

como Ponente de la Tesis Doctoral: **Spintronic devices based on fullerene C<sub>60</sub>**

---

realizada en el Departamento **Física de Materiales**

---

por el Doctorando Don/ña. **Marco Gobbi** ,

y dirigida por el Dr./a **Luis E. Hueso**

---

autorizo la presentación de la citada Tesis Doctoral, dado que reúne las condiciones necesarias para su defensa.

En \_\_\_\_\_ a \_\_\_\_\_ de \_\_\_\_\_ de \_\_\_\_\_

EL PONENTE DE LA TESIS

Fdo.: Prof. Jose M. Pitarke



**CONFORMIDAD DEL DEPARTAMENTO**

El Consejo del Departamento de **Física de materiales** \_\_\_\_\_

\_\_\_\_\_

en reunión celebrada el día \_\_\_\_ de \_\_\_\_\_ de \_\_\_\_ ha acordado dar la conformidad a la admisión a trámite de presentación de la Tesis Doctoral titulada: \_\_\_\_\_

**Spintronic devices based on fullerene C<sub>60</sub>**

\_\_\_\_\_

dirigida por el/la Dr/a. **Luis E. Hueso** \_\_\_\_\_

\_\_\_\_\_

y presentada por Don/ña. **Marco Gobbi** \_\_\_\_\_

ante este Departamento.

En \_\_\_\_\_ a \_\_\_\_ de \_\_\_\_\_ de \_\_\_\_\_

Vº Bº DIRECTOR/A DEL DEPARTAMENTO    SECRETARIO/A DEL DEPARTAMENTO

Fdo.: \_\_\_\_\_

Fdo.: \_\_\_\_\_



**ACTA DE GRADO DE DOCTOR O DOCTORA**  
**ACTA DE DEFENSA DE TESIS DOCTORAL**

DOCTORANDO/A DON/DÑA. **Marco Gobbi** \_\_\_\_\_

TITULO DE LA TESIS: **Spintronic devices based on fullerene C<sub>60</sub>**  
\_\_\_\_\_  
\_\_\_\_\_

El Tribunal designado por la Subcomisión de Doctorado de la UPV/EHU para calificar la Tesis Doctoral arriba indicada y reunido en el día de la fecha, una vez efectuada la defensa por el doctorando y contestadas las objeciones y/o sugerencias que se le han formulado, ha otorgado por \_\_\_\_\_ la calificación de:  
*unanimidad ó mayoría*

--

*APTO o NO APTO*

Idioma/s de defensa (en caso de más de un idioma, especificar apartados o porcentaje defendido en cada idioma): \_\_\_\_\_

En \_\_\_\_\_ a \_\_\_\_\_ de \_\_\_\_\_ de \_\_\_\_\_

EL/LA PRESIDENTE/A,

EL/LA SECRETARIO/A,

Fdo.: \_\_\_\_\_  
Dr/a: \_\_\_\_\_

Fdo.: \_\_\_\_\_  
Dr/a: \_\_\_\_\_

VOCAL 1º,

VOCAL 2º,

VOCAL 3º,

Fdo.: \_\_\_\_\_ Fdo.: \_\_\_\_\_ Fdo.: \_\_\_\_\_  
Dr/a: \_\_\_\_\_ Dr/a: \_\_\_\_\_ Dr/a: \_\_\_\_\_

EL/LA DOCTORANDO/A,

Fdo.: \_\_\_\_\_



## Resumen

En esta tesis, se presentan los resultados de la investigación llevada a cabo en 4 años de doctorado. El tema de la tesis, que se compone de cinco capítulos, es la fabricación de dispositivos de espintrónica basados en capas delgadas de moléculas de fullereno C<sub>60</sub>.

El primer capítulo presenta el campo de la espintrónica. A partir de los conceptos básicos, reviso los acontecimientos más importantes en el campo, centrándome en particular en por qué los materiales a base de carbono son atractivos para aplicaciones de espintrónica.

La espintrónica es un área de investigación relativamente nueva con el fin de explotar el espín del electrón en dispositivos de estado sólido. El control y manipulación del espín agrega un grado de libertad a la electrónica de estado sólido, lo que permite el diseño de dispositivos con nuevas propiedades. Por esta razón, la espintrónica hace un amplio uso de metales ferromagnéticos, que poseen intrínsecamente un número diferente de electrones con espín hacia arriba y hacia abajo. El dispositivo espintrónico prototípico se denomina válvula de espín, y está compuesto por un material no-magnético intercalado entre dos capas de metales ferromagnéticos (figura 1.1 (a) y (b)). Su importancia reside en el hecho de que su resistencia eléctrica depende de la alineación relativa de las magnetizaciones de las dos capas ferromagnéticas. En la mayoría de los casos, la resistencia es menor cuando las magnetizaciones se alinean paralelas (figura 1.1 (a)), y más alto cuando son antiparalelas (figura 1.1 (b)). La característica más importante de los dispositivos se denomina magnetoresistencia, y se define como:

$$MR = \frac{R_{ap} - R_p}{R_p} \quad (1)$$

donde  $R_{ap}$  ( $R_p$ ) es la resistencia del dispositivo en estado antiparalelo (paralelo). De este modo, la magnetización, que es una cantidad relacionada con el espín, se convierte en una variación de resistencia, que genera un voltaje compatible con la electrónica convencional.

En combinación con los metales ferromagnéticos, se utilizan otros materiales como capa intermedia en los dispositivos de espintrónica. Las cabezas de lectura de los discos duros modernos funcionan en la base de uniones túnel magnéticas. En estos dispositivos, la capa intermedia que separa los dos metales FM es una capa aislante ultradelgada. El espesor de la barrera es tan delgado (típicamente por debajo de  $t < 2$  nm) que los electrones pueden pasar por efecto túnel desde un electrodo al otro. En estos dispositivos, se puede obtener magnetoresistencia muy alta (hasta 200% a temperatura ambiente).

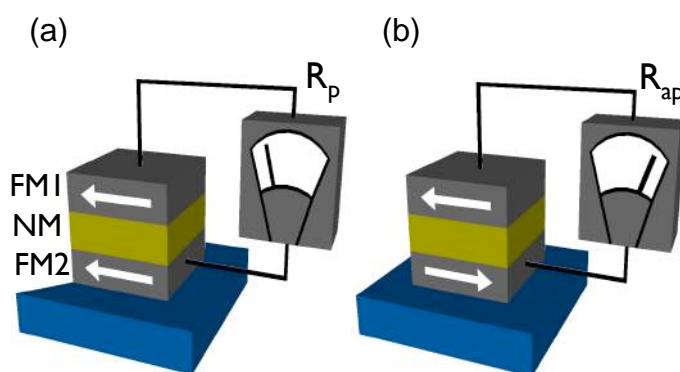


Figura r.1. Estructura de un spin-válvula: dos capas ferromagnéticas están separadas por una capa no magnética. La resistencia eléctrica de la tricapa depende de la orientación relativa de la magnetización, paralela (a) o antiparalela (b).

El efecto de magnetoresistencia se observó por primera vez en válvulas de espín metálicas, ya que la fabricación de multicapas metálicas era tecnológicamente menos difícil que la fabricación de barreras túneles ultra delgadas. En los metales, la información de espín puede viajar por largas distancias (en el orden de  $1 \mu\text{m}$ ). Con modernas técnicas de litografía, se ha demostrado que es posible manipular el espín de forma más avanzada que la simple válvula de espín vertical.

Uno de los retos más intrigantes en espintrónica es hacer que sea compatible con la industria de semiconductores, para añadir el grado de libertad de espín en dispositivos electrónicos. Por ejemplo, la producción de un transistor de efecto de spin-campo podría combinar el efecto de magnetoresistencia con el normal funcionamiento del transistor. Sin embargo, la producción de dispositivos de espintrónica basados en semiconductores se ha demostrado muy complicada.

En este contexto, el carbono se está convirtiendo en un material prometedor para nuevas aplicaciones espintrónica. Los mecanismos de scattering del espín en materiales a

base de carbono son débiles, por lo que la vida del espín es larga. Por lo tanto, ofrecen amplias posibilidades para la manipulación avanzada del espín.

En efecto, los nanotubos de carbono y el grafeno son plantillas ideales para los dispositivos donde la información de espín tiene que viajar largas distancias, gracias a su alta velocidad de Fermi y su movilidad. Por otro lado, las moléculas son útiles para modificar las superficies de los metales ferromagnéticos, y se han observado varias válvulas de espín con elevadas magnetoresistencias.

Esta tesis se centra en la producción de dispositivos de espintrónica basados en películas delgadas de fullereno  $C_{60}$ . El fullereno  $C_{60}$  es particularmente adecuado para dispositivos de espintrónica, ya que puede ser sublimado en ultra alto vacío, in situ con materiales ferromagnéticos. Además,  $C_{60}$  ha sido ampliamente estudiado y utilizado también en la electrónica orgánica estándar, especialmente como semiconductor de tipo n en transistores de efecto de campos y mezclados con polímeros como aceptor de electrones para células solares.

En el capítulo 2 se describen los equipos empleado para fabricar y caracterizar los dispositivos estudiados en esta tesis. La mayoría de los equipos fueron adquiridos recientemente en el comienzo de mi proyecto de tesis doctoral, por lo cual una parte importante de mi tesis doctoral fue su puesta en marcha y optimización. He sido el principal usuario y entrenador para el evaporador Theva y la probe station Lakeshore.

Todos los dispositivos que se describen en esta tesis se han fabricado en un sistema evaporador de ultra alto vacío fabricado por Theva, compuesto por dos cámaras principales y un load lock. Una de las cámaras principales se dedica a la deposición de los metales por haz de electrones y la otra se utiliza para la evaporación térmica de las moléculas. En el load lock, se pueden realizar tratamientos con plasma de oxígeno o argón. Cada cámara está equipada con un sistema de shadow masks que permite de modelar dispositivos sin pasos litográficas.

Las mediciones eléctricas presentadas en esta tesis se han realizado en una de las dos similares estaciones de sondas Lakeshore. Las dos estaciones de sonda tienen la capacidad de realizar mediciones en vacío con un campo magnético aplicado y a bajas temperaturas. La presión base a la temperatura ambiente está por debajo de  $p = 2 \times 10^{-5}$  mbar, lo suficientemente bajo como para evitar la degradación rápida de las capas moleculares. El campo magnético se aplica en el plano de la muestra, y tiene un valor máximo  $H = 0.6$  T. Durante la medición, se puede enfriar la muestra a 4,9 K. Las mediciones eléctricas se realizan con un Keithley 4200 equipado con tres unidades de medición/fuente, dos de los cuales cuentan con un amplificador de corriente con resolución nominal en el rango de sub-femto amperios.

Asimismo, el Microscopio de Fuerza Atómica y la Difractómetro de Rayos X se han utilizado ampliamente durante esta tesis, pero por estos equipos he sido un usuario normal.

El capítulo 3 se centra en la caracterización de las películas delgadas de los diferentes materiales utilizados en esta tesis. Todos los dispositivos que se describen a lo largo de esta tesis están compuestos por la combinación entre películas de moléculas de  $C_{60}$  y películas de diferentes metales. En particular, solo cuatro metales se han utilizado: Aluminio, Cobre, Cobalto y la aleación  $Ni_{79}Fe_{21}$ , conocida como Permalloy (Py).

En primer lugar, los metales han sido caracterizados en términos de resistividad y rugosidad. La resistividad es un buen indicador de la pureza del metal. La rugosidad es crucial para evitar pin holes en los dispositivos verticales con capas ultradelgadas. La calidad de las películas de Al y Cu aumenta cuando se depositan con una alta velocidad de deposición sobre un sustrato a temperatura baja. Para las películas ferromagnéticas, la temperatura del sustrato no es crucial. Sus campos coercitivos pueden medirse eléctricamente a través del efecto de magnetoresistencia anisótropa.

En segundo lugar, me centro en las bicapas  $C_{60}/Py$ . Las películas de  $C_{60}$  crecen relativamente planas tanto en Py y sustratos de  $SiO_2$ , y estimamos que una película de  $C_{60}$  de 5 nm de espesor cubre completamente la superficie por debajo sin dejar poros y por lo tanto puede ser utilizado en un dispositivo vertical. Además, la película de  $C_{60}$  es robusta frente a la deposición del electrodo de metal superior, y que solo hay una capa muy fina (1-2 nm) de materiales entremezclados en la interfaz  $C_{60}/Py$ . Por último, las propiedades magnéticas de Py no se ven afectadas por la secuencia de deposición, y una capa de Py con 5 nm de espesor encima de una capa de  $C_{60}$  mantiene sus propiedades magnéticas intactas.

En el capítulo 4 me centro en las válvulas de espín basadas en  $C_{60}$ . En estos dispositivos, el Fullerenos se utiliza como la capa intermedia entre dos electrodos ferromagnéticos, Cobalto y Permalloy.

La geometría del dispositivo es muy simple. Los dispositivos están definidos por la deposición de pilas  $Co/AlO_x/C_{60}/Py$  a través de máscaras de sombra. En cada chip, dos dispositivos se quedan únicamente con la capa de  $AlO_x$  sin  $C_{60}$  y se utilizan como referencias. Los dispositivos de referencia sin  $C_{60}$  se han caracterizado y optimizado. Magnetoresistencia relativamente alta (15%) se ha medido en dispositivos con la estructura  $Co / AlO_x / Py$ . Sin embargo, en lugar de utilizar barreras optimizado  $AlO_x$  preferimos emplear barreras defectuosas con baja resistencia donde no se mide magnetoresistencia de túnel. De esta manera, se evitan posibles artefactos causados por una barrera resistente  $AlO_x$  en las válvulas de espín con  $C_{60}$ .

En cuanto a los dispositivos de  $C_{60}$ , se presenta la caracterización de los dispositivos eléctricos con diferentes espesores de la capa de  $C_{60}$ . En primer lugar, la resistencia de los dispositivos aumenta exponencialmente con el espesor de la película  $C_{60}$  en el rango de 5-25 nm. El mecanismo de transporte de carga es de acuerdo con un régimen de túnel multi-paso.

A continuación, se presenta la caracterización magnética de los dispositivos. Magnetoresistencia significativa (en exceso de 5%) se mide para los diferentes espesores de la capa intermedia de  $C_{60}$  (con grosor entre 5 nm y 28 nm) hasta alto voltaje aplicado ( $\sim 1$  V), como enseñando in figura r.2. La demostración de magnetoresistencia en este tipo de dispositivos implica que los espines de los electrones no se pierden en la capa de  $C_{60}$ , que actúa como una capa de transporte de espín.

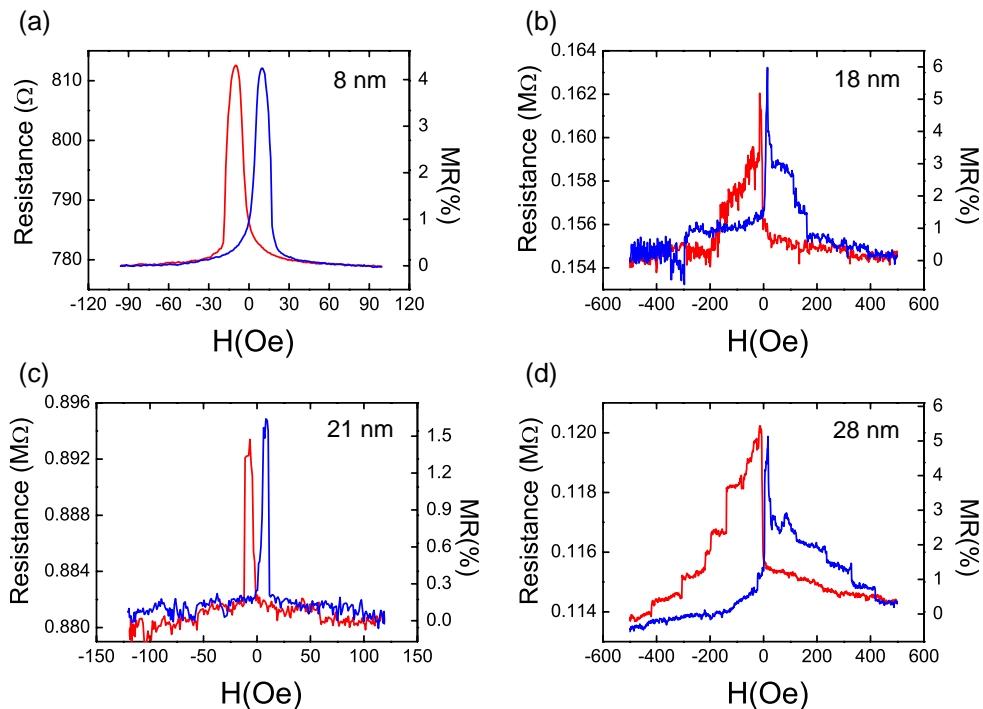


Figura r.2. Magnetoresistencia medida con un voltaje de polarización  $V = 10$  mV para las válvulas de espín basadas en  $C_{60}$  con diferente espesor: (a) 8 nm, (b) 18 nm, (c) 21 nm, (d) 28 nm.

El capítulo 5 se centrará en transistores túnel magnéticos basados en  $C_{60}$ . En tales dispositivos, la corriente se inyecta desde el emisor (un metal no magnético) en una base compuesta por una spin-válvula metálica. Los electrones se inyectan con energía por encima del nivel de Fermi de la base, por lo tanto son “caliente”. Una capa gruesa

de  $C_{60}$  se utiliza como semiconductor para coleccionar los electrones que no hayan perdido su energía en la base. Los eventos de dispersión que causan la atenuación de la energía de los electrones calientes dependen del espín en metales ferromagnéticos. Por esta razón, la interfaz ferromagnético metal / semiconductor actúa como un filtro por espines. Basado en este efecto, la cantidad de corriente que entra en la capa de  $C_{60}$  depende de la alineación relativa de las magnetizaciones de los electrodos, y es casi exactamente 0 en el caso antiparalelo (figura r.3 (a) y (b)).

La caracterización eléctrica del dispositivo permite una medición precisa de la alineación de nivel de energía en la interfaz metal/ $C_{60}$ , debido a que los electrones comienzan a fluir en el  $C_{60}$  cuando la tensión de base emisor está por encima de la barrera de energía en la interfaz metal / semiconductor. En particular, la barrera de energía entre el Fullerenos y el Permalloy es de 1 eV, con pequeñas variaciones en diferentes dispositivos.

Desde el punto de vista magnético, una variación enorme (hasta 89%) en la corriente del colector se mide a temperatura ambiente en un barrido del campo magnético (figura r.3 (c)). Además, esta variación puede ser mejorada por la aplicación de un voltaje apropiado en el colector, llegando en principio a un valor infinito debido a una corriente insignificante en el estado desactivado.

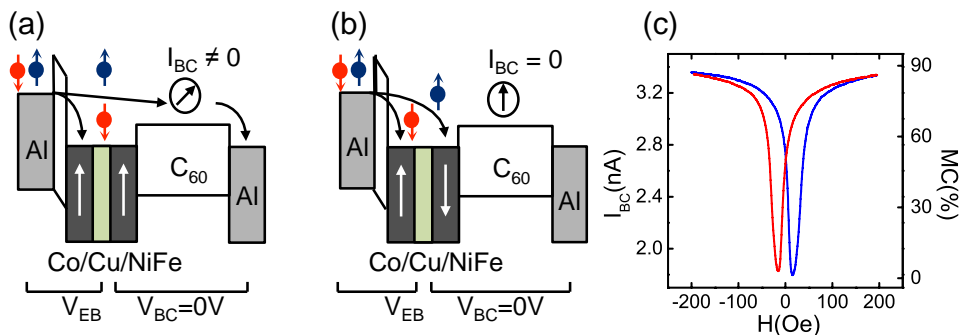


Figura r.3. Diagrama de las energías de un transistor magnético de efecto túnel, cuando la válvula de espín está en estado paralelo (a) y en estado antiparalelo (b). Suponiendo un efecto de filtro de espín perfecto, la corriente entra en el colector  $C_{60}$  sólo cuando la válvula de espín está en el estado paralelo. (c) Efectivamente, se mide una gran variación en la corriente que llega al colector dependiendo del estado de la válvula de espín.

Además, hemos estudiado el efecto de parámetros externos en las características de los dispositivos. En primer lugar, la dependencia de la temperatura de los dispositivos es análoga a la dependencia de la temperatura de los dispositivos similares basados en

semiconductores inorgánicos. En segundo lugar, el grado de oxidación de la superficie de Py cambia la barrera Py/C<sub>60</sub>. En tercer lugar, una iluminación externa aumenta la cantidad de corriente de electrones en caliente de alcanzar el electrodo superior. En cuarto lugar, el efecto de un voltaje adecuado también puede aumentar la cantidad de corriente de electrones en caliente alcanzando el electrodo colector.

En el capítulo 6, resumo algunos resultados recientes, siguiendo las directrices de la investigación de mi último año de doctorado. En efecto, la estructura de la simple válvula de espín estudiada en el capítulo 4 tiene algunas limitaciones para el estudio del transporte de espín en C<sub>60</sub>. En primer lugar, no está claro hasta qué punto los resultados obtenidos en las válvulas de espín orgánicos puede ser descrito con el modelo estándar de inyección, transporte y detección de espín. En segundo lugar, las válvulas de espín están sujetas a artefactos causados por la penetración de la capa superior de metal en la capa de C<sub>60</sub>, y de hecho experimentos de control son necesarios. Presento la idea de una geometría más sofisticado que permita la inyección eléctrica y la detección de corriente de espín polarizado en C<sub>60</sub>. Esta geometría se basa en la serie de dos transistores parecidos a los que han sido presentados en el capítulo 5. Como resultado parcial, hemos comparado transistores con diferentes metales utilizados como base, descubriendo que en la interfaz cobalto/fullereno no se forma una barrera de energía que pueda ser utilizada en un transistor.



## Table of contents

Summary .....	5
<b>1. Introduction</b>	
<b>1.1 Spintronics .....</b>	<b>9</b>
<b>1.2 Materials for spintronics .....</b>	<b>12</b>
1.2.1 Ultra-thin insulating barrier .....	12
1.2.2 Metals .....	15
1.2.3 Semiconductors.....	19
<b>1.3 Carbon-based materials .....</b>	<b>21</b>
1.3.1 Carbon nanotubes and Graphene.....	21
1.3.2 Organic semiconductors .....	23
<b>1.4 Our approach to carbon spintronics.....</b>	<b>26</b>
<b>1.5 References .....</b>	<b>28</b>
<b>2. Experimental Methods</b>	
<b>2.1 Dual chamber Evaporator.....</b>	<b>35</b>
2.1.1 Load lock.....	37
2.1.2 Metal chamber .....	37
2.1.3 Organic chamber .....	39
<b>2.2 Probe Station .....</b>	<b>40</b>
<b>2.3 Atomic force microscopy and X-rays reflectivity .....</b>	<b>42</b>
2.3.1 Atomic Force Microscopy .....	42
2.3.2 X-Rays Reflectivity .....	44
<b>2.4 References: .....</b>	<b>46</b>

### 3. Material Characterization

3.1 Metal characterization.....	49
3.1.1 Non-magnetic metals .....	51
3.1.2 Magnetic metals .....	55
3.2 Characterization of C <sub>60</sub> /Py bilayers .....	57
3.2.1 AFM Characterization.....	58
3.2.2 XRR Characterization.....	60
3.2.3 Magnetic Characteriation.....	62
3.3 Conclusions .....	65
3.4 References .....	65

### 4. C<sub>60</sub> based spin valves

4.1 Device geometry .....	69
4.2 AlO <sub>x</sub> magnetic tunnel junction .....	72
4.3 Electrical transport in C <sub>60</sub> -based spin valve.....	75
4.4 Magnetoresistance in C <sub>60</sub> based spin valves .....	79
4.5 Conclusions .....	82
4.6 References .....	82

### 5. C<sub>60</sub> based magnetic tunnel transistors

5.1 Device operation and structure.....	85
5.2 Device Characterization .....	89
5.2.1 Electrical characterization .....	89
5.2.2 Magnetic Characterization .....	91
5.3 Effects of external parameters .....	94
5.3.1 Temperature dependence.....	94
5.3.2 Dependence on the evaporator base pressure .....	97
5.3.3 Bias and light dependence .....	99
5.4 Conclusions .....	101

5.5 References .....	101
<b>6. Beyond the spin valve structure</b>	
6.1 Limitations of the spin-valve structure .....	103
6.2 Towards the hot-electron spin valve .....	106
6.2.1 Permalloy base transistors .....	109
6.2.2 Cobalt base transistor .....	113
6.3 Conclusions .....	114
6.4 References: .....	115
7. List of publications .....	117
8. Acknowledgements .....	119

---

## Summary

Spintronics, or the possibility of performing electronics with the spin of the electron, has been fundamental for the exponential growth of digital data storage which has occurred in the last decades. Indeed, hard-disk drives read-heads are the maximum exponent of what is currently being called first-generation spintronic devices. Current read-heads, although technologically very complex, are scientifically based simply on the magnetoresistance effect, for which the electrical resistance of a device changes under the application of an external magnetic field. A tunnel magneto-resistive vertical spin valve is composed of two ferromagnetic layers separated by a thin (around 1 nm) insulating layer, and the resistance of the structure can be switched between two different values upon the application of a magnetic field capable of rotating the magnetization vector of the ferromagnetic layers from parallel to antiparallel. For the eventual success of a second-generation of spintronic devices, more complex mechanisms than the nanometer-distance spin transport in metallic or insulating materials have to be obtained. In particular, coherent spin transport at distances above a few nm and long spin lifetimes are unavoidable requirements for sophisticated spin manipulation at the basis of prototypes of, for example, spin transistors or spin light-emitting diodes.

Carbon based semiconductors have emerged as promising materials for advanced spintronics applications. In this wide class of materials, the spin lifetime is very long, because the spin relaxation mechanisms are extremely weak. On the one hand, graphene and carbon nanotubes are typically characterized by high carrier mobility and long mean free path, so the long spin lifetimes translate into extremely large spin diffusion lengths. Therefore, they are template materials for applications in which the spin signal needs to be conserved over long distances. On the other hand, the combination between ferromagnetic metals and molecules offers the possibility to design new devices with novel functionalities, and to tailor the interfacial spin polarization of ferromagnetic metals.

This thesis presents spintronic devices based on thin films of fullerene  $C_{60}$ . In chapter 1, after introducing spintronics and carbon-based spintronics, I comment on the reasons for choosing  $C_{60}$  as template material for spintronic devices.

In chapter 2, the equipment used to fabricate and characterize the devices under study in this thesis is described. All the samples studied in this thesis were produced in a

dual chamber evaporator, with one chamber for the metal deposition and one chamber for the organic deposition. The evaporator was recently acquired at the beginning of my PhD project, so an important part of my PhD was its setting up and optimization, which also required in-house hardware modifications. I describe in detail also the probe station used for the device characterization. Another paragraph shortly describes the Atomic Force Microscope and the X-Rays Diffractometer, which have been extensively used during this thesis.

In chapter 3, I focus on the characterization of the thin films of the different materials used in this thesis. All the devices described throughout this thesis are composed by the combination between films of  $C_{60}$  molecules and films of different metals. In particular, four metals have been used: Aluminum, Copper, Cobalt and the  $Ni_{79}Fe_{21}$  alloy, known as Permalloy (Py). First, I describe the characterization of metals in terms of resistivity and roughness. The resistivity is a good indicator of the metal purity. The roughness is crucial for avoiding pinholes in vertical devices with ultrathin layers. Second, I will expose a detailed study about  $C_{60}$ /Py bilayers. The  $C_{60}$  films grow relatively smoothly on both Py and  $SiO_2$  substrates, and we estimate that a 5-nm-thick  $C_{60}$  film covers completely the surface underneath without leaving pinholes and can be therefore used in a vertical device. Furthermore, the  $C_{60}$  film is robust against the deposition of the top metal electrode, being the intermixing layer of only 1–2 nm at the  $C_{60}$ /Py interface. Finally, the magnetic properties of Py are not affected by the deposition sequence, and that a 5-nm-thick Py layer on top of a  $C_{60}$  layer keeps its magnetic properties intact.

In chapter 4, I focus on the prototypical spintronic device, the spin valve, based on  $C_{60}$ . In this study, a  $C_{60}$  layer is inserted between two ferromagnetic electrodes, above a seed layer of  $AlO_x$ . The devices can be used to gain information about the spin transport in the  $C_{60}$  film, because magnetoresistance is only measured if the spin coherence is not lost in the  $C_{60}$  film. I present the electrical and magnetic characterization of devices with different  $C_{60}$  thicknesses, showing that the transport mechanism is in agreement with a multi-step tunnelling regime. Significant magnetoresistance (in excess of 5%) is measured for the different thicknesses of the  $C_{60}$  interlayer (from 5 nm to 28 nm) up to high applied biases ( $\sim 1$  V), demonstrating robust spin transport through  $C_{60}$  molecules.

Chapter 5 focuses on another (more sophisticated) spintronic device based on  $C_{60}$ , the magnetic tunnel transistors (MTT). In such devices, a thick  $C_{60}$  layer is used as the semiconducting collector of a metal base transistor with a metallic spin valve base. First, I explain how the device allows an accurate measurement of the energy level alignment at the metal/ $C_{60}$  interface. Afterwards, I show that the performances of the  $C_{60}$  magnetic tunnel transistor described in this thesis are similar to those of the reported devices based on conventional inorganic semiconductors. Indeed, a huge (up to 89%)

change in the collector current is measured at room temperature in a magnetic field sweep. Moreover this variation can be enhanced by the application of a proper voltage at the collector, reaching in principle an infinite value due to a negligible current in the off-state. I also describe how different parameters affect the performances of the device. In particular I focus on the effect of different resistance of the  $C_{60}$  layer, temperature, bias voltage and external illumination.

In the last chapter, I summarize some recent results and give an outlook on the ongoing research in our laboratory. I explain that the simple spin valve structure of chapter 4 has some limitations for the study of spin transport in  $C_{60}$ . I also show how another structure based on the tunnel transistor of chapter 5 might allow further spin manipulation, presenting some partial results towards its fabrication.

---

## Chapter I

### Introduction

*In this chapter I introduce spintronics and highlight the reasons why carbon-based materials are promising candidates for novel spintronic applications.*

*In section 1, I first describe the prototypical spintronic device, the spin valve, and introduce the concepts of spin-polarized current and magnetoresistance, which are the basis of this thesis. In section 2, I review the different materials employed in combination with ferromagnetic metals in spintronic devices: ultrathin insulators, metals and semiconductors. I introduce other concepts that will be widely used in the next chapters, such as the spin injection and detection.*

*In section 3, I focus on carbon-based materials for spintronics. I explain that there are two distinct classes inside carbon-based materials, one being composed by graphene and carbon nanotubes, and the other one by organic semiconductors. For different reasons, both categories possess characteristics that make them appealing for spintronic applications.*

*In section 4, I describe our approach to the field. I explain why we chose  $C_{60}$  to produce spintronic devices, underling that  $C_{60}$  behaves either as a thin insulating film or as a conventional inorganic semiconductor in different devices.*

#### I.1 Spintronics

Spintronics is a relatively new research area with the aim of exploiting the electron spin in solid state devices [1]. Indeed, the control and manipulation of the spin adds a degree of freedom to solid-state electronics, allowing the design of devices with novel properties. In this sense, spintronics goes beyond conventional electronics, that only takes advantage of the electron charge  $e$ .

The electron spin  $S$  is a quantized angular momentum intrinsic to electrons. In a given direction it can only take on the values  $s = \hbar/2$  or  $s = -\hbar/2$ , often visualized as “spin

## 1.1 Spintronics

up” and “spin down”. Associated with the spin angular momentum, electrons possess a magnetic momentum

$$\boldsymbol{\mu} = \frac{g_s e}{2m} \boldsymbol{S} \quad (1)$$

where  $e$  and  $m$  are the electron charge and mass, and  $g_s \approx 2$  is the electron  $g$ -factor. The spin angular momentum is not an accessible quantity in conventional electronics. Therefore, the problem is how to translate it into an output compatible with conventional electronics, and how to actually profit of the extra degree of freedom.

Spintronics makes wide use of ferromagnetic (FM) metals, because they intrinsically possess a different number of electrons with spin up and spin down. Indeed, in FMs, the electronic bands split into spin up and spin down sub-bands because of the exchange interaction [2]. Figure 1.1(a) shows a schematic spin-split density of states  $N(E)$  of a typical FM, with different density of states  $N_{\uparrow}(E) \neq N_{\downarrow}(E)$ . One of the two spin subbands is favored in energy and is almost fully occupied, ( $N_{\uparrow}(E)$  in figure 1.1(a)), while the other one is only partially occupied. In the overall, more electrons possess the favored spin orientation ( $N_{\uparrow}(E)$  in figure 1.1(a)) and are called majority electrons; the spin-down electrons ( $N_{\downarrow}(E)$  in figure 1.1(a)) are called minority electrons. This unbalance in the spin populations gives rise to the macroscopic magnetization of the FM, which is due to the sum of all the magnetic momenta  $\boldsymbol{\mu}$  associated to each unpaired spin.

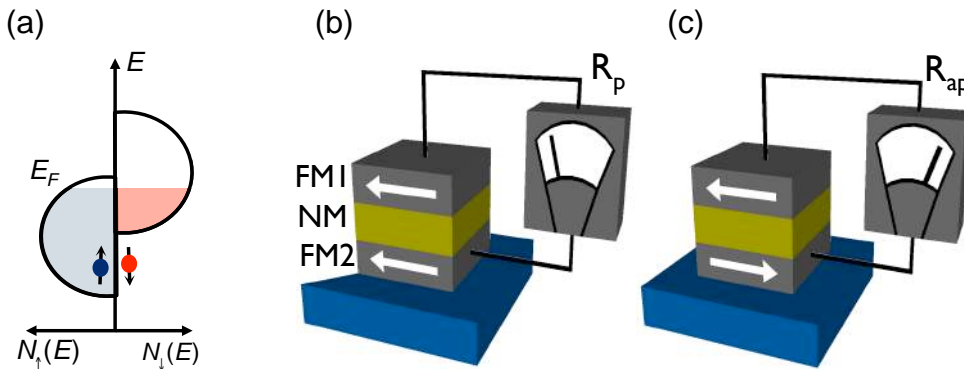


Figure 1.1. (a) Spin split density of states for a ferromagnetic metal. (b) and (c) Structure of a spin-valve: two ferromagnetic layers are separated by a non magnetic layer. The electrical resistance of the trilayer depends on the relative orientation of the magnetization, parallel (b) or antiparallel (c)

Also at the Fermi energy, the number of majority and minority electrons is unequal in FMs,  $N_{\uparrow}(E_F) \neq N_{\downarrow}(E_F)$  [2]. In figure 1.1(a),  $N_{\uparrow}(E_F) < N_{\downarrow}(E_F)$ , which is the case for Ni, while

for Co and Fe the opposite would be true,  $N_{\uparrow}(E_F) < N_{\downarrow}(E_F)$  [3]. The electrons close to the Fermi level are particularly important, because they carry the electrical current [2], which in turn is spin polarized. The total current density  $j$  can be written as the sum of two components  $j = j_{\uparrow} + j_{\downarrow}$ , one for each spin subband, which are usually considered as independent parallel channels. The current spin polarization  $SP$  can be defined as

$$SP = \frac{j_{\uparrow} - j_{\downarrow}}{j_{\uparrow} + j_{\downarrow}} \quad (2)$$

Having a look at figure 1.1(a), one would naively conclude that the current  $SP$  should be negative, because at the Fermi energy  $N_{\uparrow}(E_F) < N_{\downarrow}(E_F)$ , for Ni at least. Actually, not *all* the electrons at the Fermi energy contribute equally to the current transport, so even if  $N_{\uparrow}(E_F) < N_{\downarrow}(E_F)$ , it might be that  $j_{\uparrow} > j_{\downarrow}$  [3]. Therefore, the spin polarization of the electrical current depends in a non-trivial way on the density of states.

FMs are ideal materials for spintronics, because they have the capability to introduce uncompensated spins in electronics. The simplest spintronic device is called spin valve (SV) [1], and is a trilayer composed by a non-magnetic (NM) thin film sandwiched between 2 FM layers (figure 5.1. (b) and (c)). Its importance lies in the fact that its electrical resistance depends on the relative alignment of the magnetizations of the two FM layers. In most cases, the resistance is lower when the magnetizations are aligned parallel (P, figure 1.1(b)), and higher when they are antiparallel (AP, figure 1.1(c)). The figure of merit of the device is called magnetoresistance, and is defined as:

$$MR = \frac{R_{ap} - R_p}{R_p} \quad (3)$$

where  $R_{ap}$  ( $R_p$ ) is the resistance of the device in the AP (P) state. In this way, the magnetization, that is a spin-related quantity, is converted into a resistance change, which generates a voltage compatible with conventional electronics.

The SV can be used as a magnetic field sensor, because an external magnetic field changes the relative alignment of the FMs and therefore, the device resistance. For this reason, this device found wide technological applications in magnetic recording. This effect was discovered in 1988 [4,5], and already in 1997 IBM introduced the spin-valve sensors into the read head of hard disks [6]. Nowadays, hard disk heads are still based on a spin-valve like sensor, with figures of merit very different from those of original SVs. The NM interlayer is different: in modern read heads the magnetic layers are separated by an ultrathin insulating layer, while in the original devices by a NM metal.

In the following sections, I will focus on the importance of this NM interlayer. Indeed, the interlayer is not a passive separator, but it has an active role in the determination of the SV characteristics. In section 2, I will review the physical mechanisms behind the magnetoresistive effect in SV with different interlayer materials. In particular, I will highlight that the SV is the easiest spintronic device, but other devices based on more advanced spin manipulation can be conceived and produced. In section 3, I will explain why carbon based materials are particularly attractive for spintronic applications that go beyond the SV.

## 1.2 Materials for spintronics

### 1.2.1 Ultra-thin insulating barrier

The read-heads of modern hard disk drives work on the basis of magnetic tunnel junctions (MTJ) [6]. In these devices, the interlayer separating the two FM metals is an ultra-thin insulating layer. The insulator acts as a potential barrier between the two metallic electrodes. However, the barrier thickness is so thin (typically below  $t < 2\text{nm}$ ) that electrons can tunnel from one electrode to the other. Therefore, upon the application of a bias voltage, a current flows into the device.

The first demonstration of MTJs dates back to the 70s, when Julliere could measure MR<sup>1</sup> in a Fe/Ge/Co SV and proposed a model to explain the resistance change. There three ingredients in the Julliere model:

1. The electron spin is conserved in a tunneling event. Therefore, tunneling can only take place between bands with the same spin orientation (either up or down) in independent channels.
2. The tunneling probability depends on the density of states at the Fermi level in the interfaces of both electrodes. The tunneling is very efficient when it takes place from a high density of filled states in one electrode to a high density of empty states in the other one. As the electrodes are FM, the density of states is spin dependent:  $N_{\uparrow}(E_F) \neq N_{\downarrow}(E_F)$ .
3. Changing the magnetization of a FM electrode corresponds to invert its spin population. Therefore, in the P state, electrons with the same absolute spin

---

<sup>1</sup> In MTJs, the resistance change is usually called "Tunneling Magnetoresistance" to remark the origin of the effect. It is still defined as MR, eq. 2.

orientation are either minority or majority in *both* electrodes; in the AP state, however, electrons with the same spin orientation are minority in one electrode and majority in the other one.

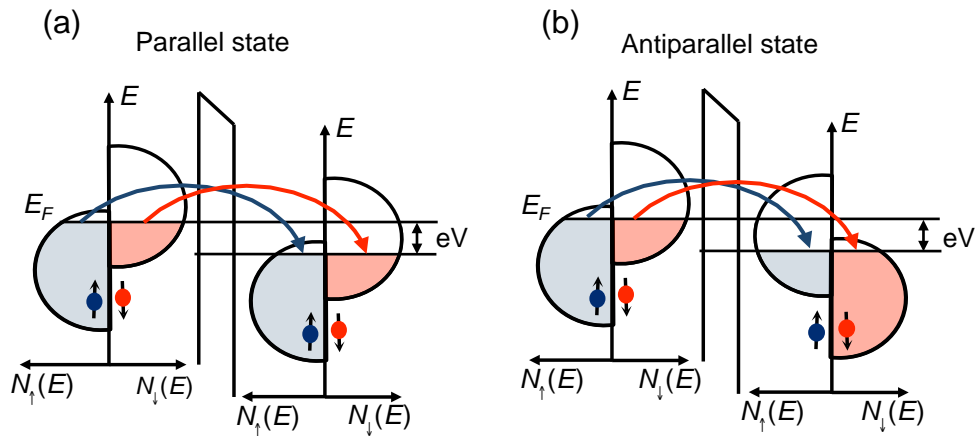


Figure 1.2. Energy diagram for electrons in a magnetic tunnel junction in the parallel state (a) or in the antiparallel state (b). In (a), the resistance is lower because the electrons on the left hand side find more empty states in the right hand side to tunnel to, so that the tunneling is more efficient.

Because of these three effects, the resistance is lower in the P state. In figure 1.2(a) it is clear that in the P state the density of states of spin down electrons at the Fermi energy is high on both sides of the barrier, so that the tunneling is very efficient in this spin channel (red arrow in figure 1.2(a)). On the contrary, in the AP state, such a low resistance channel is closed, because for both spin directions the density of states is high in one electrode but low in the other one; the corresponding tunneling probability is lower and the resistance higher. Once again, the reality is more complicated, because not only the number of electrons at the Fermi energy matters, but also other parameters, as the Fermi velocity [3].

Due to the technological problems connected with the fabrication of an ultra-thin pinholes free insulating layer, a recipe to reproducibly fabricate MTJs was only optimized in 1995 [7,8], 20 years after the pioneering work by Julliere. The new recipe was based on an amorphous  $\text{AlO}_x$  insulating barrier separating standard FM metals (Co, Fe, Ni or their alloys). More details on the fabrication of such MTJs will be given in chapter 4. MR for  $\text{AlO}_x$  MTJs is typically below 40% at room temperature [9], and the highest reported MR ratio for a fully optimized  $\text{AlO}_x$  MTJs is 70% [10]. A breakthrough in the field of MTJs came in 2004, when it was found that very large MR (up to 200% at room

## 1.2 Materials for spintronics

temperature) could be obtained in MTJs based on epitaxial MgO insulating barriers grown onto the surface of Fe(001) [11,12]. Figure 1.3(a) shows the MR of the MgO based MTJ. The resistance of the device is measured in a magnetic field sweep, which induces the reversal of the electrode magnetization. If the magnetizations of the two electrodes flip at different magnetic fields, the SV state can be controllably switched from P to AP state, and accordingly, the MR can be measured. This is a standard way of measuring MR, and will be widely used throughout this thesis.

I point out that for reaching extremely large MR ratios, an MgO barrier with the ultra-high quality in figure 1.3(b) is needed. Indeed, the large MR comes from symmetry selections that only apply if the barrier has the right crystallographic phase and ultra-high quality [13]. Again, I want to underline that the interlayer has an active role in the determination of device performances.

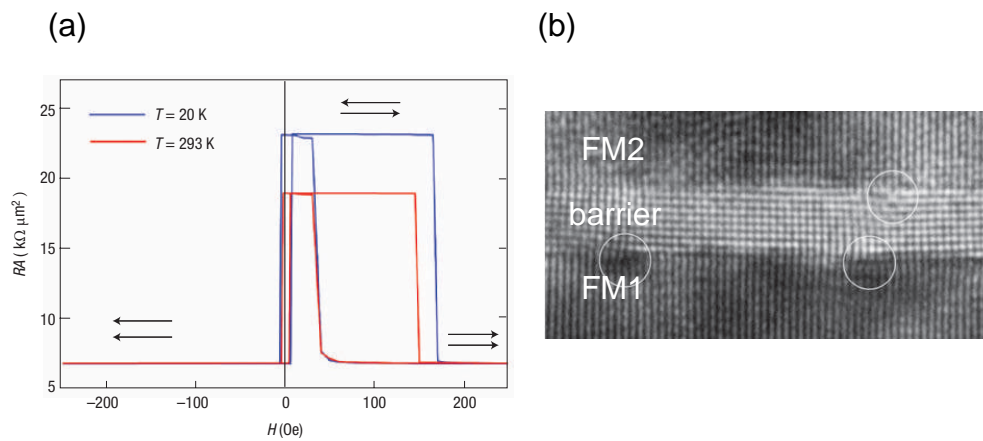


Figure 1.3. (a) MR measured by Yuasa et al. [11] for Fe(001)/MgO(001)/Fe(001) epitaxial MTJs; (b) Electron microscopy image of the MTJ stack. The atomic resolution shows that the crystallinity is almost perfect.

Although MTJs are successfully used as magnetic field sensors, further spin manipulation in this kind of devices is complicated by the nature of the tunneling effect itself. Indeed, the interlayer thickness cannot exceed the few-nm range, leaving no room for more advanced spin manipulation. Besides, electrons do not actually spend time within the barrier. The situation is very different when the interlayer is a metal or a semiconductor, as I will discuss in the next sections.

## 1.2.2 Metals

The MR effect was first observed in metal multilayers [4,5], because the fabrication of metal multilayers was technologically less challenging than the fabrication of ultra thin tunneling barrier. The MR effect measured in metal multilayers is very large (85% in figure 1.4)<sup>2</sup> and attracted immediate interest. Indeed, the effect was discovered in 1988 in devices produced by molecular beam epitaxy [4,5], and, already in 1990, GMR was demonstrated in multilayers made by the faster and simpler technique of sputtering [14]. In 1991, SVs with only two FM layers as in figure 1.1 (b) were demonstrated [15].

For the discovery of the GMR effect in metals, A. Fert and P. Grunberg were awarded with the Nobel prize in 2007. The MR signal measured in a Fe/Cr multilayer is shown in figure 1.4 [4,5]. With no external magnetic field, the magnetizations of the FM layers in the multilayer are aligned antiparallel (AP state), while they are forced to align in the P state when an external field is applied to the device. The device resistance is therefore maximum at 0 field, and decreases when the field is strong enough to align the FM magnetizations (figure 1.4(a)).

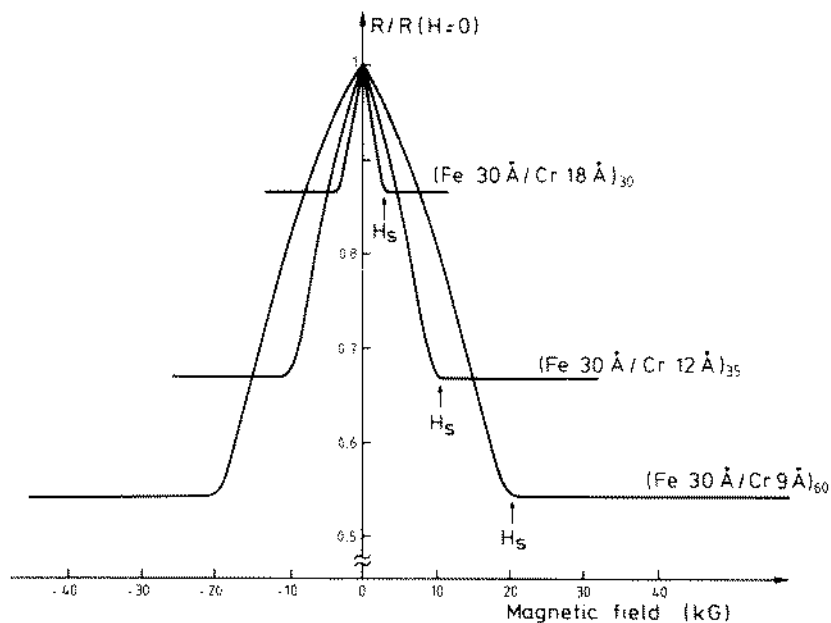


Figure 1.4. First observation of MR in Fe/Cr multilayers. From [4].

<sup>2</sup> For this reason it is called giant magnetoresistance, GMR.

Here, I will briefly discuss the physical mechanism at the basis of the GMR effect in metallic SVs, because some important concepts will apply also to any other material. Following ref. [16], three main contributions affect the MR effect when the current flows perpendicular to the stack.

First, in FM metals the conductance properties are different for the two spin currents  $j_{\uparrow}$  and  $j_{\downarrow}$ . This idea was already proposed by Mott [17], and experimentally verified several decades later [18]. In most GMR experiments, it is assumed that two independent channels with different resistance contribute to the conduction. Analogous to the MTJs case explained in the previous section, one of the two spin orientations encounters low resistance in the two FMs – that means an overall low resistance. In the AP state this low resistance channel disappears, because the two spin directions encounter high resistance in one of the layers, generating a higher resistance of the device.

Second, a similar contribution to the MR effect is expected for spin-dependent scattering at the FM/NM interfaces. In a SV structure as in figure 1.1(b), electrons travelling from one FM to the other encounter two FM/NM interfaces. The scattering at such interfaces is stronger for one spin direction. Again, when the SV is in the P state, there is one spin channel with low interface resistance at both interfaces, making the overall resistance lower than the AP state [16].

A third effect contributes to the different resistance in the P and AP state. This effect is called spin-accumulation, and is associated to the concept of spin injection and detection. This effect was already introduced by Johnson and Silsbee [19], but a more complete description was given in [16]. The origin of this effect is explained with the help of figure 1.5 for a single FM/NM metal interface. As explained in section 1, the current is spin-polarized in bulk FM metals, while it is not in bulk NM metals. When a current flows from a FM metal to a NM metal, some electrons must flip their spin to adjust the incoming and outgoing spin fluxes [16]. In figure 1.5(a), the current in the FM metal is carried mainly by spin-up electrons, a fraction of which must flip at the interface with the NM metal. Therefore, spin-up electrons “accumulate” in a region close to the interface. In this region, a splitting of the chemical potentials for the two spin channels occurs [16], giving rise to an extra potential drop, proportional to the current density. This contribution introduces an additional resistance at the interface, different from the one discussed at 2. The spin accumulation decays exponentially on each side of the interfaces, with different spin diffusion lengths  $L_F$  and  $L_N$ .

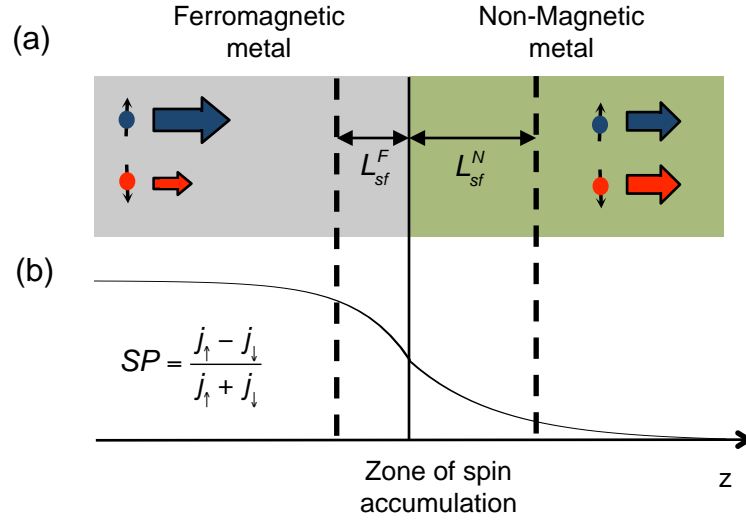


Figure 1.5. Schematics of the spin accumulation. In the FM metal the current is spin polarized, while in non-magnetic metals it is not (a). Therefore, the spin polarization of the current gradually changes from spin-polarized in the FM metal to non-spin-polarized current in the non-magnetic metal (b).

Consequently, the current spin polarization, defined as in (2), decreases while electrons flow from the bulk FM to the NM metal, with different spin diffusion lengths  $L_F$  and  $L_N$  in the two sides of the interfaces (figure 1.5(b)). The important point here is that an out-of-equilibrium spin-polarized current flows into a NM metal, for a region with a thickness in the order of  $L_N$ . Such spin polarized current is said to be “injected” by the FM metal, which therefore acts as a “spin injector”. If a second FM metal is placed at a distance  $l < L_N$  from the interface, it will sense the spin polarization of the current in the NM metal. Indeed, the spin accumulation is different in the P or AP state, and this difference is reflected in the overall SV resistance. For this reason, the second FM layer acts as a “spin detector”.

At this point, the question is for how long the current retains a spin polarization in the NM layer, or similarly, how long is  $L_N$ . It turns out that it depends on some properties of the specific metals. In particular, one of the main source of spin decoherence is the spin-orbit interaction. Since the strength of the spin-orbit interaction is proportional to the fourth power of the atomic number,  $Z^4$ , the spin diffusion length is higher in light materials. For instance, in Cu and Al [20,21],  $L_N$  approaches 1  $\mu\text{m}$ .

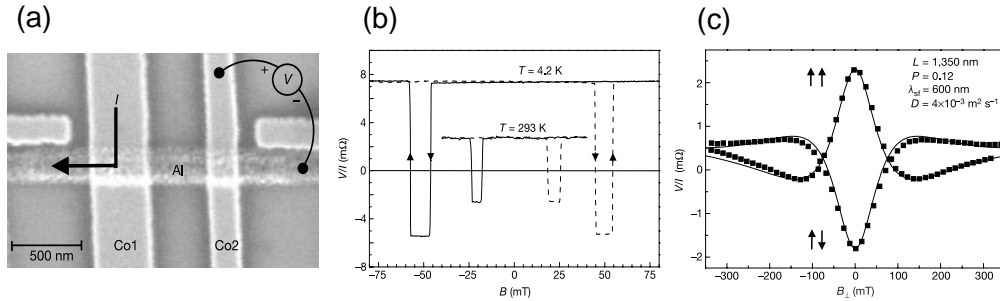


Figure 1.6. Lateral SVs from ref. [21]. (a) Electron microscopy image of the patterned SV. (b) MR of the SV. (c) Spin manipulation (see text).

With modern lithography techniques, it becomes possible to pattern lateral SVs (figure 1.6(a)), in which a NM metallic nano-sized channel connects two FM nanocontacts within a distance  $l < L_N$ . Therefore, one of the FM contacts injects a spin polarized current into the channel, and the other one detects it via a resistance change. This kind of device is also very useful because it allows the separation of electrical current path by the spin signal, as shown in figure 1.6(a). The current flows between the spin injector and the NM channel, while the detector measures a voltage difference which is only spin-related, as the electrical current is not flowing through it. A measurement with this geometry is called “non-local” measurement. The voltage drop has the typical MR shape, with different voltage measured when the FM magnetizations are switched from P to AP with an in-plane magnetic field (figure 1.6(b)). Such a voltage drop is due to the spin accumulation, and it is decoupled from the electrical current, which is not flowing through the detection contact. The possibility to decouple the electrical current and the spin-related voltage had been explored before, in different devices [22,23], but this new geometry allows to better avoid any spurious signal.

In lateral SVs, further spin manipulation has been demonstrated. An out-of-plane external magnetic field introduces a torque on the in-plane-injected spins [1], which results in a precession around the field. In this process, the direction of spins rotates, initially coherently, so that spins injected with a direction parallel to the magnetization of the injector arrive to the detector with another direction. Therefore, even if the FMs are in the P state, the voltage drop measured at the detector is not the voltage drop of the P state. The spin direction at the detector depends on the intensity of the applied field. Indeed, the voltage measured at the detector changes in a sweep of the external magnetic field, following the rotation of the spins in the NM channel, as shown in figure 1.6(c) [21]. This precession is called Hanle effect, and it can be used to extract the spin lifetime.

### 1.2.3 Semiconductors

One of the most intriguing challenges in spintronics is to make this topic compatible with semiconductors [24], that constitute the basis of most electronic devices. The proposal of a spin field-effect-transistor by Datta and Das at the beginning of the 1990s [25] attracted much interest and boost intense research in the field. A cartoon of such a transistor is shown schematically in figure 1.7(a). According to the proposal, a spin-polarized current would be injected into the semiconductor by a FM metal and detected by a second FM metal, as for the spin injection and detection in metals discussed in the previous section. Furthermore, the electrons in the semiconductor would precess around a magnetic field, as for the Hanle effect discussed in the previous section. The difference is that in this case the magnetic field would be intrinsic in the semiconductor, and not externally applied as in the previous section. A gate voltage would allow the control of the internal magnetic field, and therefore, of the spin precession in the semiconducting material. The FM detector would then detect the magnitude of the spin precession.

However, the realization of such a device proved to be extremely difficult. After 10 years of attempts, it was realized that the spin injection in semiconductors is not straightforward, because flowing a current from a FM metal to a semiconductor does not produce a spin-polarized current into the semiconductor [26]. When the resistivity of the NM material is much higher than that of the FM metal, the spin polarization decays already in the FM metal, leaving a negligible spin polarization of the current into the NM material, as shown in figure 1.7(b). This problem is known as “conductivity mismatch”, and is always present at a FM metal/semiconductor interface.

Alternative ways for the electrical injection of a spin-polarized current into a semiconductor have been proposed. Possibly, the easiest way is to insert a tunnel barrier at the FM metal/semiconductor interface [27,28]. Even in this case, the task is far from easy, because the resistance of the barrier has to be in a defined resistance range [28], which is not always achievable in devices. Electrical spin injection through a tunnel junction into semiconductors has been demonstrated only 15 years after the Datta Das proposal [29,30]. Also, a spin transistor very similar to the original proposal was demonstrated in reference [31], although the topic remains controversial.

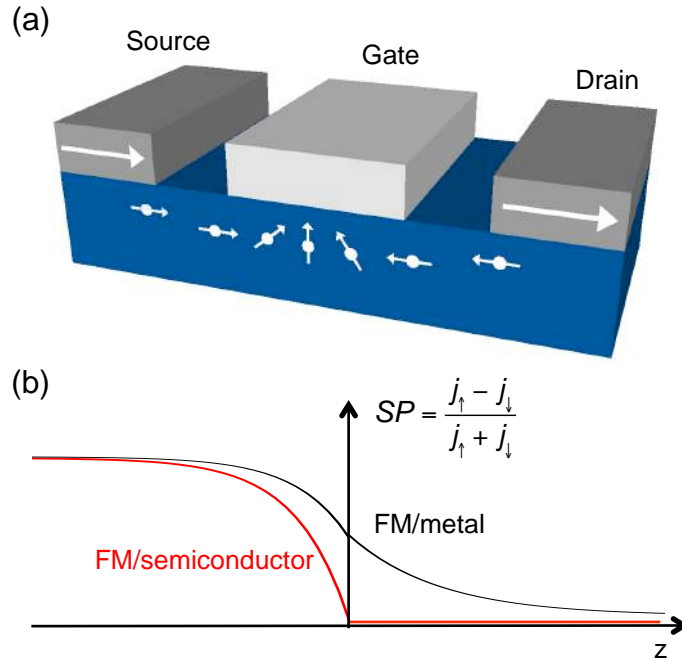


Figure 1.7. (a) Scheme of the Datta Das spin transistor. Adapted from [25]. (b) Spin polarization at a FM/metal and FM/semiconductor interface. The current injected into the semiconductor is not spin polarized.

Other methods for injecting spin-polarized current into semiconductors have been proposed. A particularly successful one involves the electrical injection of spin filtered hot electrons into semiconductors [32,33]. Based on this spin filtering effect, a device called spin-valve transistor was demonstrated, representing one of the most successful realization of a hybrid FM metal/semiconductor device [34,35]. SV transistors are 3-terminal devices with the same scheme of metal base transistor, in which a hot-electron current is injected into the device by an emitter, and a base modulates the amount of current reaching the semiconducting collector. Such a modulation is driven by an external magnetic field, which switches the SV base from a P to an AP alignment, and produces an extremely high variation of the current entering the collector. In the case of SV transistors, the spin manipulation does not take place in the semiconductor, but in the metallic base; the semiconductor is only used to provide an energy barrier for the energy filtering. This device will be described in more detail in chapter 5, while in chapter 6 I will focus on the injection of spin polarized hot electrons into semiconductors.

## 1.3 Carbon-based materials

Carbon is emerging as a promising material for novel spintronics applications. As explained in the previous sections, a long spin lifetime is a fundamental requirement for advanced spin manipulation, such as the Hanle precession, and it is at the basis of the spin transistors. As mentioned in section 1.2.2, one of the main sources of spin scattering is the spin-orbit interaction, which is stronger in heavy materials – being roughly proportional to the fourth power of the atomic number  $Z^4$ . Carbon based materials are composed by extremely light materials, so the spin lifetime is expected to be longer than in materials commonly used in spintronics.

Based on the different transport characteristics, one can identify two main classes of carbon-based materials: on one hand, carbon nanotubes and graphene; on the other hand, organic semiconductors. In this section, I will show the results of recent experiments indicating that spintronics can take profit from both categories.

### 1.3.1 Carbon nanotubes and Graphene

Unlike other carbon-based materials, carbon nanotubes (CNT) and graphene are characterized by extremely high mobility and Fermi velocity. A Fermi velocity  $v_F = 10^6 \text{m/s}$  has been reported in CNT [36] and graphene [37]; with corresponding mobility  $\mu > 10^5 \text{cm}^2/\text{Vs}$  [38,39], and up to  $\mu = 2 \times 10^6 \text{cm}^2/\text{Vs}$  for suspended graphene [40]. Another common characteristic is that CNT and graphene are only composed by carbon. For these materials, spin scattering mechanisms are extremely weak. Not only the spin-orbit interaction in carbon is extremely low [41], but also the hyperfine interaction produced by the nuclei, which is another source of spin scattering, is extremely low too. Indeed, the carbon nucleus  $^{12}\text{C}$  isotope has a spin singlet, and thus does not count for the hyperfine interaction, while the  $^{13}\text{C}$  isotope nucleus is rare (natural abundance  $< 2\%$ ). The expected spin lifetime in these materials is therefore extremely high, in the  $\mu\text{s}$  range [41,42]. This expected long spin lifetime, together with the ultrahigh mobility, suggests that in CNT and graphene the spin information could travel over extremely long distances, in the  $\mu\text{m}$  range.

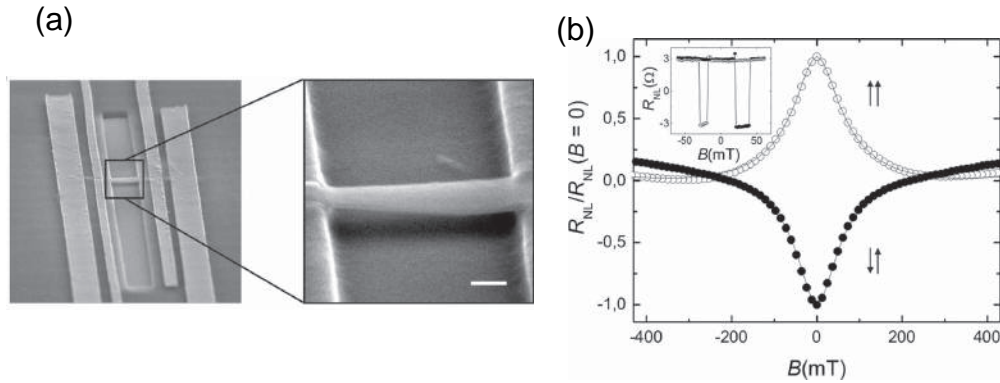


Figure 1.8. Four terminal lateral SV with a suspended graphene channel. (a) scanning electron microscope image of the device, with a zoom of the free standing graphene suspended between two FM electrodes. (b) shows the measurement of the Hanle effect in the device in (a). In the inset, the classical SV MR is recognizable.

CNTs and graphene spintronics has been subject of intense research in the last few years. Initially, it was shown that extremely high MR (60%) could be obtained in lateral SVs with a CNT interlayer as long as  $2 \mu\text{m}$  [43]. Afterwards, most of the effort was focused on graphene, because of the relatively easy fabrication of high quality flakes. All the techniques previously applied to the study of metals have been applied also to graphene. Lateral SVs with graphene interlayers were produced employing the non-local geometry described in section 1.2.2 [44,45] or the simpler 2 terminal geometry [46]. As an example, figure 1.8 shows a recent result of a 4 terminal SV with a channel of suspended graphene, from reference [47]; (a) shows the high quality of the device; (b) the electrical measurements, that is very similar to that of figure 1.6(c). Graphene-based spintronic devices have been demonstrated on different substrates (for instance,  $\text{SiO}_2$  [44], free standing [47,48],  $\text{SiC}$  [49]), with different interfaces to the FM electrodes [50,51], making graphene one of the most studied materials (also) for spintronics. So far, the spin lifetime measured through the Hanle effect (maximum 2.3 ns in epitaxial graphene [49]) is several orders of magnitude below the expected one. Despite this discrepancy, the demonstrated spin diffusion length is well above  $1 \mu\text{m}$ , thanks to the extremely high mobility. In [46], a spin diffusion length of  $100 \mu\text{m}$  is claimed, though not directly measured via the Hanle effect.

In conclusion, CNTs and graphene are ideal materials for those applications in which the spin information has to travel laterally over long distances. In this sense, they are comparable to light metals, but better in terms of spin transport properties.

### 1.3.2 Organic semiconductors

There are several reasons why organic semiconductors (OS) are attractive for spintronics. First, the spin scattering mechanisms are weak, as already discussed for CNTs and graphene. In the case of OS, spin lifetimes close to 1  $\mu$ s have been measured with electron paramagnetic resonance [52–54]. However, a priori, such long spin lifetime does not translate into long spin diffusion lengths, because most OS are characterized by low mobility (typically below  $\mu = 1 \text{ cm}^2/\text{Vs}$  [55]). Moreover, the resistance of OS is much higher than the resistance of FM metals, as for the case of inorganic semiconductors. Therefore, the problem of conductivity mismatch and the difficulties of injecting spin-polarized current should also apply to OS. The first demonstration of MR in lateral SVs with a long polymeric interlayer (sexithienyl, T6,  $\text{C}_{24}\text{H}_{14}\text{S}_6$  [56]) came as a great surprise. The result was followed by the measurement of MR in nanosized vertical tunnel junctions based on an octanethiol self-assembled monolayer sandwiched between two Nickel electrodes [57]. However, the reproducibility of this result was limited by the complicated fabrication technique employed for patterning the junctions.

An important step towards more controllable organic-based spintronics was the fabrication of vertical SVs with big junction area (from hundreds of square microns to square millimeters), obtained by deposition in vacuum through shadow masks. Initially, MR was measured in SVs with a thick (>100 nm) interlayer of 8-hydroxy-quinoline aluminium ( $\text{Alq}_3$ ) inserted between a manganite (LSMO) and a Co electrode (see figure 1.9(a)). High *negative* MR (>40%) was measured in these SVs (see figure 1.9(b)) [58]. This effect was confirmed in analogous devices by other groups [59,60]. Furthermore, similar results were demonstrated in devices with analogous electrodes separated by thick layers of other small molecules,  $\alpha$ -NPD and CVB [59]. Small molecules are particularly attractive as SV interlayers, because they can be sublimed in ultra-high vacuum environments to form clean interfaces with FM electrodes. However, SVs with spin-coated polymer interlayers have also been reported [61,62]. In all these cases, thick organic films were employed as SV interlayers, so that the measurement of MR was taken as the demonstration of the conservation of the spin coherence across the organic layer. SVs were used to estimate spin diffusion lengths in the organic spacer, following the spin injection-transport-detection framework described in the previous sections. In some cases, spin diffusion lengths above 100 nm were reported [63].

In parallel, organic SVs were also produced with an ultra-thin organic interlayer acting as a tunneling barrier. These devices, fabricated in ultra high-vacuum and patterned by

### 1.3 Carbon-based materials

evaporation through shadow masks, employed 3d FM electrodes and hybrid barriers composed by an inorganic seed layer ( $\text{AlO}_x$  or  $\text{MgO}$ ) and a molecular layer ( $\text{Alq}_3$  [64–66] or rubrene [67]). Positive MR was measured in these devices.

Also, organic magnetic tunnel junctions with nanosized junction areas have been reported, based on  $\text{Alq}_3$  [68] and on the self assembly of dodecyl (C12P) and octadecyl (C18P) phosphonic acids [69]. Ultra-high positive high MR ( $> 300\%$ ) has been measured at 2K in an  $\text{Alq}_3$  device. Recently, a SV has been reported in which a reaction at the interface between Co and a radical species with unpaired spin (phenalenyl) give rise to an organometallic interfacial state that behaves as a spin filter [70].

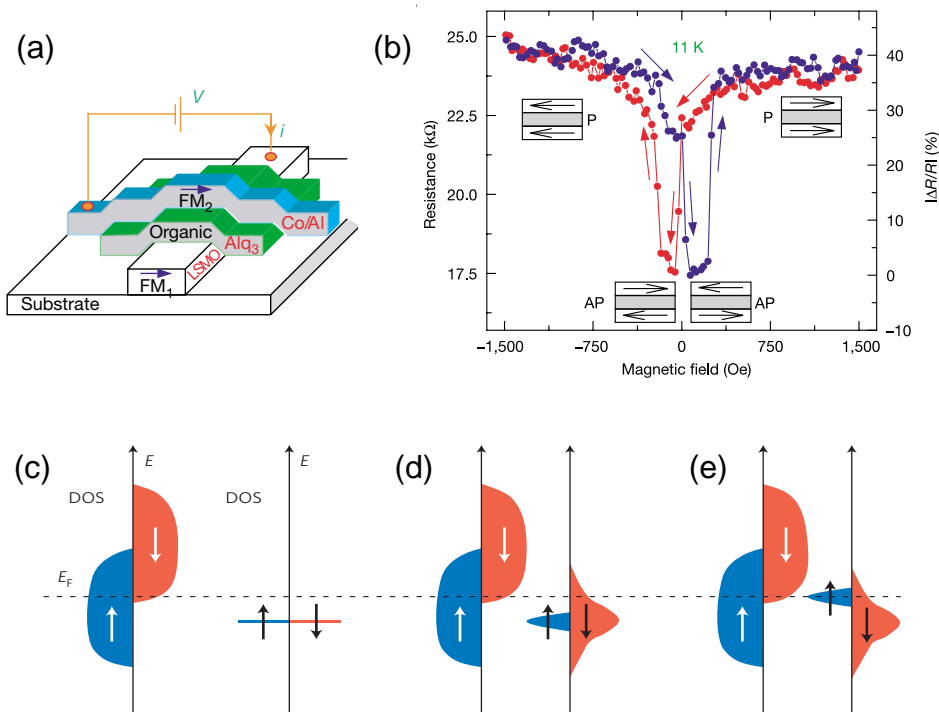


Figure 1.9. (a) Scheme of a SV based on a thick  $\text{Alq}_3$  layer. (b) MR measured in the device in (a) [58]. (c), (d), (e) Schematics of the density of states at a molecule/FM metal interface taken from [71]. (c) The molecule and the metal surface are separated (not interacting), (d) and (e) show that when the molecules interacts with the interface their energy level broaden and shift.

Given the variety of the results described above, it was soon realized that the sign and the magnitude of MR depend on the details of the molecule/FM metal interface. It was proposed that the interaction between the molecules and a FM surface might change the interfacial spin-polarization, enhancing or inverting it depending on the

surface/molecule system [68]. This is schematically shown in figure 1.10 (c)-(e). Figure 1.10 (c) shows the density of states of a FM metal and a molecule when they are well separated, not interacting with each other. The FM metals possess the usual DOS (figure 1.1(a)), and the molecule, a series of discrete energy levels. When the molecule is brought into contact with the metal, reactions take place between the molecules and the metal surface and the DOS gets modified in two ways: the energy levels broaden (b) and their position shifts in energy (c). Therefore the spin polarization of the hybridized surface/molecule system might be different from the original FM metal alone, causing a MR enhancement (b) or reversal (c) [68]. The fact that an inversion of the interfacial density of states could cause negative MR had been demonstrated previously [72]. This effect points out another reason for which OSs are attractive for spintronics: molecules can be used to modify a FM surface and tailor its spin polarization, by either enhancing or reversing it. This effect can hardly be achieved with other materials – possibly only with epitaxial interfaces of ultra-high quality.

In order to gain more insight on the topic, several works have focused on molecules/FM metal interfaces rather than on the fabrication of devices. The fact that reactions between metals and molecules can change drastically the energetics of the surface is well established (ref. [73] and references therein). The novel ingredient is the modification of the spin polarization. It has been shown that strong electrical dipoles are present at the interfaces of LSMO/Alq<sub>3</sub>, Co/Alq<sub>3</sub>, Co/CuPc and Fe/C<sub>60</sub> by means of photoemission spectroscopy [74–79]. These interfacial dipoles can alter the equilibrium energy levels by more than 1 eV, indicating the presence of strong interfacial reactions. Also, the magnetic properties of the reacted interfaces have been studied with X-Ray Magnetic Circular Dichroism (XMCD). It was found that the presence of the FM metal induces a spin polarization in the first molecular layer [78,80], supporting the model described in figure 1.9 (c).

More advanced techniques have been exploited to directly reveal the profile distribution of the spin polarization inside OS, two-photon photoemission spectroscopy and muon spin-rotation. The former has been applied to measure that the spin injection from Co into thin layers of CuPc with different thicknesses is very efficient (approaching 100% in the first monolayer, and then weakly decaying [81]). Furthermore, with the same technique it has been found that electrons are trapped in hybrid interface states for a time lapse that is spin dependent [82]. A muon spin rotation technique has been used to measure the depth-resolved spin polarization in Alq<sub>3</sub> SVs, based on which a spin diffusion length of 35 nm has been extracted [83]. Moreover, the effect of an interface modification has been studied, leading to the conclusion that the presence of a polar layer at the interface between the FM electrode and the organic semiconductor can invert the sign of the spin polarization [84].

Other possible developments of OS spintronics involve the addition of the spin degree of freedom into organic-based electronic devices, in particular in organic light emitting diodes (OLED) and in organic field effect transistors (OFET). As for OLEDs, it was thought that the injection of spin-polarized current into OS could improve the light emission efficiency [85]. Recently, a light-emitting organic SV was reported in which the luminescence depended on the relative orientation of the FM electrodes [86]. As for OFETs, organic spin-FETs can be envisaged, similarly to the inorganic FET in figure 1.7(a), that take advantage from the longer spin-lifetime. So far, no spin-OFETs have been demonstrated, although some attempts have been done in this direction [87]. Possibly, the problems related to the spin injection in inorganic semiconductors also apply to OS.

Molecules with magnetic properties can be exploited in spintronics. For instance, molecular compounds with a high spin ground state can be synthesized [88,89]. These compounds, called "single molecule magnets", behave in some extent as ferromagnetic materials at low temperatures, and might form part of future all-molecular spintronic devices [90]. With this purpose, the coupling of a FM metal surface with paramagnetic molecules [91] and single molecule magnets [92] has been investigated. Recently, devices have been produced employing single molecule magnets deposited onto graphene and CNTs. In these devices, the different alignment of molecular momenta induces a spin-valve-like variation in the resistance of the graphene/CNT channel [93,94]. Also, it has been shown that the nuclear spin state of a single molecule magnet can be read out electrically by contacting one single molecule between two gold electrodes [95].

In summary, spintronics is only beginning to take full advantage of the almost unlimited variety of molecules, that can be synthesized "on demand" with any desired property.

## 1.4 Our approach to carbon spintronics

In this thesis, we focused on the production of spintronic devices based on thin films of fullerene  $C_{60}$ . Discovered in 1985,  $C_{60}$  is the well-known molecule shown in figure 1.10 (a).  $C_{60}$  is particularly suitable for spintronic devices because it can be sublimed in an ultra-high vacuum environment, in situ with FM materials. It is a robust molecule, and minor damage is expected upon the evaporation of the top metal contact. Furthermore,  $C_{60}$  has been widely studied and used also in standard organic electronics, especially as n-type semiconductor in FETs [96] and as electron acceptor in polymer/ $C_{60}$  blends for

solar cells [97,98]. For these reasons, its electron transport properties are well established:  $C_{60}$  is a n-type semiconductor with high mobility ( $\mu > 1 \text{ cm}^2/\text{Vs}$ , measured in OFET structures [96]).

In some senses, the molecular species  $C_{60}$  is in between the two categories of carbon based materials described in the previous section. It is a molecule, and its current transport properties are similar to those of organic semiconductors. However, it is only composed by carbon, so that it is not “organic”. Especially for the spin transport properties, this feature marks an important difference: the main spin scattering mechanism in organics is thought to be the hyperfine interaction with protons in the nuclei, and in particular with the hydrogen nuclei [99], that are not present in  $C_{60}$ . Other sources of spin scattering should then be taken into account for  $C_{60}$ . In particular, it has been shown that the spin-orbit interaction in *curved* carbon surfaces can be significant. While for flat graphene spin-orbit effects are expected at energy scales of  $\Delta_{SO} \approx 1 \text{ } \mu\text{eV}$ , they become more pronounced when carbon does not lie flat, but has some curvature [41], as for carbon nanotubes and fullerenes. In fact, a spin-orbit splitting above  $\Delta_{SO} > 100 \text{ } \mu\text{eV}$  has been measured in carbon nanotubes [100–102], indicating that a similar effect might be present in  $C_{60}$ . However, this effect is weak compared with other semiconductors (for Si, the spin-orbit splitting of the valence band is  $\Delta_{SO} \approx 44 \text{ meV}$ ; for Ge and GaAs,  $\Delta_{SO} \approx 300 \text{ meV}$ ). Indeed, a spin diffusion length above 400 nm has been predicted for  $C_{60}$  layers in a recent work [103].

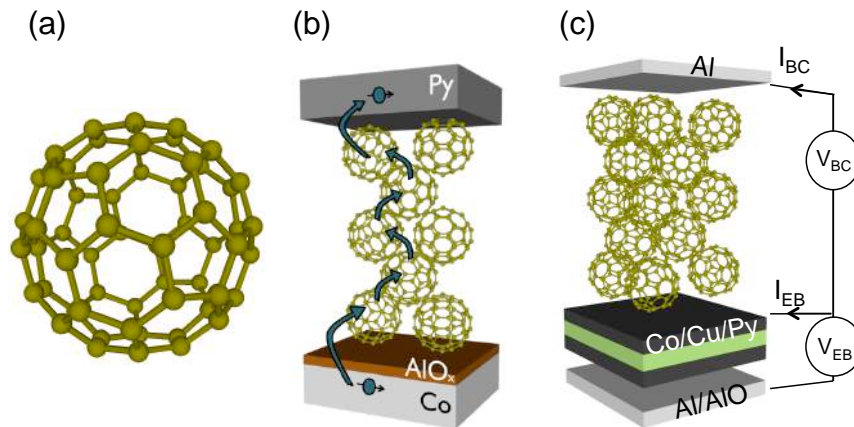


Figure 1.10 (a) The molecule of  $C_{60}$  fullerene. (b) and (c) our spintronic devices based on  $C_{60}$ : the SV (b) and the magnetic tunnel transistor (c). Note that the layer thicknesses are not in scale: in (c) the  $C_{60}$  thickness should be much thicker.

Our  $C_{60}$  based spintronic devices are shown in figure 1.10(b) and (c). We produced SVs and magnetic tunnel transistors. In SVs, a thin (thickness  $< 30$  nm)  $C_{60}$  layer is used as spin transport layer between two FM layers, one for the spin injection and the other one for the detection. As explained in the previous sections, the measurement of MR is taken as the demonstration of spin transport. I show that in SVs the  $C_{60}$  layers acts as an insulating barrier, and our results can be interpreted in terms of a multistep tunneling between  $C_{60}$  molecules. In magnetic tunnel transistors, a  $C_{60}$  thick layer (thickness  $> 130$  nm) act as the semiconductor collector in a metal-base-transistor geometry. In this thesis, chapter 4 and 5 are dedicated to the description of the  $C_{60}$  spin valves and magnetic tunnel transistors respectively. Prior to that, chapter 2 is dedicated to the description of the experimental setup with which the devices have been produced and characterized, and chapter 3 focuses on the characterization of the single films that compose the various devices.

Finally, I would like to point out that the interest for  $C_{60}$  in spintronics is shared with other groups over the world. Several results appeared in parallel with this thesis [79,80,104–109]. Also, SV devices very similar to ours have been reported [106] after the work extracted from this thesis.

## 1.5 References

- [1] I. Zutic, J. Fabian, and S. D. Sarma, *Reviews of Modern Physics* **76**, (2004).
- [2] H. Ibach and H. Lüth, *Solid-State Physics: An Introduction to Principles of Materials Science* (2003).
- [3] I. I. Mazin, *Physical Review Letters* **83**, 1427 (1999).
- [4] M. N. Baibich, J. M. Broto, A. Fert, F. Nguyen VanDau, F. Petroff, P. Eitenne, G. Creuzet, A. Friederich, and J. Chazelas, *Physical Review Letters* **61**, 2472 (1988).
- [5] G. Binasch, P. Grünberg, F. Saurenbach, and W. Zinn, *Physical Review B* **39**, 4828 (1989).
- [6] C. Chappert, A. Fert, and F. N. Van Dau, *Nature Materials* **6**, (2007).
- [7] J. S. Moodera, L. R. Kinder, T. M. Wong, and R. Meservey, *Physical Review Letters* **74**, 3273 (1995).
- [8] T. Miyazaki and N. Tezuka, *Journal of Magnetism and Magnetic Materials* **139**, 94 (1995).
- [9] P. Leclair, *Fundamental Aspects of Spin Polarized Tunneling*, PhD Thesis, Technische Universiteit Eindhoven, 2002.

- [10] D. Wang, C. Nordman, J. M. Daughton, Z. Qian, and J. Fink, IEEE Transactions on Magnetics **40**, 2269 (2004).
- [11] S. Yuasa and D. D. Djayaprawira, Journal of Physics D: Applied Physics **40**, R337 (2007).
- [12] S. S. P. Parkin, C. Kaiser, A. Panchula, P. M. Rice, B. Hughes, M. Samant, and S.-H. Yang, Nature Materials **3**, 862 (2004).
- [13] W. Butler, X.-G. Zhang, T. Schulthess, and J. MacLaren, Physical Review B **63**, 054416 (2001).
- [14] S. S. P. Parkin, N. More, and K. P. Roche, Physical Review Letters **64**, 2304 (1990).
- [15] B. Dieny, V. S. Speriosu, S. S. P. Parkin, B. A. Gurney, D. R. Wilhoit, and D. Mauri, Physical Review B **43**, 1297 (1991).
- [16] T. Valet and A. Fert, Physical Review B **48**, 7099 (1993).
- [17] N. F. Mott, Proc. Roy. Soc. A **153**, 699 (1936).
- [18] A. Fert and I. A. Campbell, Physical Review Letters **21**, 1190 (1968).
- [19] M. Johnson and R. H. Silsbee, Physical Review Letters **60**, 377 (1988).
- [20] F. J. Jedema, a T. Filip, and B. J. van Wees, Nature **410**, 345 (2001).
- [21] F. J. Jedema, H. B. Heersche, a T. Filip, J. J. a Baselmans, and B. J. van Wees, Nature **416**, 713 (2002).
- [22] M. Johnson, Science **260**, 320 (1993).
- [23] M. Johnson, Physical Review Letters **70**, 2142 (1993).
- [24] D. D. Awschalom and M. E. Flatte, Nature Physics **3**, 153 (2007).
- [25] S. Datta and B. Das, Applied Physics Letters **56**, 665 (1990).
- [26] G. Schmidt, D. Ferrand, L. Molenkamp, a Filip, and B. van Wees, Physical Review B **62**, R4790 (2000).
- [27] E. Rashba, Physical Review B **62**, R16267 (2000).
- [28] A. Fert and H. Jaffrès, Physical Review B **64**, 184420 (2001).
- [29] X. Lou, C. Adelman, S. a. Crooker, E. S. Garlid, J. Zhang, K. S. M. Reddy, S. D. Flexner, C. J. Palmstrøm, and P. a. Crowell, Nature Physics **3**, 197 (2007).
- [30] B. T. Jonker, G. Kioseoglou, A. T. Hanbicki, C. H. Li, and P. E. Thompson, Nature Physics **3**, 542 (2007).
- [31] H. C. Koo, J. H. Kwon, J. Eom, J. Chang, S. H. Han, and M. Johnson, Science (New York, N.Y.) **325**, 1515 (2009).
- [32] X. Jiang, R. Wang, S. van Dijken, R. Shelby, R. Macfarlane, G. Solomon, J. Harris, and S. Parkin, Physical Review Letters **90**, 25 (2003).
- [33] I. Appelbaum, B. Huang, and D. J. Monsma, Nature **447**, 295 (2007).
- [34] D. J. Monsma, J. C. Lodder, T. J. A. Popma, and B. Dieny, Physical Review Letters **74**, 5260 (1995).

## 1.5 References

---

- [35] R. Jansen, *Journal of Physics D: Applied Physics* **36**, R289 (2003).
- [36] M. Buitelaar, a. Bachtold, T. Nussbaumer, M. Iqbal, and C. Schönenberger, *Physical Review Letters* **88**, 156801 (2002).
- [37] K. S. Novoselov, a K. Geim, S. V. Morozov, D. Jiang, M. I. Katsnelson, I. V. Grigorieva, S. V. Dubonos, and a a Firsov, *Nature* **438**, 197 (2005).
- [38] T. Dürkop, S. a. Getty, E. Cobas, and M. S. Fuhrer, *Nano Letters* **4**, 35 (2004).
- [39] J. Chen, C. Jang, S. Xiao, M. Ishigami, and M. S. Fuhrer, *Nature Nanotechnology* **3**, 206 (2008).
- [40] K. I. Bolotin, K. J. Sikes, Z. Jiang, M. Klima, G. Fudenberg, J. Hone, P. Kim, and H. L. Stormer, *Science* **318**, 850 (2007).
- [41] D. Huertas-Hernando, F. Guinea, and A. Brataas, *Physical Review B* **74**, 155426 (2006).
- [42] B. Trauzettel, D. V. Bulaev, D. Loss, and G. Burkard, *Nature Physics* **3**, 192 (2007).
- [43] L. E. Hueso, J. M. Pruneda, V. Ferrari, G. Burnell, J. P. Valdés-Herrera, B. D. Simons, P. B. Littlewood, E. Artacho, A. Fert, and N. D. Mathur, *Nature* **445**, 410 (2007).
- [44] N. Tombros, C. Jozsa, M. Popinciuc, H. T. Jonkman, and B. J. van Wees, *Nature* **448**, 571 (2007).
- [45] W. Han, K. M. McCreary, K. Pi, W. H. Wang, Y. Li, H. Wen, J. R. Chen, and R. K. Kawakami, *Journal of Magnetism and Magnetic Materials* **324**, 369 (2012).
- [46] B. Dlubak, M. Martin, C. Deranlot, B. Servet, S. Xavier, R. Mattana, M. Sprinkle, C. Berger, W. A. D. Heer, F. Petroff, A. Anane, P. Seneor, and A. Fert, *Nature Physics* **8**, 557 (2012).
- [47] I. Neumann, J. Van de Vondel, G. Bridoux, M. V. Costache, F. Alzina, C. M. S. Torres, and S. O. Valenzuela, *Small* **9**, 156 (2012).
- [48] M. H. D. Guimarães, a Veligura, P. J. Zomer, T. Maassen, I. J. Vera-Marun, N. Tombros, and B. J. van Wees, *Nano Letters* **12**, 3512 (2012).
- [49] T. Maassen, J. J. van den Berg, N. Ijbema, F. Fromm, T. Seyller, R. Yakimova, and B. J. van Wees, *Nano Letters* **12**, 1498 (2012).
- [50] W. Han, K. Pi, K. McCreary, Y. Li, J. Wong, a. Swartz, and R. Kawakami, *Physical Review Letters* **105**, 167202 (2010).
- [51] J. Maassen, W. Ji, and H. Guo, *Nano Letters* **11**, 151 (2011).
- [52] V. I. Krinichnyi, S. D. Chemerisov, and Y. S. Lebedev, *Physical Review B* **55**, 16233 (1997).
- [53] V. I. Krinichnyi, *Synthetic Metals* **108**, 173 (2000).
- [54] D. R. McCamey, H. a Seipel, S.-Y. Paik, M. J. Walter, N. J. Borys, J. M. Lupton, and C. Boehme, *Nature Materials* **7**, 723 (2008).

- [55] Y. Yamashita, *Science and Technology of Advanced Materials* **10**, 024313 (2009).
- [56] V. Dediu, M. Murgia, F. C. Maticotta, C. Taliani, and S. Barbanera, *Solid State Communications* **122**, 181 (2002).
- [57] J. Petta, S. Slater, and D. Ralph, *Physical Review Letters* **93**, 136601 (2004).
- [58] Z. H. Xiong, D. Wu, Z. V. Vardeny, and J. Shi, *Nature* **427**, 821 (2004).
- [59] F. Wang, C. Yang, Z. Vardeny, and X. Li, *Physical Review B* **75**, 245324 (2007).
- [60] V. Dediu, L. Hueso, I. Bergenti, a. Riminucci, F. Borgatti, P. Graziosi, C. Newby, F. Casoli, M. De Jong, C. Taliani, and Y. Zhan, *Physical Review B* **78**, 115203 (2008).
- [61] N. a. Morley, a. Rao, D. Dhandapani, M. R. J. Gibbs, M. Grell, and T. Richardson, *Journal of Applied Physics* **103**, 07F306 (2008).
- [62] T. D. Nguyen, G. Hukic-Markosian, F. Wan, L. Wojcik, X.-G. Li, E. Ehrenfreund, and Z. V. Vardeny, *Nature Materials* **9**, 345 (2010).
- [63] V. A. Dediu, L. E. Hueso, I. Bergenti, and C. Taliani, *Nature Materials* **8**, 707 (2009).
- [64] T. Santos, J. Lee, P. Migdal, I. Lekshmi, B. Satpati, and J. Moodera, *Physical Review Letters* **98**, 016601 (2007).
- [65] J. Schoonus, P. Lumens, W. Wagemans, J. Kohlhepp, P. Bobbert, H. Swagten, and B. Koopmans, *Physical Review Letters* **103**, 146601 (2009).
- [66] G. Szulczewski, H. Tokuc, K. Oguz, and J. M. D. Coey, *Applied Physics Letters* **95**, 202506 (2009).
- [67] J. Shim, K. Raman, Y. Park, T. Santos, G. Miao, B. Satpati, and J. Moodera, *Physical Review Letters* **100**, 226603 (2008).
- [68] C. Barraud, P. Seneor, R. Mattana, S. Fusil, K. Bouzehouane, C. Deranlot, P. Graziosi, L. Hueso, I. Bergenti, V. Dediu, F. Petroff, and A. Fert, *Nature Physics* **6**, 615 (2010).
- [69] M. Galbiati, C. Barraud, S. Tatay, K. Bouzehouane, C. Deranlot, E. Jacquet, A. Fert, P. Seneor, R. Mattana, and F. Petroff, *Advanced Materials* **24**, 6429 (2012).
- [70] K. V. Raman, A. M. Kamerbeek, A. Mukherjee, N. Atodiresei, T. K. Sen, P. Lazić, V. Caciuc, R. Michel, D. Stalke, S. K. Mandal, S. Blügel, M. Münzenberg, and J. S. Moodera, *Nature* **493**, 509 (2013).
- [71] S. Sanvito, *Nature Physics* **6**, 562 (2010).
- [72] J. M. De Teresa, A. Barthelemy, A. Fert, J. P. Contour, F. Montaigne, P. Seneor, *Science* **286**, 507 (1999).
- [73] J. Hwang, A. Wan, and A. Kahn, *Materials Science and Engineering: R: Reports* **64**, 1 (2009).
- [74] Y. Zhan, I. Bergenti, L. Hueso, V. Dediu, M. de Jong, and Z. Li, *Physical Review B* **76**, 045406 (2007).

- [75] Y. Zhan, M. de Jong, F. Li, V. Dediu, M. Fahlman, and W. Salaneck, *Physical Review B* **78**, 045208 (2008).
- [76] M. Grobosch, K. Dorr, R. B. Gangineni, and M. Knupfer, *Applied Physics Letters* **92**, 023302 (2008).
- [77] Y. Q. Zhan, X. J. Liu, E. Carlegrim, F. H. Li, I. Bergenti, P. Graziosi, V. Dediu, and M. Fahlman, *Applied Physics Letters* **94**, 053301 (2009).
- [78] Y. Zhan, E. Holmström, R. Lizárraga, O. Eriksson, X. Liu, F. Li, E. Carlegrim, S. Stafström, and M. Fahlman, *Advanced Materials* **22**, 1626 (2010).
- [79] T. L. A. Tran, D. Cakır, P. K. J. Wong, A. B. Preobrajenski, G. Brocks, W. G. van der Wiel, and M. P. de Jong, *ACS Applied Materials & Interfaces* **5**, 837 (2013).
- [80] T. L. a. Tran, P. K. J. Wong, M. P. de Jong, W. G. van der Wiel, Y. Q. Zhan, and M. Fahlman, *Applied Physics Letters* **98**, 222505 (2011).
- [81] M. Cinchetti, K. Heimer, J.-P. Wüstenberg, O. Andreyev, M. Bauer, S. Lach, C. Ziegler, Y. Gao, and M. Aeschlimann, *Nature Materials* **8**, 115 (2009).
- [82] S. Steil, N. Großmann, M. Laux, A. Ruffing, D. Steil, M. Wiesenmayer, S. Mathias, O. L. A. Monti, M. Cinchetti, and M. Aeschlimann, *Nature Physics* (2013).
- [83] A. J. Drew, J. Hoppler, L. Schulz, F. L. Pratt, P. Desai, P. Shakya, T. Kreouzis, W. P. Gillin, A. Suter, N. A. Morley, V. K. Malik, A. Dubroka, K. W. Kim, H. Bouyanfif, F. Bourqui, C. Bernhard, R. Scheuermann, G. J. Nieuwenhuys, T. Prokscha, and E. Morenzoni, *Nature Materials* **8**, 109 (2009).
- [84] L. Schulz, L. Nuccio, M. Willis, P. Desai, P. Shakya, T. Kreouzis, V. K. Malik, C. Bernhard, and A. J. Drew, *Nature Materials* **10**, 39 (2011).
- [85] I. Bergenti, V. Dediu, E. Arisi, T. Mertelj, M. Murgia, a. Riminucci, G. Ruani, M. Solzi, and C. Taliani, *Organic Electronics* **5**, 309 (2004).
- [86] T. D. Nguyen, E. Ehrenfreund, and Z. V. Vardeny, *Science* **337**, 204 (2012).
- [87] W. J. M. Naber, M. F. Craciun, J. H. J. Lemmens, a. H. Arkenbout, T. T. M. Palstra, a. F. Morpurgo, and W. G. van der Wiel, *Organic Electronics* **11**, 743 (2010).
- [88] N. Ishikawa, *Polyhedron* **26**, 2147 (2007).
- [89] R. Sessoli and A. K. Powell, *Coordination Chemistry Reviews* **253**, 2328 (2009).
- [90] L. Bogani and W. Wernsdorfer, *Nature Materials* **7**, 179 (2008).
- [91] H. Wende, M. Bemien, J. Luo, C. Sorg, N. Ponpandian, J. Kurde, J. Miguel, M. Piantek, X. Xu, P. Eckhold, W. Kuch, K. Baberschke, P. M. Panchmatia, B. Sanyal, P. M. Oppeneer, and O. Eriksson, *Nature Materials* **6**, 516 (2007).
- [92] a. Lodi Rizzini, C. Krull, T. Balashov, J. Kavich, a. Mugarza, P. Miedema, P. Thakur, V. Sessi, S. Klyatskaya, M. Ruben, S. Stepanow, and P. Gambardella, *Physical Review Letters* **107**, 177205 (2011).
- [93] M. Urdampilleta, S. Klyatskaya, J. Cleuziou, M. Ruben, and W. Wernsdorfer, *Nature Materials* **10**, 502 (2011).

- [94] A. Candini, S. Klyatskaya, M. Ruben, W. Wernsdorfer, and M. Affronte, *Nano Letters* **11**, 2634 (2011).
- [95] R. Vincent, S. Klyatskaya, M. Ruben, W. Wernsdorfer, and F. Balestro, *Nature* **488**, 357 (2012).
- [96] Y. Wen and Y. Liu, *Advanced Materials* **22**, 1331 (2010).
- [97] G. Yu, J. Gao, J. C. Hummelen, F. Wudi, and A. J. Heeger, *Science* **270**, 1789 (1995).
- [98] S. Günes, H. Neugebauer, and N. S. Sariciftci, *Chemical Reviews* **107**, 1324 (2007).
- [99] P. Bobbert, W. Wagemans, F. van Oost, B. Koopmans, and M. Wohlgenannt, *Physical Review Letters* **102**, 156604 (2009).
- [100] F. Kuemmeth, S. Ilani, D. C. Ralph, and P. L. McEuen, *Nature* **452**, 448 (2008).
- [101] G. a. Steele, F. Pei, E. a. Laird, J. M. Jol, H. B. Meerwaldt, and L. P. Kouwenhoven, *Nature Communications* **4**, 1573 (2013).
- [102] T. S. Jespersen, J. Paaske, K. Muraki, T. Fujisawa, and K. Flensberg, *Nature Physics* **7**, 348 (2011).
- [103] Z. Yu, *Physical Review B* **85**, 115201 (2012).
- [104] F. Wang and Z. V. Vardeny, *Synthetic Metals* **160**, 210 (2010).
- [105] R. Lin, F. Wang, M. Wohlgenannt, C. He, X. Zhai, and Y. Suzuki, *Synthetic Metals* **161**, 553 (2011).
- [106] T. L. A. Tran, T. Q. Le, J. G. M. Sanderink, W. G. van der Wiel, and M. P. de Jong, *Advanced Functional Materials* **22**, 1180 (2012).
- [107] S. L. Kawahara, J. Lagoute, V. Repain, C. Chacon, Y. Girard, S. Rousset, a Smogunov, and C. Barreteau, *Nano Letters* **12**, 4558 (2012).
- [108] X. Zhang, S. Mizukami, T. Kubota, Q. Ma, M. Oogane, H. Naganuma, Y. Ando, and T. Miyazaki, *Nature Communications* **4**, 1392 (2013).
- [109] T. D. Nguyen, F. Wang, X.-G. Li, E. Ehrenfreund, and Z. V. Vardeny, *Physical Review B* **87**, 075205 (2013).

---

## Chapter 2

# Experimental Methods

*In this chapter I describe the equipment used to fabricate and characterize the devices under study in this thesis. Most of the equipment was newly acquired at the beginning of my PhD project, so an important part of my PhD was its starting up and optimization. I describe in detail the dual chamber evaporator and the Lakeshore probe station, for which I have been the main user and trainer. In particular, the optimization of the evaporator required in-house hardware modifications.*

*Another section describes the Atomic Force Microscope and the X-Rays Diffractometer, which have been extensively used during this thesis, but for which I have been a normal user.*

### 2.1 Dual chamber Evaporator

All the devices described in this thesis have been fabricated in a dual-chamber ultra-high vacuum (UHV) evaporator system fabricated by Theva (Figure 2.1a). The evaporator is composed by two main chambers and a load-lock. One of the main chambers is dedicated to the deposition of metals and the other one to the deposition of molecules; the load-lock allows the insertion of samples without breaking the vacuum in these main chambers. The three chambers are pumped independently with a turbo pump in each chamber. A heating sleeve system covers the main chambers for a straightforward bake-out (Figure 2.1a). After the bake-out process, the base pressure in the main chambers gets below  $10^{-10}$  mbar.

The samples are clamped onto a copper sample holder, which is transferred from one chamber to the other with a magnetic arm without vacuum breaking. The sample holder is designed to fit wafers with a maximum size of 1 inch, and the typical substrate size employed in this work is  $5 \times 5$  mm<sup>2</sup> or  $10 \times 10$  mm<sup>2</sup>.

## 2.1 Dual chamber evaporator

---

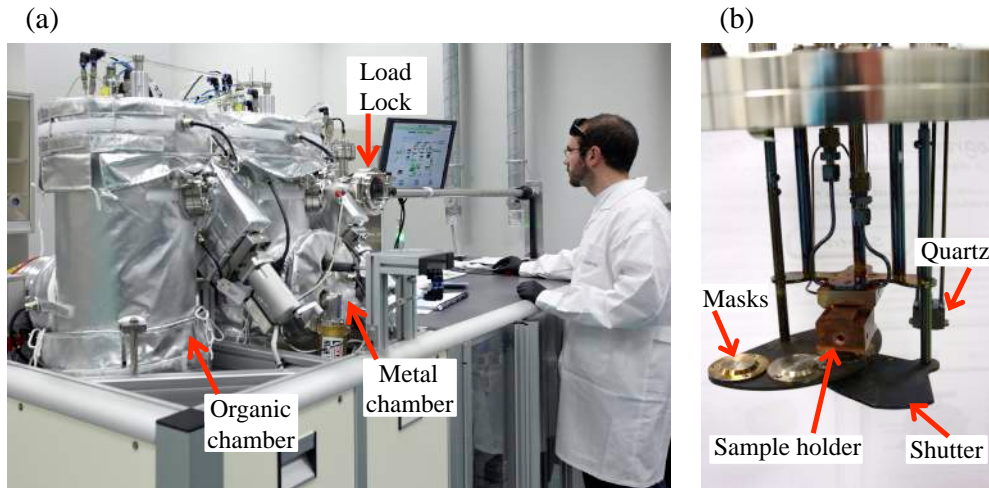


Figure 2.1(a) Dual chamber evaporator. The bake-out sleeves covering the two main chambers are visible. (b) Top flange of one of the main chambers. The most important features are labeled.

The top flanges of the two main chambers (Figure 2.1b) possess a sample stage to fit the sample holder, a thickness monitor, a shutter and a mask holder. The sample stages can be cooled with water and are equipped with a thermocouple for monitoring the temperature. The sample stage in the organic chamber and in the load-lock can be heated up to 250°C with a resistance, while in the metal chamber it can be cooled down with liquid nitrogen, reaching a minimum temperature between 100-105 K.

A crystal monitor measures the amount of evaporated material. Its calibration is kept accurate by measuring the actual thickness of the deposited layers with X-Rays reflectivity whenever the source material is refilled. A shutter between the sample and the material source can be opened and closed by a pneumatic actuator controlled by software, so that the deposition can be started when the desired deposition rate is reached.

The 2 main chambers possess a shadow masking system. Indeed, all the devices described in this thesis have been patterned by evaporation through shadow masks on the substrate. In this technique, a pattern is drilled into a metal foil – the mask –, which is placed in the proximity of the sample during the deposition. Therefore, the material is only deposited on the substrate through the apertures in the mask, so that the pattern on the substrate mimics the shape of the mask. This fabrication technique allows in-situ device patterning without any kind of lithography. Its drawback is that the smallest feature size is rather big (on the order of 100  $\mu\text{m}$ ), being limited by the mechanical accuracy of the drilling process. The two main chambers are equipped with a mask

holder that can host four different masks. Each mask can be positioned in front of the substrate with a manual displacement of the mask holder. In order to minimize the lateral misalignment in successive evaporations, each mask is mounted onto a conical holder that fits into the sample holder (Figure 2.1b). Due to the tolerances of this system, the error in the adjustment in successive evaporations is on the order of 50  $\mu\text{m}$ . However, as 4 masks are not sufficient to account for all the on-going projects, we have designed a new mask holder with smaller alignment cones that can fit 8 shadow masks.

### 2.1.1 Load lock

The load lock is used for the insertion and removal of substrates without breaking the vacuum in the main chambers. In this way, the main chambers are vented and opened only to refill or change the evaporation materials.

Furthermore, the load lock is designed to perform low power plasma treatments. After a base pressure below  $10^{-6}$  mbar is reached, it is possible to insert Oxygen or Argon into the chamber with the turbopump rotating at reduced speed (200 Hz instead of 1000 Hz). The gas pressure can be stabilized in the range of 0.05-0.1 mbar, and the plasma can be ignited by applying a high voltage between the sample stage and a glow discharge plate positioned below the sample. The maximum plasma power is 60 W (1200 V and 50 mA). The oxygen plasma has been extensively used for oxidizing Al films and form  $\text{AlO}_x$  tunnel barrier.

### 2.1.2 Metal chamber

Metals are evaporated by electron-beam evaporation in a chamber dedicated exclusively to this purpose. The principles of the e-beam evaporation are well established [1]. An electron beam is generated for thermionic emission by passing current through a filament (figure 2.2a). The e-beam is focused by a magnetic field and accelerated towards the evaporation material applying a high voltage. The impact of the electrons with the material converts part of the kinetic energy of the electrons into heat, causing the material to sublime and deposit onto the substrate.

## 2.1 Dual chamber evaporator

---

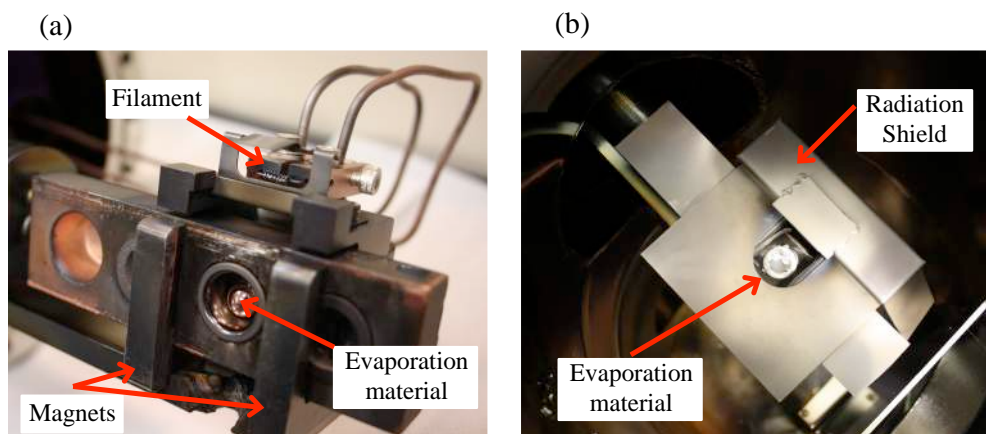


Figure 2.2(a) e-beam evaporator: electrons emitted by a filament are accelerated by a high voltage and deflected by permanent magnets towards the evaporation material. (b) Metal chamber view from the top. The home-designed radiation shield is highlighted.

In our evaporator, we employ a Telemark 528 e-beam source with 4 pockets (fig. 2.2a), which is UHV-compatible. While the base pressure in the chamber is in the range of  $10^{-11}$  mbar, during metal deposition it is typically in the  $10^{-7}$  mbar range. The e-beam power supply has 3 kW maximum power, and each pocket has a capacity of 1.5 cc. Compared with other e-beam evaporators, in which the typical pocket size is 15 cc and the maximum power source 10 kW, in our system the pocket capacity and the evaporation power are relatively low. However, they are adequate to the small chamber size – the internal diameter of the chamber is 25 cm and the material source is placed just at 20 cm from the sample. Such a small distance presents some advantages and some disadvantages. On one hand, the evaporation is very efficient, because the amount of the deposited material on the chamber walls is minimized. This efficiency is crucial when working with small pocket sizes, because otherwise the material would last for only a few evaporations. On the other hand, one should be very careful when depositing a metal on top of a molecular layer, because the radiation emitted during the e-beam evaporation might damage the molecular layer [2–5].

To check the level of damage induced to a molecular layer by a metal evaporation, we deposited a metal on top of patterned PMMA films. PMMA is a polymeric material extremely sensitive to irradiation of electrons and UV or x-ray light, that is why it is commonly used as a high resolution positive resist for direct write e-beam as well as x-ray and deep UV microlithographic processes. When it is exposed to a high radiation dose, it becomes insoluble in acetone, representing our ideal test platform to evaluate

the amount of radiation reaching the sample. In early attempts, during the deposition, the PMMA became regularly insoluble in acetone, meaning that a high irradiation dose was reaching the sample. In order to diminish it, we designed a radiation shield to be inserted between the filament and the sample (figure 2.2b). In this way no direct light from the filament reached the sample. We found that using the radiation shield and an evaporation power below 1 kW, the radiation dose reaching the sample is diminished enough to leave reproducibly the PMMA not over-exposed, i.e., soluble in acetone. The results presented in this thesis were measured on samples grown after the shield was inserted, when we were confident that the irradiation during deposition was not damaging the molecular layer.

The aluminum evaporation also required a long optimization. Al is known to be a problematic material for evaporation, as it tends to wet its crucible and eventually crack it. We found that we could not evaporate Al reliably if we used boron nitride (BN) liners, which are often used for the e-beam evaporation of Al [6]. In our system, Al wets the whole BN liner and touch the water-cooled copper support. Therefore, a thermal short circuit would prevent the Al evaporation at low power, introducing two main disadvantages. First, when the evaporation power is too high (above 1 kW), the deposition above a molecular layer damages it, even with the shield in its position. Second, the pressure in the chamber raises above  $5 \times 10^{-7}$  mbar, worsening the quality of the deposited Al. In particular, we found that in some cases the Al film was optically almost transparent and not conductive. The solution to these problems was to employ liners of different materials other than BN. In particular, we found that the Al deposition from  $\text{Al}_2\text{O}_3$  liners was much more controllable, as Al did not wet and creep.

As a further modification to the chamber, we changed the sample cooling system. At the beginning, the sample stage could be cooled to 22°C by flowing water through it. In order to decrease the minimum sample stage temperature, we designed a new cooling system with liquid nitrogen. As expected, the quality of the metals improved, both in terms of lower resistivity and lower surface roughness (see next chapter).

### 2.1.3 Organic chamber

Organics are thermally evaporated in a dedicated chamber. Compared to the metal chamber, the organic chamber required much less hardware optimization. The chamber is equipped with three low-temperature effusion cells purchased from MBE-komponenten (figure 3a, 3b). Molecules in powder form are inserted into an elongated Quartz crucible (also purchased from MBE-komponenten) inside the effusion cell. A

## 2.1 Dual chamber evaporator

---

small filament uniformly heats the crucible along its entire length. When the temperature is high enough, the molecules sublime and are deposited on the sample.

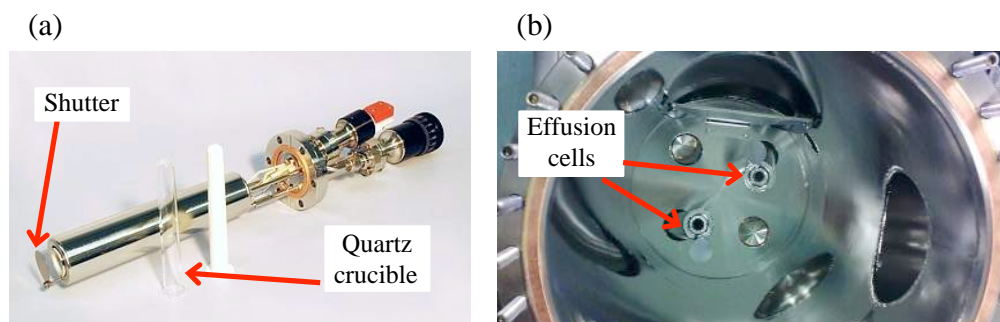


Figure 2.3 (a) Effusion cell with one quartz crucible. (b) Organic chamber view from the top. Two effusion cells are mounted, and two other ports are available for additional cells.

The temperature is measured by a thermocouple in direct contact to the crucible wall and it is controlled by software through an EpiTemp controller. Apart from the shutter mounted on the chamber flange, the effusion cells possess a shutter close to the evaporation material. In this way, while the temperature is ramped up, the molecules are deposited on the shutter and not on the chamber walls. The maximum temperature that cells can reach is 800°C, well above the sublimation temperature of most small molecules (the maximum temperature reached in this project was 450°C). The organic evaporation becomes as easy as setting the molecule sublimation temperature in the software and control the deposited thickness via the quartz crystal monitor. The base pressure in the chamber is in the low  $10^{-9}$  mbar range, and during the molecule sublimation, it typically remains below  $10^{-8}$  mbar.

## 2.2 Probe Station

The electrical measurements presented in this thesis have been performed in one of two similar LakeShore probe stations (Fig. 2.4a). The actual electrical contact to the sample is achieved through four tips controlled by micrometric actuators (Fig 2.4b), connected via triaxial cables to the measuring instruments. Each probe station contains two radiation shields for minimizing external noise.

## 2. EXPERIMENTAL METHODS

The two probe stations are able to perform measurements in vacuum with an applied magnetic field and at low temperatures. The base pressure at room temperature is below  $p=2 \times 10^{-5}$  mbar, low enough to prevent rapid degradation of molecular layers. The magnetic field is applied in the sample plane, and has a maximum value  $H=0.6$  T. The sample can be rotated  $90^\circ$  with an external rotator when the chamber is under vacuum, in order to apply the magnetic field in different in-plane directions. The cooling system represents the main difference between the two probe stations: one is equipped with a compressor which can cool the sample stage down to 4.9 K, and the other one can be cooled down with liquid nitrogen or liquid helium down to a nominal minimum temperature  $T=7$  K. In this thesis, the second probe station has only been cooled with liquid nitrogen to a minimum temperature close to  $T=77$  K. However, in both probe stations measurements as a function of varying temperature are not trivial because of the thermal contraction of the tips, which need to be positioned after the temperature is stabilized.

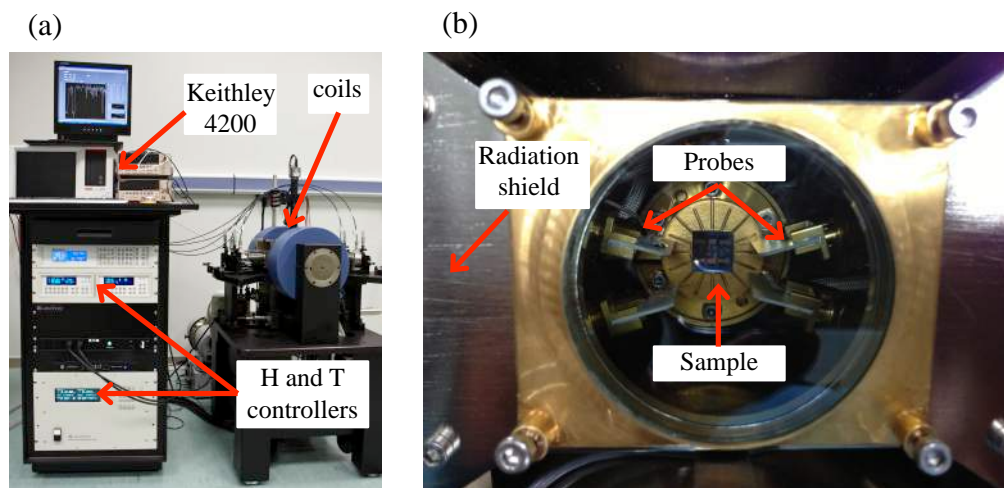


Figure 2.4 The probe station. (a) On the left side, the controllers of temperature and magnetic field and the equipment for electrical measurements are shown, on the right side the sample stage with the probes and the electromagnets. (b) Inside the probe station four probes are used to contact the sample.

The electrical measurements are performed with a Keithley 4200 equipped with three source-measurement units (SMU), two of which possess a current amplifier with sub-femto ampere nominal resolution. Indeed, thanks to the triax cables and the radiation shield, the noise level in our system when the circuit is open (tips not touching a sample) is below 10 fA. During actual measurements the main source of noise is the

## 2.2 Probe Station

---

mechanical instability of the contact between the tip and the sample. In this sense, the noise level depends crucially on the material to be contacted, on its thickness and the conditions of the measurement. In particular, the compressor that lowers the temperature to 4.9 K introduces an unavoidable vibration that generates noise. This mechanical noise can be lowered by cold-pressing Indium on the contacts and leaning the tips against the Indium.

The control and synchronization of the electrical measurements with the magnetic field and the temperature were achieved by the implementation of basic programs in Labview. For the spin-valves, we implemented two software programs. The first one was used for measuring the current-voltage (IV) trace of the device, *i.e.* the current during a voltage sweep at a fixed magnetic field; the other one for measuring the magnetoresistance, *i.e.* the current at a fixed voltage while sweeping the magnetic field. For the measurements of the magnetic tunnel transistors, the software was modified to allow the measurement of current at all the SMU of Keithley 4200 simultaneously, during a magnetic field sweep or during a voltage sweep at one of the SMU.

## 2.3 Atomic force microscopy and X-rays reflectivity

Atomic Force Microscopy (AFM) and X-Rays Reflectivity (XRR) have been widely used during this thesis as tools for the characterization of thin films. In this section, the basic principles of the two techniques will be described, with some technical details about the instrumentation employed.

### 2.3.1 Atomic Force Microscopy

Atomic Force Microscopy is a powerful scanning probe technique that can provide diverse information about a surface [7]. Although different operating modes have been developed, they all rely on the same basic principles. A cantilever terminating in a sharp tip is brought in the proximity of the sample surface. When the tip is close enough, it begins to interact with the sample surface and it is deflected due to different forces, such as mechanical contact, van der Waals, electrostatic and magnetic forces. The deflection is monitored through a laser focused on the cantilever and reflected to a photodetector (figure 2.5a). When the Figure 2.5tip/sample interaction begins, the tip

scans the surface thanks to a piezoelectric actuator. In this sense, the result is a spatially resolved mapping of the forces between the tip and the surface.

Information can be obtained from the different forces acting on the tip depending on the operation mode. During this project, tapping mode AFM has been used to characterize the topography of the samples. In this mode, a piezoelectric element mounted in the tip holder makes the cantilever oscillate at a frequency close to its resonance. When the tip gets close to the sample, the amplitude of the oscillation decreases due to its interaction with the surface. The tip-sample distance determines the oscillation amplitude. In particular, the closer the tip to the surface, the smaller the oscillation amplitude and the stronger the force with which the tip hits the sample. A feedback loop keeps the cantilever vibrating at fixed amplitude by vertically moving the tip closer or further to the sample when the oscillation amplitude tends to increase or decrease respectively. By doing so, the tip follows the surface morphology, and the map of the vertical displacement of the tip as a function of the in-plane coordinates result in a 3D graph that mimics the sample topography.

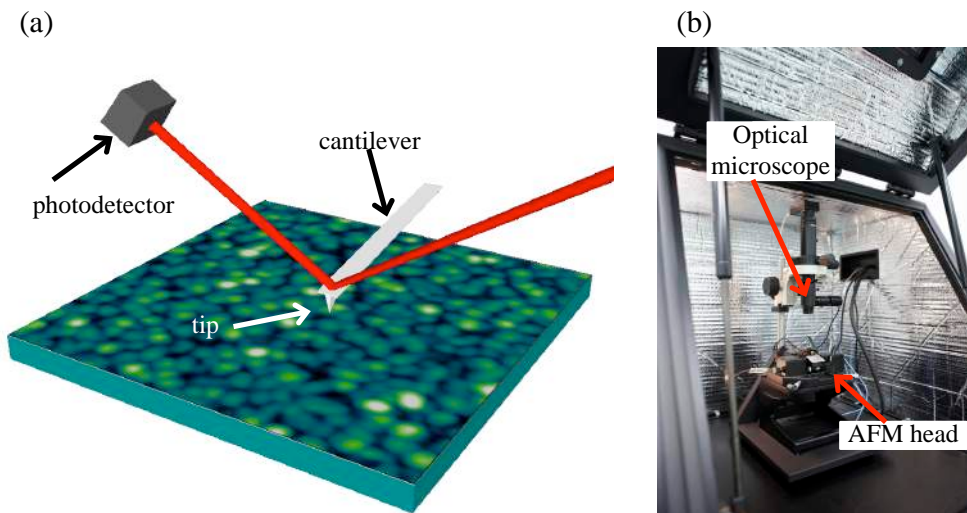


Figure 2.5: (a) AFM cartoon. The position of a cantilever terminating in a sharp tip is monitored, recording the position of a laser reflected on the cantilever. (b) Picture of the AFM used in this thesis. It is enclosed into a cage to reduce the noise, and equipped with an optical microscope for positioning the cantilever in the desired position of the sample.

The resolution of the AFM depends on several factors, the most important being the radius of curvature of the tip and the stability of the piezo. Soon after the invention of the AFM, images showing atomic corrugation were demonstrated [8]. More recently it

## 2.3 Atomic force microscopy and X-rays reflectivity

---

has been shown that controlling the atomic composition of the very apex of the tip allows direct imaging of individual atoms inside a molecule lying on a surface and of the bonds inside the molecule [9,10]. However, for reaching such a resolution, a very clean environment is necessary (ultra-high vacuum), far from the aim of this thesis.

In this work, we used an Agilent AFM enclosed in a cage for minimizing external noise (figure 2.5b). The piezoelectric scanner allows a  $100 \times 100 \mu\text{m}^2$  maximum image size. In this project we were mainly interested in exploiting the capability of the AFM of measuring the surface roughness at the nanometer scale, so the typical image size was  $1 \times 1 \mu\text{m}^2$ . We employed standard AFM tips purchased from Nanosensors, with a tip radius typically below 7 nm, which allow a lateral resolution below 50 nm. In this respect, AFM measurements give information about the small-range roughness, nicely complementing the long-range roughness information obtained in X-rays experiments (see next section).

The Gwyddion software was used to analyze the AFM data. It allows color-scale 2D and 3D rendering of the topography and basic image treatments – for instance, removing a polynomial background, correcting faulty lines or extracting profiles along any line in the image. Moreover, the surface roughness can be characterized with significant parameter that will be widely used in the next chapter. First, the *RMS roughness* represents the “dispersion” of the heights with respect to the mean height, and is calculated using the root mean square of the heights in every point. Another important parameter is the *peak-to-peak* distance, which represent the absolute difference between the highest and the lowest point in the image; there is the option to calculate it using the highest and lowest value of the whole image, in a selected part of it, or in a single line. Finally, the sample topography is often composed by different grains; in that case, the *average grain size* can be extracted from the image.

### 2.3.2 X-Rays Reflectivity

X-Ray Reflectivity (XRR) is a standard nondestructive technique for the characterization of surfaces and thin films [11]. In this technique, an X-ray beam hits a sample with a very low incidence angle. The intensity of the reflected ray is measured, while the incidence angle is scanned a few degrees (2-3). For electromagnetic radiation with wavelength within the X-ray wavelength spectrum, the refractive index of any material is typically below unity. In this condition, according to the Snell law for reflection, there is a critical angle below which the X-rays do not penetrate from air into the material, being completely reflected. Above the critical angle, the electromagnetic waves can penetrate into the sample and the intensity of the reflected rays rapidly

decrease down to a point where no reflection is measured, and all the radiation enters the sample. However, before the reflection intensity vanishes, there is a range in which the incoming radiation is partly reflected at the film surface and partly enters the sample and is reflected at the interface between the substrate and the thin film (figure 2.6 a).

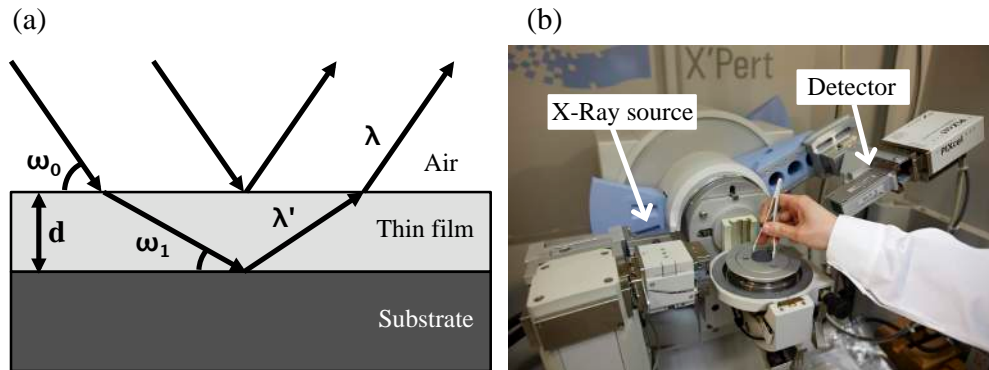


Figure 2.6 (a) X-rays reflected at the film surface and at the film/substrate interface causes an interference pattern. (b) Experimental equipment for XRR measurements.

The two reflected rays interfere constructively or destructively, depending on the difference in the optical path. Therefore, by scanning a few degrees the incidence angle and measuring the intensity of the reflected ray, it is possible to measure interference peaks superimposed to the decay of the intensity of the reflected beam [11]. Analogous to a Bragg reflection, the peak position is related to the separation between the reflecting planes, which in XRR is nothing but the thickness of the film. Indeed, the formula to obtain the film thickness is the Bragg law, modified to take into account the difference in the X-ray wavelength in air and in the thin film:

$$m\lambda' = m\left(\frac{\lambda}{n}\right) = 2d\sin\omega_1 \quad (1)$$

where  $m$  is the interference order,  $\lambda'$  is the wavelength in the film,  $\lambda$  is the wavelength in air,  $n$  the film refractive index,  $d$  is the film thickness and  $\omega_1$  is the incidence angle, as defined in figure 2.6 a.

When the thin film is composed by multiple layers, interference occurs at every interface, and the pattern is more complicated, because it features interference fringes at different angular frequencies. However, it is possible to fit the XRR scan to a structural model for the sample, and obtain information about the thickness of every layer.

### 2.3 Atomic force microscopy and X-rays reflectivity

---

The surface roughness influences the way in which the X-rays are reflected. Eventually, an extremely rough surface would scatter incoherently the incident ray in every direction, and no interference would occur. Therefore, an accurate fit of the XRR results allows an estimation of the interface and substrate roughness. Unlike the roughness obtained in an AFM measurement, the roughness obtained from an XRR scan is related to the long-range surface quality, because the portion of the film under investigation is as wide as the X-ray spot on the sample – which is,  $2 \times 2 \text{ mm}^2$ .

Finally, a XRR scan also provides information on the electronic density of the film, because the film refractive index and the critical angle depend on it.

The XRR measurements were performed in a Panalytical system (figure 2.6b). The system does not only features the hardware for the measurement, but also the software to analyze the measured data. The software “Panalytical X’Pert Reflectivity” allows the simulation and the fitting of experimental data of multilayer structures composed of different materials. A layer in the structure is defined by its thickness, density and roughness, which can be set as free fitting parameters. From the fit one can thus extract a value for the layer thickness, density and roughness.

## 2.4 References:

- [1] K. S. Sree Harsha, *Principles of Physical Vapor Deposition of Thin Films* (2006).
- [2] H. Haick, J. Ghabboun, and D. Cahen, *Applied Physics Letters* **86**, 042113 (2005).
- [3] H. Haick and D. Cahen, *Accounts of Chemical Research* **41**, 359 (2008).
- [4] B. A. C. Dürr, F. Schreiber, M. Kelsch, H. D. Carstanjen, and H. Dosch, 961 (2002).
- [5] J. Rybicki, R. Lin, F. Wang, M. Wohlgenannt, C. He, T. Sanders, and Y. Suzuki, *Physical Review Letters* **109**, 1 (2012).
- [6] Vacuum engineering and materials co, *Thin film evaporation guide* (2008).
- [7] E. Meyer, H. J. Hug, and R. Bennewitz, *Scanning Probe Microscopy: The Lab on a Tip* (2004).
- [8] G. Binnig, C. Gerber, E. Stoll, T. Albrecht, and C. Quate, *Surface Science* **189**, 1 (1987).
- [9] L. Gross, F. Mohn, N. Moll, P. Liljeroth, and G. Meyer, *Science* **325**, (2009).

## 2. EXPERIMENTAL METHODS

---

[10] L. Gross, F. Mohn, N. Moll, B. Schuler, a. Criado, E. Guitian, D. Pena, a. Gourdon, and G. Meyer, *Science* **337**, 1326 (2012).

[11] J. Als-Nielsen, *Elements of Modern X-Ray Physics* (New York, 2001).



## Chapter 3

# Material Characterization

*In this chapter, I focus on the characterization of the thin films of different materials used in this thesis. All the devices described throughout this thesis are composed by the combination between films of  $C_{60}$  molecules and films of different metals. In particular, four metals have been used: Aluminum, Copper, Cobalt and the  $Ni_{79}Fe_{21}$  alloy, known as Permalloy (Py).*

*In section 3.1, I describe the characterization of metals in terms of resistivity and roughness. The resistivity is a good indicator of the metal purity, while the roughness is crucial for avoiding pinholes in vertical devices with ultrathin layers. I show that the quality of Al and Cu films increases when they are deposited with a high deposition rate on a substrate at low temperature. For the ferromagnetic films, the substrate temperature is not crucial. I show that their coercive fields can be measured electrically via the AMR effect.*

*In section 3.2, I expose a detailed study about  $C_{60}$ /Py bilayers. The  $C_{60}$  films grow relatively smoothly on both Py and  $SiO_2$  substrates, and we estimate that a 5-nm-thick  $C_{60}$  film covers completely the surface underneath, without leaving pinholes and can be therefore used in a vertical device. Furthermore, the  $C_{60}$  film is robust against the deposition of the top metal electrode, being the intermixing layer of 1–2 nm at the  $C_{60}$ /Py interface. Finally, we show that the magnetic properties of Py are not affected by the deposition sequence, and that a 5-nm-thick Py layer on top of a  $C_{60}$  layer keeps its magnetic properties intact.*

### 3.1 Metal characterization

Metals were purchased from Kurt Lesker in pellets with purity 99.95% for cobalt, permalloy and copper and 99.99% for aluminum. However, evaporation materials react with the molecules of residual gas in the chamber during deposition, [1] so that the purity of the thin film is not as good as the original pellets. In order to maximize the

### 3.1 Metal characterization

---

purity of the deposited films, it is crucial to work in an extremely clean environment. Indeed, the metal chamber is kept in ultra-high vacuum, with base pressure below  $10^{-10}$  mbar (see chapter 2). To reach such a good vacuum, a six-hour bake out at  $200^{\circ}\text{C}$  is performed every time the deposition chamber is opened. Additionally, all the materials are heated up before the first deposition in order to degas all the molecules adsorbed by the pallets. During this degassing procedure, the pressure increases to  $p > 10^{-6}$  mbar when the material begins to evaporate, and decreases to  $p < 3 \times 10^{-7}$  mbar after the evaporation of a few nanometers (10-15 nm) of material. In the following depositions, the pressure typically remains below  $2 \times 10^{-7}$  mbar.

The resistivity in a resistor is defined as

$$\rho = \frac{RA}{l} \quad (1)$$

where  $R$  is the electrical resistance,  $A$  is the cross-sectional area of the wire and  $l$  is the wire length. Given this definition, the resistivity does not depend on any geometrical factor, so it is an intrinsic property of the material. Impurities increase the resistivity of metals [2–4], so that the resistivity is a good indicator of the metal purity: the closer is the thin film resistivity to the bulk resistivity of the pure metals, the purer the material is.

However, the resistivity of the material depends also on other parameter of the thin film, such as the size of the crystalline grains and the surface roughness. In fact, scattering at the grain boundaries and at the surface increases the resistivity of thin films compared to bulk metal. [5,6] In extreme cases in which the film roughness is on the same order of film thickness, the film might not be continuous, and therefore not conductive. [7] For this reason, the structural characterization of the metal growth is complementary to the resistivity measurements. This characterization, performed with AFM and XRR (chapter 2), gives important additional information about the possibility to use a metal film in vertical devices, where the roughness of the layers at the bottom has to be low enough to permit a homogeneous growth of the layers at the top.

Two main parameters influence the purity and the growth of metals:

1. *The deposition rate.* During the deposition, atoms and molecules of both the evaporation metals and residual gases impinge on the substrate in independent events. Gas molecules can react with the metal and get trapped into the film as impurity inclusions. The probability of this event depends on the reactivity of both the metal and the gas. In general, the film purity will be higher at higher deposition rates, as this minimizes the relative rate of gaseous impurity inclusion. [8] In turn, the deposition rate influences the growth of the thin films.

Materials deposited at high rates possess more energy to diffuse on the substrate, producing films with bigger grains. [9]

2. *The temperature of the substrate.* The substrate temperature influences both the material purity and the film morphology. When the substrate is cooled with liquid nitrogen, molecules of the residual gases condensate onto the cooling system parts inside the chamber. Therefore, the pressure is further lowered and the deposited material is more pure. The substrate temperature also influences the metal growth. At low temperatures (100 K), the evaporated atoms have less energy to diffuse and redistribute on the substrate. Films of the same material grown at different substrate temperatures might have very different topography. [1,9]

In this section, I will show the characterization of our metals in term of resistivity and morphology, highlighting the role of the substrate temperature and of the deposition rate.

#### 3.1.1 Non-magnetic metals

Aluminum is the non-magnetic metal that has been used more throughout this thesis. We exploited its capability to react with oxygen to form a uniform oxide layer suitable for tunneling. Indeed, when Al is exposed to O<sub>2</sub>, an insulating Al<sub>2</sub>O<sub>3</sub> oxide layer is formed at the surface, with a thickness that is chemically self-limited in the tunneling range (1-3 nm) [10]. Reactivity of aluminium, however, makes its deposition very critical because other problems, apart from the technical ones connected with its evaporation, arise. In particular, Al reacts with and incorporates almost all residual contaminants already during the deposition, in particular oxygen [1]. When it is evaporated in a residual oxygen pressure, the film can result totally oxidized and not conductive. [3]

Indeed, when we evaporate Al at low rate ( $< 0.1 \text{ \AA/s}$ ) with the substrate at 20°C, the resulting film is very contaminated. Especially when the material is deposited through a narrow aperture in a shadow mask (a line), it appears non-homogeneous optically, opaque in the center and almost transparent close to the edges. Most probably, the shadow mask itself is degassing during the deposition, so that the film is more contaminated close to the edges. Therefore it is important to characterize the resistivity of the film particularly when it is deposited as a narrow line on the substrate.

### 3.1 Metal characterization

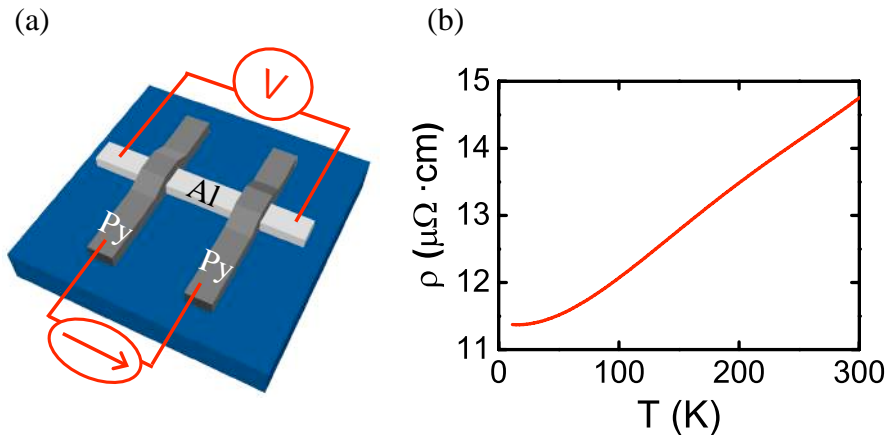


Figure 3.1. (a) Scheme of the resistivity measurement. The width of all the lines in the cartoon is 250  $\mu\text{m}$ . (b) Resistivity of a 15-nm-thick Al line as a function of temperature. Aluminum was deposited at low substrate temperature.

Fig. 3.1 (a) shows a scheme of the device fabricated to measure the resistivity of a 250- $\mu\text{m}$ -wide and 4-mm-long Al line. The 15-nm-thick Al line is deposited on a Si/SiO<sub>2</sub>(150 nm) substrate through a shadow mask. Two 10-nm-thick Permalloy contacts with the same size are perpendicularly deposited on top of it. The current is driven through the Py contact, and the voltage is measured at the Al terminals, as sketched in the figure. This sensing configuration – called four terminal sensing – is widely used to avoid spurious voltage drops in series with the device under measurement. In this particular case, the voltage drop is only caused by the current flowing in the Aluminum itself; the contact resistance and the cable resistance are not measured.

The opaque Aluminum deposited at room temperature with slow rate is not even metallic, with a resistivity  $\rho_{\text{Al RT}} > 10^5 \mu\Omega\text{cm}$ , several orders of magnitude above the nominal Al resistivity ( $\rho_{\text{Al bulk}} = 2.8 \mu\Omega\text{cm}$ ). In order to get reproducibly a homogeneous Aluminum at room temperature, the material has to be evaporated at a high rate ( $r > 2 \text{ \AA/s}$ ). This kind of deposition has some drawback, though. First, the thickness of ultrathin films ( $t < 5 \text{ nm}$ ) is difficult to control with high precision. Furthermore, a high energetic evaporation on top of a molecular layer might result in damages to the molecular layer itself [11–14]. The best compromise between purity and controllability is found with an evaporation rate  $r = 1.0 \text{ \AA/s}$ . Such a rate is not high enough to obtain reproducibly metallic Al lines if the substrate is kept at room temperature, but gives good results when the substrate is kept at low temperature.

Fig. 3.1 (b) shows the temperature dependence of the resistivity of Aluminum deposited with these optimized parameters. The resistivity decreases as the temperature is lowered, a typical feature of metals [2]. At room temperature, we measure  $\rho_{\text{ALIT}} = 14.7 \mu\Omega\text{cm}$ , which has the same order of magnitude of other reported resistivity of Aluminum nanostructures  $\rho_{\text{ALIT}} = 9.09 \mu\Omega\text{cm}$  [15]. Although the higher value we measure might be due to residual contaminations, it is satisfactory for the purposes of this thesis. In the next chapters I will show that this Al is suitable for creating tunneling barriers and making electrical contacts. Additionally, if ultra-pure Al is needed, the recipe is clear: the deposition must occur at a very high rate ( $10 \text{ \AA/s}$ ) onto a substrate kept at 100 K.

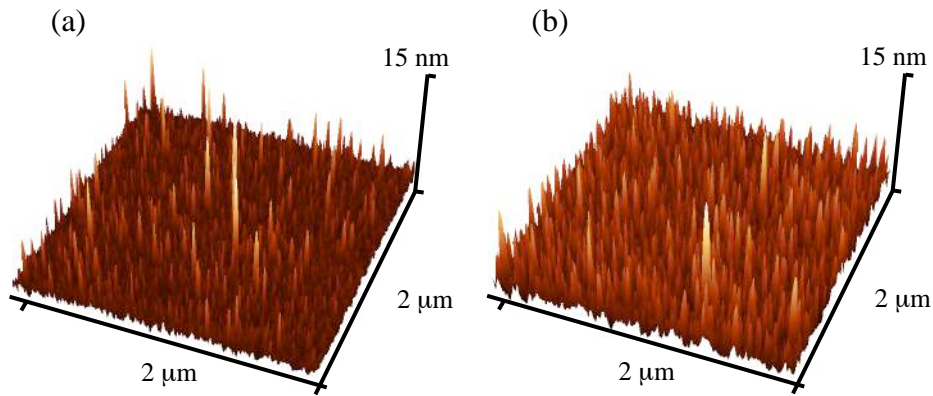


Figure 3.2. AFM images of a 15-nm-thick Al film deposited at a rate  $r = 1.0 \text{ \AA/s}$ , on a Si/SiO<sub>2</sub> substrate kept at 100 K (a) and 300 K (b).

Figure 3.2 shows how the Aluminum surface topography changes at different substrate temperatures. In both cases, the film is rather rough and composed by grains that protrude more than 10 nm from the surface. When the substrate is cold (fig 3.2 (a)), the film is smoother, its r.m.s. roughness being  $R_{\text{LT}} = 0.7 \text{ nm}$  versus  $R_{\text{RT}} = 1.2 \text{ nm}$  at room temperature. As expected [9], also the average diameter of the grains is smaller when the film is deposited at lower temperatures, resulting  $d_{\text{LT}} = 20 \text{ nm}$  and  $d_{\text{RT}} = 50 \text{ nm}$ .

This rather high roughness is not a problem when the Al<sub>2</sub>O<sub>3</sub> barrier is needed on the Al itself, because the oxidation is very uniform over the Al surface, following its roughness [10]. The issue is more critical when Al is deposited on top of another metal to produce an Al<sub>2</sub>O<sub>3</sub>, as will be discussed in more detail in the next chapter.

### 3.1 Metal characterization

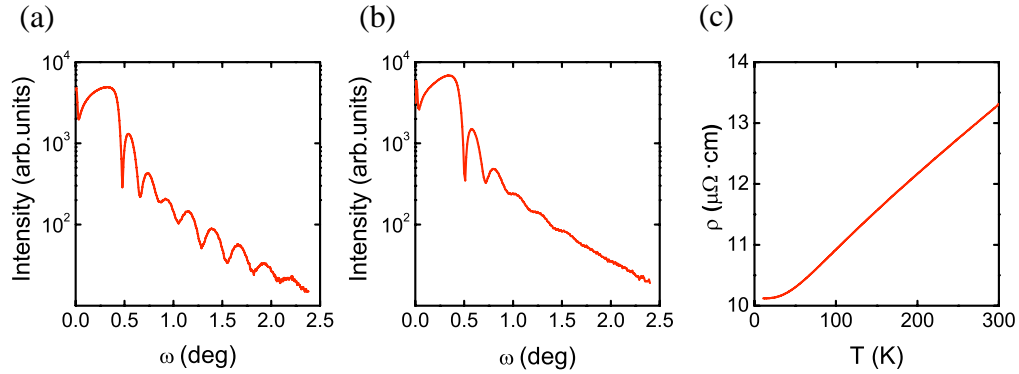


Figure 3.3. XRR Characterization of a 20-nm-thick copper film deposited onto a substrate kept at 100 K (a) and at 300 K (b). The temperature dependence of resistivity of the film produced at room temperature is shown in panel (c).

Copper is the other non-magnetic material that has been used during this thesis. It has been used as a spacer between ferromagnetic layers in all-metallic spin valves (see chapter 5).

Its growth has been characterized at different substrate temperatures by XRR (figure 3.3 a and b). The evaporation rate was kept at  $r = 1.0 \text{ \AA/s}$ . There is a great difference between the scans obtained of the film deposited with the substrate at low temperature (a) and at room temperature (b). In the first case, several interference fringes are visible, indication of an extremely smooth surface [16]. In the second case, the fringes decay rapidly, showing again that the film is rougher when deposited at room temperature.

On the contrary, for copper, the substrate temperature did not affect the transport properties as dramatically as for aluminum. Fig 3.3 (c) shows the temperature dependence of the resistivity of copper deposited at room temperature, measured in a device with geometry similar to the one shown in Fig. 3.1 (a). In this case, even the room temperature deposited copper shows a metallic behavior. Once again the resistivity measured at room temperature  $\rho_{\text{Cu,RT}} = 13.3 \mu\Omega\text{cm}$  is higher than the resistivity reported for copper in nanostructures ( $\rho = 2.8 \mu\Omega\text{cm}$  [17]), indicating that the copper is not extremely pure, but pure enough for the purposes of this thesis.

### 3.1.2 Magnetic metals

The devices that will be described in chapters 4 and 5 are typically composed by different multilayer structures in which two layers are ferromagnetic (FM). Although the devices are very different, in both cases we are interested in the variation of the electrical current caused by a change in the relative alignment of the magnetization of the FM metals – for instance, from parallel to antiparallel. The easiest way to observe the two alignment states is to employ two FM metals that reverse their magnetizations at different values of magnetic field [18], i.e., metals with different coercive fields. We employed Py and Co, for which the coercive fields are intrinsically different. Py is a soft FM metal, and it is expected to exhibit a coercive field lower than Co.

The magnetic properties of a FM metal can be characterized electrically by means of the anisotropic magnetoresistance (AMR). According to the AMR effect, as a result of the anisotropy of spin-orbit scattering in FM metals, their electrical resistance depends on the angle between the electrical current  $J$  and the magnetization  $M$  [19]. When the  $M$  is perpendicular (parallel) to  $J$ , the resistance is lower (higher).

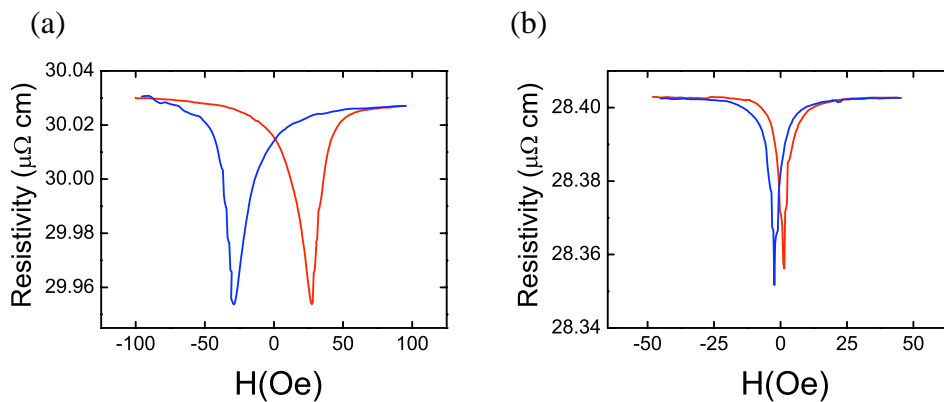


Figure 3.4. Resistivity of a 15 nm thick line of Co (a) and Py (b), as a function of an external magnetic field  $H$ . The metal lines are 4 mm long and 250  $\mu\text{m}$  wide, and the field is applied parallel to the line.

Figure 3.4 shows the variation of the resistivity of a 15-nm-thick line of Co (a) and Py (b) in a sweep of an external magnetic field  $H$  parallel to the lines. The metals were deposited at a rate  $r = 1.0 \text{ \AA/s}$  with the substrate kept at 300 K. Their resistivity  $\rho_{\text{Py}} = 28.4 \mu\Omega \text{ cm}$  and  $\rho_{\text{Co}} = 30.0 \mu\Omega \text{ cm}$  is higher than those reported for FM thin films by

### 3.1 Metal characterization

---

a factor 2 [17], which may be due to some contaminations in the film (see previous section). However, I will show in the next chapters that spintronic devices based on these magnetic layers show good figures of merit.

The dips in the magnetic field sweep (fig 3.4 (a) and (b)) are explained as follows. Looking at the red curve, we see that the external (negative) field initially keeps  $J$  and  $M$  parallel; moving towards positive fields,  $M$  rotates, so the angle between  $J$  and  $M$  changes. Accordingly, a resistivity variation is observed for the AMR effect. Eventually, when the magnetic field is positive and strong enough,  $M$  reverses to align to the new field orientation. When this happens,  $M$  is perpendicular to  $J$  for a while, and because of the AMR effect, the resistivity has a minimum (the dips in fig. 3.4). The same phenomenon occurs when the field is swept from positive to negative fields. The position of the dips indicates at which field  $M$  reverses – i.e., the coercive field. As expected, the coercive fields are different for Co and Py, resulting  $H_{cCo} = 25$  Oe and  $H_{cPy} = 2$  Oe.

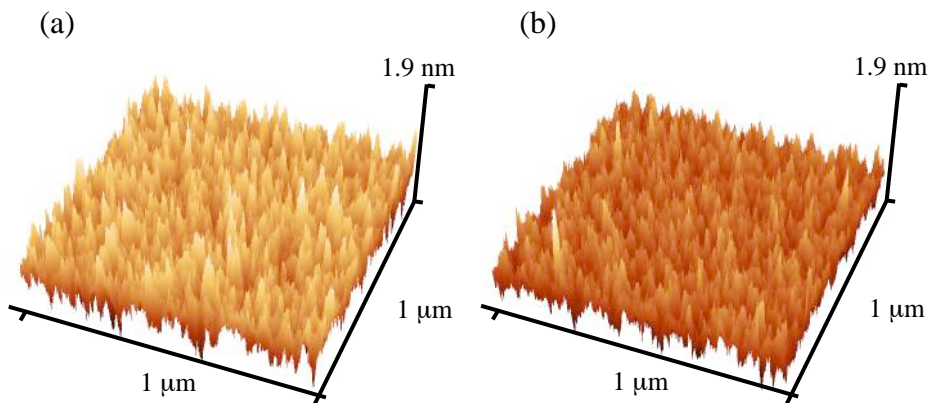


Figure 3.5. AFM images of the surface of a 15-nm-thick Co film deposited at a rate  $r = 0.2 \text{ \AA/s}$  (a) and  $r = 1.0 \text{ \AA/s}$  (b) onto a substrate at room temperature.

Regarding the morphology, fig. 3.5 shows the surface of a 15 nm thick Co film deposited at two different rates  $r = 0.2 \text{ \AA/s}$  (a) and  $r = 1.0 \text{ \AA/s}$  (b). The morphology of Py will be discussed in more detail in the next section. The requirements on the Co roughness are particularly stringent, because Co will be used as the bottom electrode in magnetic tunnel junctions (see chapter 4). In particular, its roughness has to be below 0.3 nm in order to assure that a pinhole-free tunnel barrier with a thickness in the 0.5 - 2.5 nm range can be grown on top of it. Fig 3.5 (a) and (b) show that the Co surface is indeed extremely flat, even when deposited on a substrate at room temperature, with r.m.s roughness  $R < 0.2$  nm.

As we can conclude from the data shown in this section, in most cases we do not need to cool down the sample holder for the FM deposition, because the transport properties and roughness are satisfactory even when deposited at room temperature.

## 3.2 Characterization of C<sub>60</sub>/Py bilayers

The combination between C<sub>60</sub> and Py represents the basis of the devices used in this thesis. In chap. 4, Py will be used as a top contact on top of a thin C<sub>60</sub> layer; in chap. 5, it will be in direct contact with a C<sub>60</sub> thick layer. In both cases, the interaction between the two layers is critical for the properties of the device. Therefore, this section is dedicated to a detailed study of the structural and magnetic properties of Py/C<sub>60</sub> bilayers.

In order to perform the characterization, we have fabricated two different sets of bilayers. In the first set, we deposited a bottom Py layer, with a fixed thickness of 5 nm, and subsequently a C<sub>60</sub> layer with variable thickness (from 5 up to 25 nm) on top of it. In the second set, we reversed the deposition sequence and deposited a bottom 16-nm-thick C<sub>60</sub> layer, covered in this case by a top Py layer with variable thickness (again in the range between 5 and 25 nm). The samples of this second set were completed with the deposition of a 2 nm Al capping layer to prevent the oxidation of the Py layer. All the samples described here were grown on Silicon substrates covered by a thin SiO<sub>2</sub> native layer. C<sub>60</sub> was purchased from Sigma Aldrich (99.9% pure).

The structural properties are studied with AFM and XRR, while the magnetic characterization was performed combining absolute magnetization and magneto-optical hysteresis loops. Magnetization was measured in a Quantum Design VSM-SQUID magnetometer, while magneto-optical data were recorded in a home-made magneto-optical Kerr effect (MOKE) apparatus [20].

For the growth of vertical spin valves with thin molecular layers sandwiched between two metallic contacts, some constraints need to be fulfilled by both the molecular and the metal layers:

(1) The molecular layer needs to grow smoothly, with low surface roughness, covering completely the bottom metal contact after the deposition of a few monolayers. In this way, the metal film grown on top of the molecular layer would be in contact with the molecules only, without touching directly the metal underneath (pinholes). Furthermore, a low surface roughness is important to achieve homogeneous conductance through the molecular layer, since if the surface is very rough, the current will mainly flow through those regions that present the lowest thickness.

## 3.2 Characterization of C<sub>60</sub>/Py bilayer

---

(2) The top metal contact should not penetrate deeply in the organic layer during the deposition. Certain intermixing layer at the metal-organic interface is probably unavoidable [11–14], but it should be as thin as possible (on the order of 1 nm).

(3) In order to form an optimal spin injector, the FM metal layers need to maintain their magnetic properties intact, either when they are deposited at the bottom or at the top of the vertical structure.

In this section we show how the Py/C<sub>60</sub> system fulfills the three conditions listed above, making it a promising testing platform in molecular spintronics.

### 3.2.1 AFM Characterization

The surface information obtained by AFM is summarized in Figure 2. Figures 3.6 (a)–(c) refer to the set of Py/C<sub>60</sub> samples in which Py is the bottom film and C<sub>60</sub> the top one.

Fig. 3.6 (a) shows an AFM micrograph of a single 5-nm-thick Py film grown on the Si/SiO<sub>2</sub> substrate. The analysis indicates that the film is a polycrystal formed by flat nanosized grains with an average lateral grain size  $d = 15$  nm. Its surface is extremely smooth, with a rms roughness  $R = 0.19$  nm across a  $1 \times 1 \mu\text{m}^2$  image (Fig 3.6 (a)). Fig. 3.6 (b) shows the surface of a Py (5 nm)/C<sub>60</sub> (3 nm) bilayer. In this case, although the average lateral grain size of the topmost C<sub>60</sub> surface is also around 15 nm, as for the plain Py film, the rms roughness is much higher, being  $R = 0.43$  nm and with a peak-to-peak value in excess of 3 nm (Fig 3.6 (b)). Comparing this roughness with the outer diameter of the C<sub>60</sub> molecule (diameter around 1 nm), we estimate the overall roughness to be about 3–4 molecular layers. The fact that the layer roughness is comparable with the layer thickness suggests that the coverage of the Py surface may be discontinuous. Therefore, such a thin C<sub>60</sub> layer is not suitable for the growth of a vertical device, as pinholes are very likely to form upon the deposition of a top metal contact. In the samples with thicker C<sub>60</sub> layers, the lateral grain size slightly increases, reaching an average value  $d = 25$  nm for the 25-nm-thick film (a direct comparison can be done by inspection of figures 3.6 (b) and (c)). However, the rms roughness of the C<sub>60</sub> layer surface does not change significantly with its thickness, as it is maintained in the range  $R = 0.4 - 0.5$  nm with peak-to-peak roughness in excess of 3 nm (Fig 3.6 (b)–(c)). Given these r.m.s and peak-to-peak roughnesses, we estimate that a 5-nm-thick C<sub>60</sub> film forms a continuous layer on the metal surface, and hence it can be used as interlayer in a vertical device.

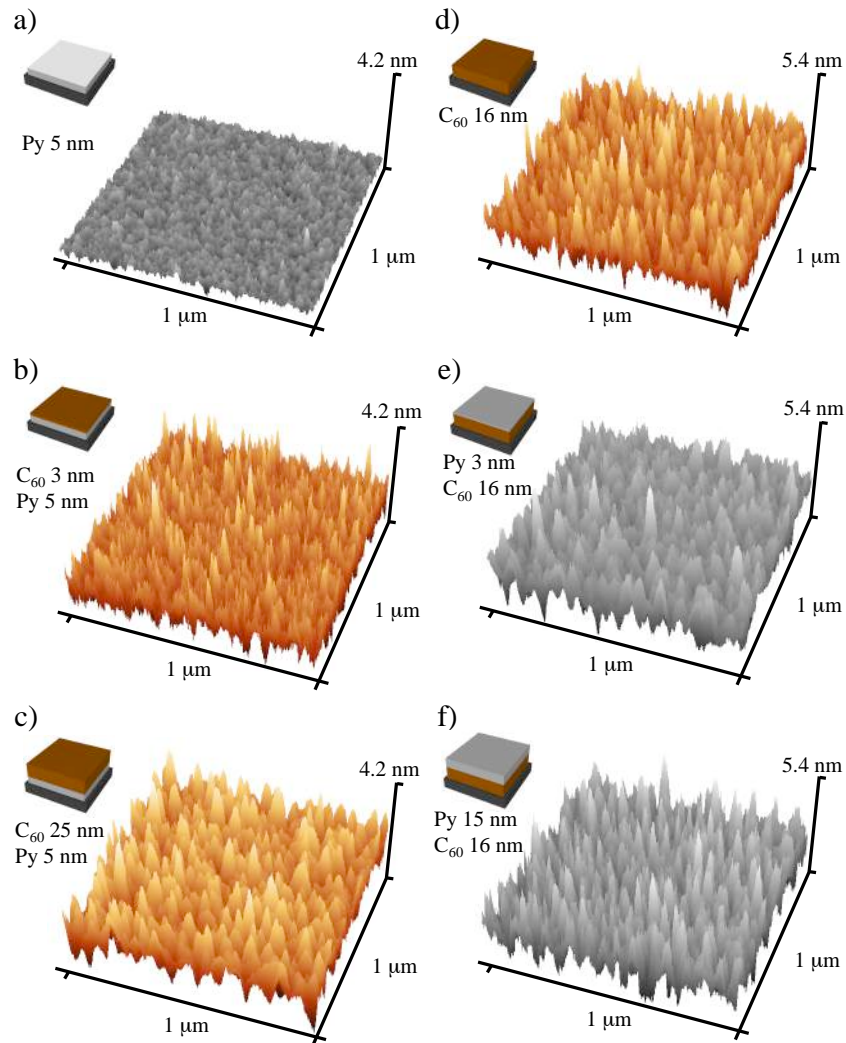


Figure 3.6. AFM characterization of Py/ $C_{60}$  and  $C_{60}$ /Py bilayers. Py surfaces are shown in grey scale,  $C_{60}$  surface in brown scale. (a-c) Images of samples Py/ $C_{60}$ , Py below  $C_{60}$ : (a) surface of a 5 nm Py layer with no top  $C_{60}$ ; (b) 5 nm Py covered by 3 nm  $C_{60}$ ; (c) 5 nm Py covered by 25 nm  $C_{60}$ . (d-f) Images of samples  $C_{60}$ /Py, with  $C_{60}$  below Py: (d) surface of 16 nm  $C_{60}$  with no top Py; (e) 16 nm  $C_{60}$  covered by 3 nm Py; (f) 16 nm  $C_{60}$  covered by 15 nm Py.

We now turn our attention to the topography of the Py films grown over a fullerene underlayer (Figs. 3.6 (d)-(f)). A 16-nm-thick  $C_{60}$  layer deposited directly on the substrate is shown in Fig. 3.6 (d). This layer is formed by grains with an average lateral size of 20

## 3.2 Characterization of C<sub>60</sub>/Py bilayer

---

nm, in good agreement with AFM data reported in literature [21]. In this case, the rms roughness is  $R = 0.65$  nm, with the peak-to-peak roughness in excess of 3.5 nm. This peak-to-peak roughness shows that the morphology of the C<sub>60</sub> layer surface is substantially independent of the substrate utilized, either SiO<sub>2</sub> or Py. When a Py layer is grown on top of the 16-nm-thick C<sub>60</sub> film, its surface morphology mimics that of the C<sub>60</sub> layer underneath, both in terms of grain size and of surface roughness, irrespective of the Py thickness. The peak-to-peak roughness value of  $\sim 3 - 3.5$  nm sets the limiting thickness required for obtaining a continuous layer both in the Py and C<sub>60</sub> case. For the case of a thin Py layer (thickness  $< 4$  nm), its discontinuous film structure is confirmed by the magnetic characterization of the samples (see next section).

### 3.2.2 XRR Characterization

In addition to AFM, we have also used x-ray reflectivity (XRR) to check the layer thickness and homogeneity on a larger scale (mm<sup>2</sup> compared to  $\mu\text{m}^2$  for the AFM analysis). Interference fringes are present in XRR scans on both single Py and C<sub>60</sub> layers of similar thickness (Figs. 3.7 (a) and (b)), confirming the high quality of the surfaces under study. In the particular case of a single Py film, the fringe patterns extend up to an angle of 3 degs., while in a single C<sub>60</sub> layer they are no longer discernible from the noise background above 1.5 degs. This fact indicates that the large area roughness of Py is lower than for the C<sub>60</sub>, in good agreement with the AFM measurements (see previous section). From the XRR fittings we extract a large area roughness  $R = 0.4$  nm (for the Py film) and  $R = 1.4$  nm (for the C<sub>60</sub> film). Following the overall analysis of both AFM and XRR data, we can conclude that the Py/C<sub>60</sub> system fulfills the first condition listed above for a material to become a suitable test platform for molecular spintronics.

We move now into the second requirement of the criteria outlined above. For this purpose, information on the damage caused to the molecular layer by the top metal deposition can be obtained by comparing XRR scans taken from a molecular layer before and after the deposition of a top metal layer [22]. The procedure applied is the following: we first measured a XRR scan on a single C<sub>60</sub> layer deposited on top Si/SiO<sub>2</sub> (Fig. 3b). Afterwards, we placed the very same sample back in the evaporation chamber and deposited a 8-nm-thick Py layer on top. The XRR scan measured on the full bilayer after the metal deposition is shown in Fig 3.7 (c).

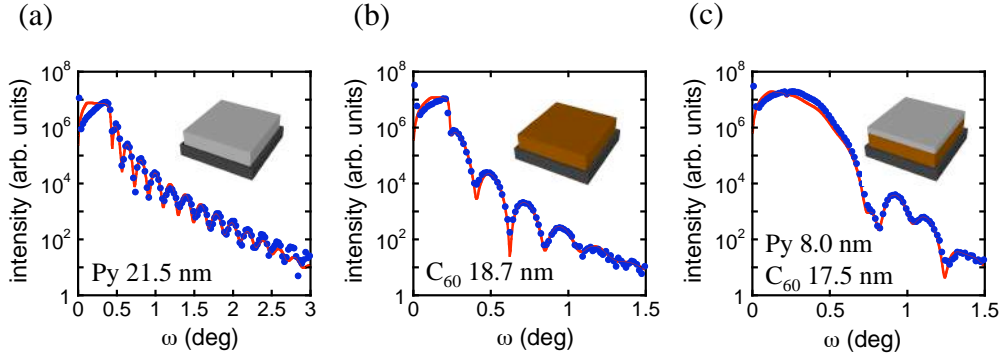


Figure 3.7. X-ray reflectivity characterization of Py/ $C_{60}$  layers. Experimental data are shown as blue dots; the red line is the fit obtained by modeling the sample as (a) a single Py layer, (b) a single  $C_{60}$  layer, (c) a  $C_{60}$ /Py bilayer. The thicknesses displayed in the figure are those obtained from the fit.

The fit to the data shown in fig. 3.7 (b) (red line) provides us with values of the layer thickness (18.7 nm), roughness (1.4 nm) and density ( $1.6 \text{ g/cm}^3$ ). These values were obtained by using as starting parameters in the fitting procedure the nominal thicknesses given by a thickness monitor during the deposition (20 nm), the roughness obtained by AFM measurements (0.65 nm), and the  $C_{60}$  nominal density ( $1.6 \text{ g/cm}^3$ ). In the case of the fit to the XRR data of the  $C_{60}$ /Py bilayer (fig. 3.7 (c), red line), the starting parameters for the  $C_{60}$  layer are the values provided by the fit of the uncovered layer, while for the Py, we used its nominal thickness (8 nm) and density ( $8.72 \text{ g/cm}^3$ ). From the fit, we obtain for the  $C_{60}$  layer the same density ( $1.6 \text{ g/cm}^3$ ) and for the Py layer a density ( $8.8 \text{ g/cm}^3$ ) and a thickness (7.8 nm), in good agreement with the expected values. Interestingly, we find that the  $C_{60}$  thickness diminished from 18.7 nm down to 17.5 nm after the deposition of the top metal. We can assume that after the metal deposition on the fullerene, exactly at the  $C_{60}$ /Py interface, an ill-defined layer with a thickness of approximately 1-2 nm is formed. The thickness of this layer is extremely thin compared to the damage reported for other molecular layers after a metal deposition [13,14,23].

From the data presented above we prove that the  $C_{60}$ /Py system fulfills as well the second condition proposed above (thin intermixing layer, on the order of 1 nm) for making it a suitable metal-organic reference system for molecular spintronics.

### 3.2.3 Magnetic Characteriation

After having discussed the morphological properties of the Py and fullerene layers, we should turn now our attention to the magnetic properties of the metal film (see condition three in page 58). It is clear that for producing optimum devices, the Py layer must conserve its magnetic properties unaltered when deposited either below or above a molecular layer.

It is generally expected that a molecular layer deposited on top of a FM metal would not affect dramatically the magnetic properties of the latter, although issues such as oxidation or a strong metal-molecular bonding have to be taken into account carefully [24,25]. In the opposite case, when a FM layer is on top a molecular one, it is not obvious to what extent the roughness of the molecular sub-layer affects the magnetic properties of the FM film [26–28]. In particular, the magnetic properties of the ill-defined layer at the interface need to be investigated.

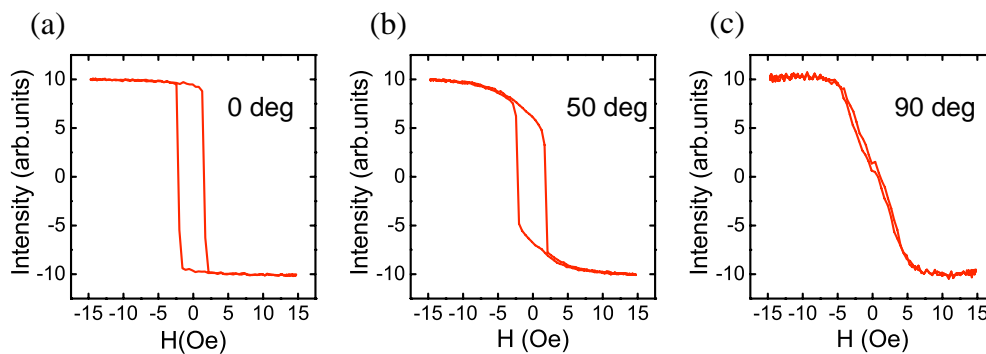


Figure 3.8. Hysteresis loops for a 5-nm-thick Py capped with a 2-nm-thick Al layer film measured at different in-plane angles between the sample and the magnetic field: 0 deg, 50 deg and 90 deg.

First, we analyze the magnetic properties of a single layer of Py grown on the substrate without C<sub>60</sub>. Figure 3.8 shows the hysteresis loops for a 5-nm-thick Py layer with a 2-nm-thick Al capping layer measured with the MOKE setup. The hysteresis loops recorded at different angles between the in-plane magnetic field and the sample are very different. At a particular angle (arbitrarily called 0 deg), the loop has a square shaped hysteresis (a); when the angle is changed, the loop shape becomes smoother and narrower (b), until the hysteresis almost disappears for a loop recorded at an angle 90 degs rotated with respect to the initial one. Such a behavior indicates that there is a

direction, that we call 0 deg, that is energetically more favorable for the magnetization. In other words, the film exhibits uniaxial magnetic anisotropy, with an easy axis in the 0 deg direction. This anisotropy is probably due to a small remnant field at the sample stage during the deposition, induced by the magnets that accelerate the electron beam (see chapter 2). In agreement with this hypothesis, the easy axis direction roughly corresponds to the same physical direction of the evaporator for every sample.

The characterization of the magnetic properties of the different  $C_{60}/Py$  films has been done focusing on the two most representative parameters that define the magnetic hysteresis loop: the coercive field ( $H_c$ ) and the saturation magnetization ( $M_s$ ).

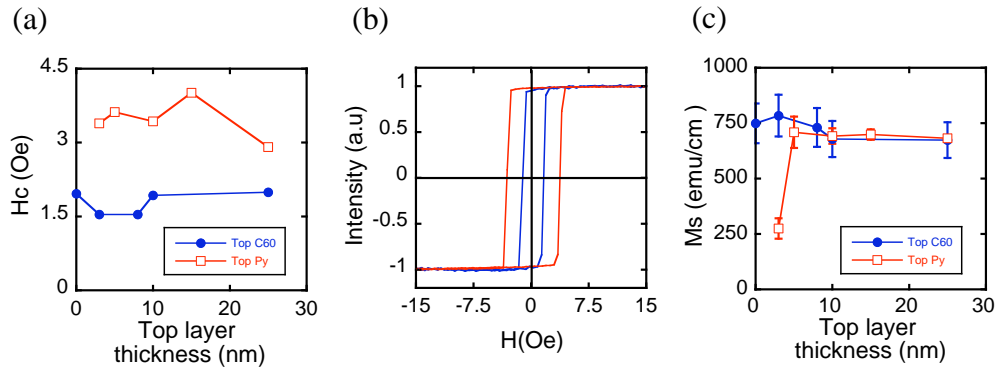


Figure 3.9. : Magnetic characterization of  $C_{60}/Py$  bilayers. Coercive field and magnetization are shown for 2 sets of samples: in the first set, Py layers of fixed thickness (5 nm) are covered by  $C_{60}$  layers with variable thickness; in the second set,  $C_{60}$  layers of fixed thickness (16 nm) are covered by Py layers with variable thickness. For the first sample set,  $H_c$  and  $M_s$  are plotted as a function of the thickness of the top  $C_{60}$  layer (blue closed data in fig. a and c respectively). For the second set,  $H_c$  and  $M_s$  are plotted as a function of thickness of the top Py layer (red open data in fig. a and c respectively). The main error source comes from the thickness of the FM layer, which we estimate in 0.5 nm. Fig. b shows the hysteresis loop of a 5-nm-thick Py when it is placed below a 8 nm  $C_{60}$  film (blue closed circles) and above a 16-nm-thick  $C_{60}$  film (red open squares).

For the first set of samples, in which  $C_{60}$  layers of different thicknesses cover a 5-nm-thick Py film, the  $H_c$  values are displayed in blue in figure 3.9 (a). The coercive field  $H_c$  gives us information regarding the relation between the external applied magnetic field and the energy required for reversing the magnetization direction. We include only the  $H_c$  values measured along the easy-axis for a consistent comparison between different samples. Figure 3.9 (a) shows that the  $C_{60}$  grown on top of the Py film has not any influence on its hysteresis loop. The coercive fields recorded are all in the range from

### 3.2 Characterization of C<sub>60</sub>/Py bilayer

---

1.5 Oe to 2 Oe, very close to the value obtained in the case of a plain Py film without any C<sub>60</sub> above (first blue point in Fig. 3.9 a). The red open symbols and line in Figure 3.9 (a) refer to the H<sub>c</sub> for the inverse set of samples in which different thicknesses of Py are deposited on top of the C<sub>60</sub> underlayer. In this case, the average coercive field increases up to 3.5 Oe for the Py films grown on top of C<sub>60</sub>. This difference can be also visualized in Figure 3.9 (b), which shows the hysteresis loop of a 5 nm Py layer placed as top and bottom electrodes (blue and red curves, respectively). The significant difference in H<sub>c</sub> is due to the intrinsic roughness of the underlying C<sub>60</sub> layer (see above), which creates magnetic pinning sites (orange-peel like effect [29]) in the top Py film [26–28]. In any case, although the difference in the coercive field of the two cases is relatively very large, its absolute value remains very small.

Fig 3.9 (c) shows the saturation magnetization for the 2 sets of samples (blue and red symbols refer to the magnetic Py films placed as bottom or as top electrode, respectively). From the inspection of fig. 3.9 (c), we can conclude that the M<sub>s</sub> values of the Py underlayer are also not affected by the growth of the C<sub>60</sub> layer on top, i.e., M<sub>s</sub> is constant within the error bars, irrespective of the amount of molecules deposited on top of the Py underlayer. Note that the first blue symbol corresponds to a C<sub>60</sub> thickness equal to 0, so it represents the M<sub>s</sub> of a Py film grown directly on Si/SiO<sub>2</sub>.

In the case of Py top layers, we find that the samples with Py thicknesses above 3 nm have again constant M<sub>s</sub> within the error bar, with a value very close to the M<sub>s</sub> measured for the previous samples. The 3-nm-thick Py layer (first red open symbol in Fig. 3.9 (c)) shows a remarkably different behavior. It is ferromagnetic, because it displays a clear hysteresis loop, but its M<sub>s</sub> value of 270±20 emu/cm<sup>3</sup> corresponds to almost one third of the average M<sub>s</sub> of the other samples. This considerable drop in the M<sub>s</sub> of this ultrathin layer can be explained considering that: (1) the C<sub>60</sub> surface peak-to-peak roughness is on the order of the Py thickness, so the layer may be not continuous (see above the discussion about the morphological properties of the Py/C<sub>60</sub> system above); (2) the thickness of the ill-defined layer between C<sub>60</sub> and Py that we estimated in approximately 1-2 nm corresponds to almost one half of the Py layer thickness. In summary, the data displayed in Fig. 3.9 (c) points to 5 nm as the lowest thickness of a Py overlayer to be continuous and to present bulk magnetic properties.

In general, all our Py samples (at the top or at the bottom of the C<sub>60</sub>) possess M<sub>s</sub> = 720±70 emu/cm<sup>3</sup>, which is slightly lower than the reported saturation value for bulk Py (830 emu/cm<sup>3</sup>) [30]. This difference may be due to a slight oxidation of Py during the growth. Such a contamination was expected from the electrical analysis mentioned in the previous section.

Following the magnetic characterization performed for the Py/C<sub>60</sub> system, we can now assure that such combination of materials fulfills the third condition required for an ideal material test system in molecular spintronics, as was outlined above.

### 3.3 Conclusions

In this chapter, thin films of the different materials used in this thesis have been characterized structurally, electrically and magnetically. In particular, I focused on the characterization of C<sub>60</sub>/Py bilayers combining different techniques (AFM, XRR, SQUID, MOKE) in order to test their suitability as a base system for molecular-based spintronics. We have highlighted three general constraints that any bilayer needs to fulfill for being used in vertical spintronic devices: (1) the films need to grow smoothly; (2) the molecular layer should be minimally damaged by the top metal deposition; (3) the magnetic properties of the ferromagnetic layer need to be preserved.

We found that the C<sub>60</sub>/Py bilayers satisfy these three constraints: the layers grow with low surface roughness and the intermixing between Py and C<sub>60</sub> layers is limited to 1-2 nm, so that a 5-nm-thick C<sub>60</sub> layer can be contacted without pinholes. Finally, a Py layer as thin as 5 nm already displays good magnetic properties, even if it is grown on the rough C<sub>60</sub> surface.

We can, thus, conclude that the combination between C<sub>60</sub> and Py provides a robust platform for spintronic application. In particular, we suggest that this system is ideal to study the effect of further modifications (of the morphology and/or of the energetic) at metal-organic interfaces.

### 3.4 References

- [1] D. Smith, *Thin-Film Deposition: Principles and Practice* (1995).
- [2] C. Kittel, *Introduction to Solid State Physics* (2005).
- [3] R. C. Dynes and J. P. Garno, *Physical Review Letters* **46**, 137 (1981).
- [4] J. Bass and W. P. Pratt, *Journal of Physics: Condensed Matter* **19**, 183201 (2007).

### 3.4 References

---

- [5] P. M. T. M. van Attekum, P. H. Woerlee, G. C. Verdake, and A. A. M. Hoeben, *Physical Review B* **29**, 645 (1984).
- [6] N. Artunc and Z. Z. Ozturk, *Journal of Physics: Condensed Matter* **5**, 559 (1993).
- [7] E. V. Barnat, D. Nagakura, P. Wang, and T. Lu, *Journal of Applied Physics*, **91** 1667 (2002).
- [8] M. Ohring, *Materials Science of Thin Films (second Edition)* (2001).
- [9] K. L. Chopra, *Journal of Applied Physics* **39**, 1874 (1968).
- [10] R. Meservey and P. M. Tedrow, *Physics Reports* **238**, 173 (1994).
- [11] H. Haick and D. Cahen, *Accounts of Chemical Research* **41**, 359 (2008).
- [12] H. Haick, J. Ghabboun, and D. Cahen, *Applied Physics Letters* **86**, 042113 (2005).
- [13] B. de Boer, M. M. Frank, Y. J. Chabal, W. Jiang, E. Garfunkel, and Z. Bao, *Langmuir: the ACS Journal of Surfaces and Colloids* **20**, 1539 (2004).
- [14] B. A. C. Dürr, F. Schreiber, M. Kelsch, H. D. Carstanjen, and H. Dosch, *Advanced Materials* **961** (2002).
- [15] F. J. Jedema, H. B. Heersche, a T. Filip, J. J. a Baselmans, and B. J. van Wees, *Nature* **416**, 713 (2002).
- [16] J. Als-Nielsen, *Elements of Modern X-Ray Physics* (New York, 2001).
- [17] F. J. Jedema, a T. Filip, and B. J. van Wees, *Nature* **410**, 345 (2001).
- [18] J. S. Moodera, L. R. Kinder, T. M. Wong, and R. Meservey, *Physical Review Letters* **74**, 3273 (1995).
- [19] T. R. McGuire and I. Potter, *IEEE Transactions on Magnetics* **4**, 1018 (1975).
- [20] P. Vavassori, *Applied Physics Letters* **77**, 1605 (2000).
- [21] O. Amelines-Sarria, P. C. dos Santos Claro, P. L. Schilardi, B. Blum, a. Rubert, G. Benitez, V. a. Basiuk, a. González Orive, a. Hernández Creus, C. Díaz, and R. C. Salvarezza, *Organic Electronics* **12**, 1483 (2011).
- [22] C. R. Hansen, T. J. Sørensen, M. Glyvradal, J. Larsen, S. H. Eisenhardt, T. Bjørnholm, M. M. Nielsen, R. Feidenhans'l, and B. W. Laursen, *Nano Letters* **9**, 1052 (2009).
- [23] Z. H. Xiong, D. Wu, Z. V. Vardeny, and J. Shi, *Nature* **427** 821 (2004).
- [24] C. Barraud, P. Seneor, R. Mattana, S. Fusil, K. Bouzehouane, C. Deranlot, P. Graziosi, L. Hueso, I. Bergenti, V. Dediu, F. Petroff, and A. Fert, *Nature Physics* **6**, 615 (2010).
- [25] S. Sanvito, *Nature Physics* **6**, 526 (2010).
- [26] Y.-L. Chan, Y.-J. Hung, C.-H. Wang, Y.-C. Lin, C.-Y. Chiu, Y.-L. Lai, H.-T. Chang, C.-H. Lee, Y. J. Hsu, and D. H. Wei, *Physical Review Letters* **104**, 177204 (2010).

[27] A. A. Sidorenko, C. Pernechele, P. Lupo, M. Ghidini, M. Solzi, R. De Renzi, I. Bergenti, P. Graziosi, V. Dediu, L. Hueso, and a. T. Hindmarch, *Applied Physics Letters* **97**, 162509 (2010).

[28] I. Bergenti, a. Riminucci, E. Arisi, M. Murgia, M. Cavallini, M. Solzi, F. Casoli, and V. Dediu, *Journal of Magnetism and Magnetic Materials* **316**, e987 (2007).

[29] L. Néel, *C. R. Acad. Sci, Ser. A* **255**, 1676 (1962).

[30] M. Coey, *Magnetism and Magnetic Materials* (Cambridge, 2009).



## Chapter 4

# C<sub>60</sub> based spin valves

*In this chapter I focus on the C<sub>60</sub> based spin valves. In such devices, a C<sub>60</sub> layer is inserted between two ferromagnetic electrodes.*

*The device geometry is very simple and is described in detail in section 1. The devices are patterned by the deposition of Co/AIO<sub>x</sub>/C<sub>60</sub>/Py stacks through shadow masks. In every chip, two devices are left without covering the AIO<sub>x</sub> layer with C<sub>60</sub>, and are used as references. Section 2 focuses on the characterization of such reference devices. I explain that rather than using resistive AIO<sub>x</sub> barriers we prefer to employ leaky barriers where no tunneling magnetoresistance is measured.*

*In section 3 and 4 I present the electrical and magnetic characterization of devices with different C<sub>60</sub> thicknesses. In section 3, I show that the transport mechanism is in agreement with a multi-step tunnelling regime. In section 4, I show that a significant magnetoresistance (in excess of 5%) is measured for the different thicknesses of the C<sub>60</sub> interlayer (from 5 nm to 28 nm) up to high applied biases (~1 V), demonstrating a coherent spin transport through C<sub>60</sub> molecules.*

### 4.1 Device geometry

The prototypical spintronic device is a spin valve (SV) [1], which in its simplest form is a trilayer structure composed by a non-magnetic material sandwiched between two ferromagnetic (FM) electrodes [2]. Its electrical resistance is different when the electrode magnetizations are aligned parallel (P) or antiparallel (AP), provided that some electrons retain their spin while crossing the non-magnetic layer [3]. As explained in the introduction (chapter 1), the device can be driven from the P to the AP magnetization state by the application of an external magnetic field. The corresponding resistance

## 4.1 Device geometry

variation is called magnetoresistance (MR) [1]. In our case, Co and Py are used as FM electrodes and  $C_{60}$  as the NM interlayer.

Figure 4.1 (a) shows a sketch of the device and of the measurement scheme we employ. The SVs have a cross-bar geometry obtained by metal deposition through shadow masks on Si/SiO<sub>2</sub> (150 nm) substrates. In every chip, five 15-nm-thick Co lines are deposited as bottom electrodes. A thin Al layer (0.9 nm) is deposited on top of them and was oxidized in-situ using an oxygen-plasma. A  $C_{60}$  layer, with thickness between 5 and 28 nm, is also evaporated through a shadow mask designed in such a way that the fullerene only covers 3 of the 5 bottom lines. Hence, two Co electrodes are left only with the thin AlO<sub>x</sub> layer and are used as reference junctions. Finally, the sample is completed with the evaporation of a 20-nm-thick Py top electrode. Junction areas range from 200×200 μm<sup>2</sup> to 500×200 μm<sup>2</sup>. The electrical measurement of every device in the chip was performed with the 4-terminal-sensing scheme of figure 4.1 (a). In such a sensing scheme, the current flows between two ends of the two different electrodes, and the voltage is measured at the other ends of the same electrodes. In this way, the current flowing into the electrodes does not enter in the voltage measurement path, so that the measured voltage drops in the junction area.

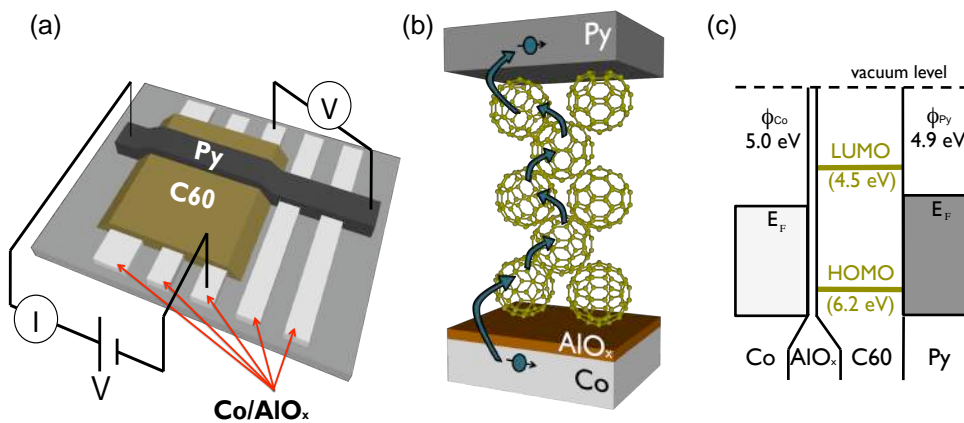


Figure 4.1. (a) Schematic of our spin valve device. Only 3 of the 5 bottom Co electrodes are covered with  $C_{60}$ , in such a way that in every chip there are 3 organic junctions and 2 reference junctions with only an AlO<sub>x</sub> layer. (b) Ideal representation of a cross-section of our  $C_{60}$ -based spin valves. (c) Rigid energy band diagram for the Co/AlO<sub>x</sub>/ $C_{60}$ /Py stack.

Even if we aim to study the spin transport in the C<sub>60</sub> interlayer, in our device we always employ an ultrathin AlO<sub>x</sub> seed layer below the C<sub>60</sub> layer (figure 4.1(a) and (b)). Several groups have previously shown that the presence of such a seed layer in molecular based SVs improves the device performances and reproducibility [4–8]. Its role is not completely clear, but it has been shown that it improves the spin polarization of the injected current. Moreover, it insulates the molecules from the Co electrode, which is very useful since Co is known for being very reactive with different organic molecules [9].

Figure 4.1 (c) shows the rigid energy band diagram of our devices. The lowest unoccupied molecular orbital (LUMO) of C<sub>60</sub> matches quite well with the Fermi energy of common ferromagnetic metals, such as Cobalt or Permalloy (Fe<sub>80</sub>Ni<sub>20</sub>, Py), making possible a relatively easy current injection from magnetic electrodes, while keeping a moderate energy injection barrier. The actual energy barrier at the Py/C<sub>60</sub> and Co/C<sub>60</sub> interfaces is different from the rigid scheme of fig. 4.1 (c), and will be discussed in detail in the next chapters. [10]

In this section, I would also like to stress that the SV geometry we employ (fig 4.1) is the simplest possible [1]. The structure of fully optimized SVs (either GMR or MTJs) differs from our simple geometry in three main aspects.

1. The AP magnetization state can be stabilized in different ways. In our case, we use the simplest method of employing two FM metals with intrinsically different coercive fields, Co and Py. This situation is not ideal because in the junction area the two FM metals become coupled, as the magnetization reversal in one layer tends to reverse the magnetization even in the second layer. Moreover, the coercive fields of Co and Py are rather close (for 15 nm thick thin films,  $H_{cPy}=2$  Oe;  $H_{cCo} = 25$  Oe – see section 3.1.2), so that the AP state would be stable at most for some tens of Oersted. As a result, it becomes rather difficult to reach a completely antiparallel state. More sophisticated SVs are based on the exchange bias effect [11]. In this case, an antiferromagnetic material (or a multilayer structure known as artificial antiferromagnet [12]) is used to keep the magnetization of one of the layer pinned, so the AP state becomes very stable [13].
2. The metals in our devices are deposited through shadow masks, so the junction area is rather big. Optimized SVs are patterned with lithography methods in micron-sized columns to increase the homogeneity all over the junction area and to reduce the probability of pinholes through the barrier [11]. Moreover, patterning the junction area in the micron range also allows the control of the coercive field of the FM layers. In fact, when the junction size is small enough, its

## 4.1 Device geometry

---

shape anisotropy begins to play an important role in the switching process [14]. Therefore it can be designed for obtaining sharper switching fields and more stable antiparallel states.

3. Our layers are polycrystalline or amorphous, we have not attempted to grow single crystals. In several cases, ultrahigh crystalline quality of materials improves the MR ratio. The SV devices mostly used in technologic application are Fe/MgO/Fe magnetic tunnel junctions [15] with atomically perfect epitaxial stacking of layer [16,17], which is by far out of our scope.

In fact, we do not expect our devices to perform as fully optimized SVs. The production of high performance SVs is not the goal of this chapter. Instead, we want to use the devices to obtain information about the spin transport in the  $C_{60}$  layer. SVs with various structures are commonly used for studying the spin transport properties into the interlayer material [18,19]. For this purpose, the simple geometry in fig. 4.1 is good enough, in the sense that MR is only measured if the spin information is not lost into the  $C_{60}$  layer. For this reason, we choose to adopt the simple geometry, which is also the only geometry compatible with our evaporator and our materials. Indeed, multilayer structures for exchange-biased SVs and for epitaxial layers are typically grown by sputtering [11,15], while the presence of a molecular layer complicates any lithography step [20].

## 4.2 $AlO_x$ magnetic tunnel junction

Prior to the  $C_{60}$  spin valves, we produced and optimized magnetic tunnel junctions (MTJs) with thin  $AlO_x$  as insulating barrier. For different reasons, these devices are the basis for the  $C_{60}$  SVs. As explained in the previous section, in every device we employ an  $AlO_x$  seed layer at the bottom of the  $C_{60}$  layer. And, we leave 2 reference junctions with only the seed layer. In this respect,  $AlO_x$  MTJs will serve as a comparison even for the MR measurements in  $C_{60}$  SVs.

$AlO_x$  based MTJs were the first to be reproducibly fabricated [21,22] and are nowadays produced routinely in several laboratories all over the world. The growth recipe is well established and relatively easy. It is based on the property of Al of forming a homogeneous self-limiting oxide barrier at the surface with a thickness in the tunneling regime (1-3 nm). An extremely thin Al layer is deposited on the bottom metal contact and is subsequently oxidized by exposure to oxygen. Ideally, all the Aluminum gets oxidized, while the bottom contact does not. This fabrication method proved to be

more reliable than a direct deposition of a thin Al<sub>2</sub>O<sub>3</sub> layer [23]. In our case, the oxidation is performed with an O<sub>2</sub> plasma, which is also a common step in the MTJ recipe. Two parameters are particularly important for determining the device performances: the Al thickness and the oxidation time.

1. The Al thickness must be very thin (1-3 nm) to allow the electron tunneling through it. Controlling the exact barrier thickness at the Å level is vital, because the tunneling probability diminishes exponentially with the tunneling barrier thickness, so that a tiny thickness variation gives rise to a big resistance change. As already mention in the section 3.1.2, the Al must be grown on an extremely flat electrode in order to avoid direct contact between the top and bottom metals.
2. The plasma oxidation should be optimized in order to oxidize the whole Al film, but not the bottom layer. If the duration of the plasma is not enough to oxidize the whole barrier, some Al metal will be left either at the interface or into the barrier, with detrimental effects on the MR [24,25]. In the opposite case, if the plasma duration is too long, the magnetic contact can get partially oxidized, and the presence of the magnetic oxide at the interface worsen the metal spin polarization, lowering again the MR.

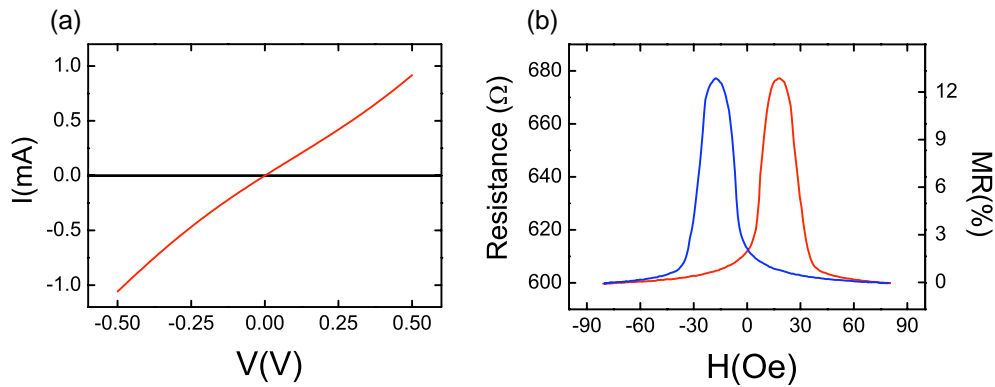


Figure 4.2. (a) Current-Voltage characteristic of one of our 'optimized' AlO<sub>x</sub> tunnel junctions, which shows a tunneling magnetoresistance in excess of 13%.

Figure 4.2 shows the characteristics of a representative optimized AlO<sub>x</sub> magnetic tunnel junction produced in our evaporator. The device stack was Co (15 nm) / Al (2.3 nm) + Oxygen plasma / Py 20 nm. The parameters for the plasma oxidation were chosen following the recipe in ref. [25]: 180s in an O<sub>2</sub> atmosphere with a pressure  $p = 10^{-1}$  mbar. The plasma power was below 10 W (approximately 10 mA for 400 V). Fig 4.2 (a) shows the current-voltage (I-V) characteristic of a typical device. At

## 4.2 AlO<sub>x</sub> magnetic tunnel junction

low bias voltages, the current increases linearly with the voltage; at higher biases the trace deviates from the linear dependence. Such a behavior is typical of tunnel junctions [26]. The low-bias resistance of our AlO<sub>x</sub> is typically in the range between  $100 \Omega < R < 1000 \Omega$  for the junction area  $A = 250 \times 250 \mu\text{m}^2$ .

The corresponding TMR was reproducibly above 10 %, reaching 15 % in the best devices (in fig 3.2 (b) I show a typical device with MR = 13.5 %). Reported TMR for optimized AlO<sub>x</sub> MTJs at room temperature are usually higher, in the range between 20 % – 30 % [14,23]. In particular, it should be noticed here that the AP state in figure 3.2 (b) has a rounded shape, without the usual clear plateau of reported MTJs (see [11,14,23,25]). We conclude that our AP state is not completely achieved, and it is rather unstable. This fact will worsen the performances of the devices described in this and in the following chapter. However, given all the limitations of our simple device geometry discussed in the previous section, the TMR above 10 % presented here can be considered satisfactory.

In previous studies on molecular tunnel junctions, a fully-optimized inorganic tunnel barrier is inserted between the bottom ferromagnetic electrode and the OS [4–8]. As a consequence, it is sometimes difficult to separate the effect of the inorganic from that of the organic barrier. In those devices, the presence of the molecules results in a deterioration of the performances of the optimized tunnel junction.

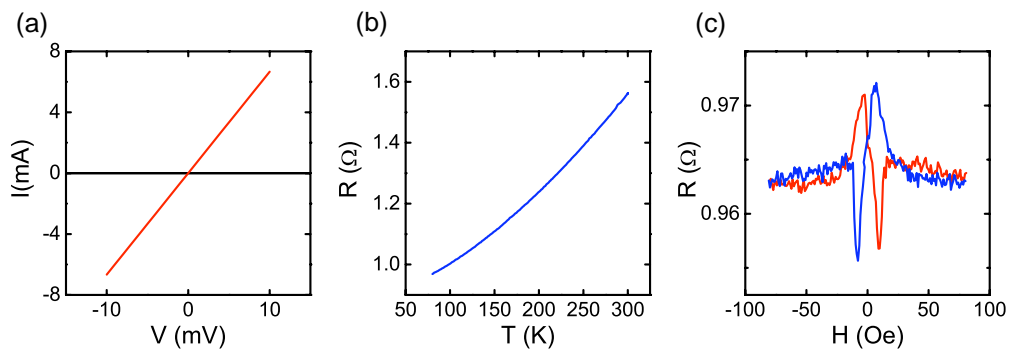


Figure 4.3. Characterization of a typical AlO<sub>x</sub> reference junction. (a) Current-Voltage characteristics show linear behavior with a resistance below  $2 \Omega$ . (b) The resistance as a function of the temperature shows a metallic behavior. (c) Resistance measured as a function of the field at 80 K.

In our case, we choose not to use our optimized 2.3-nm-thick barriers as the seed layer for the C<sub>60</sub> growth. Instead, we intentionally use a 0.9 Al layer which does not even form a continuous layer, but rather forms a leaky barrier. The reference junctions

present in every chip (see fig 4.1 (a)) always show the characteristics shown in fig. 4.3. The resistance is very low (typically around  $R = 1.5 \Omega$  (a)), suggesting that the junction is actually a short circuit. A valid *criterion* to distinguish between continuous and leaky tunnel barriers is the variation of the barrier resistance as a function of the temperature  $R(T)$  [27]. The resistance of continuous tunneling barriers increases when lowering the temperature. On the contrary, the resistance of our junctions decreases when lowering the temperature (fig 4.3 (b)), a typical behavior of metallic systems [28], confirming that they are actually leaky. Finally, figure 4.3 (c) shows the resistance of the junctions in a magnetic field sweep measured at 80 K. A small MR is actually measured, but with a very different shape compared to the typical shape of TMR signals (compare with fig. 4.2 (b)). We ascribe such an effect to the anisotropic MR (AMR) of the magnetic electrodes. Indeed, when the junction resistance is as low as in this case, the resistance of the metallic contacts in the junction area begins to be comparable to it. Therefore, even if with the 4 terminal sensing scheme of fig 4.1 (a) one only measures the voltage drop in the junction area, a sizable part comes from the magnetic contacts – this also explains the metallic behavior of the  $R(T)$  in fig. 4.3 (b). With a more resistive barrier (for instance when C<sub>60</sub> is employed – see next section), the resistance of the contacts in the junction area is negligible compared with the barrier, and AMR effects do not affect the measurement.

Before measuring the C<sub>60</sub>-based spin valves, we make sure that the reference junctions behave as in figure 4.3. In this way, we are confident that the effects measured in the C<sub>60</sub>-based devices are intrinsic of the C<sub>60</sub> layer itself, because the reference junction is a short circuit.

### 4.3 Electrical transport in C<sub>60</sub>-based spin valve

After having discussed the reference junctions, we move now to the electronic transport properties of the C<sub>60</sub>-based devices. For C<sub>60</sub> thicknesses below 10 nm, the RT current-voltage (I-V) curves are non-linear and symmetric, similar to the representative curve of fig. 4.4 (a). In this thickness range, the resistance at low voltages (10 mV) increases around 40% when lowering the temperature down to 80 K (Fig. 4.4 (c)). The I-V traces become progressively more asymmetric as the C<sub>60</sub> thickness is increased (see fig. 4.4 (b) and (c) for representative samples). Above a thickness of 20 nm, the low-bias resistance (measured at 10 mV) increases typically 400% when lowering the temperature down to 200 K, keeping an almost constant value below that temperature

### 4.3 Electrical transport in $C_{60}$ -based spin valves

(fig. 4.4 (d)). Figure 4.4 (e) shows the I-V trace of the 20-nm-thick  $C_{60}$  spin valve measured at 300 K and 78 K. At the low temperature, the resistance increases and the I-V traces become more symmetric (blue line). The temperature behaviour of the resistance does not follow in any case a simple thermally activated law. Such a temperature behaviour was found in  $C_{60}$ -based junctions with a geometry very similar to ours [29]. We will show below that this behaviour is compatible with the conductivity dominated by quantum-mechanical tunnelling from molecule to molecule.

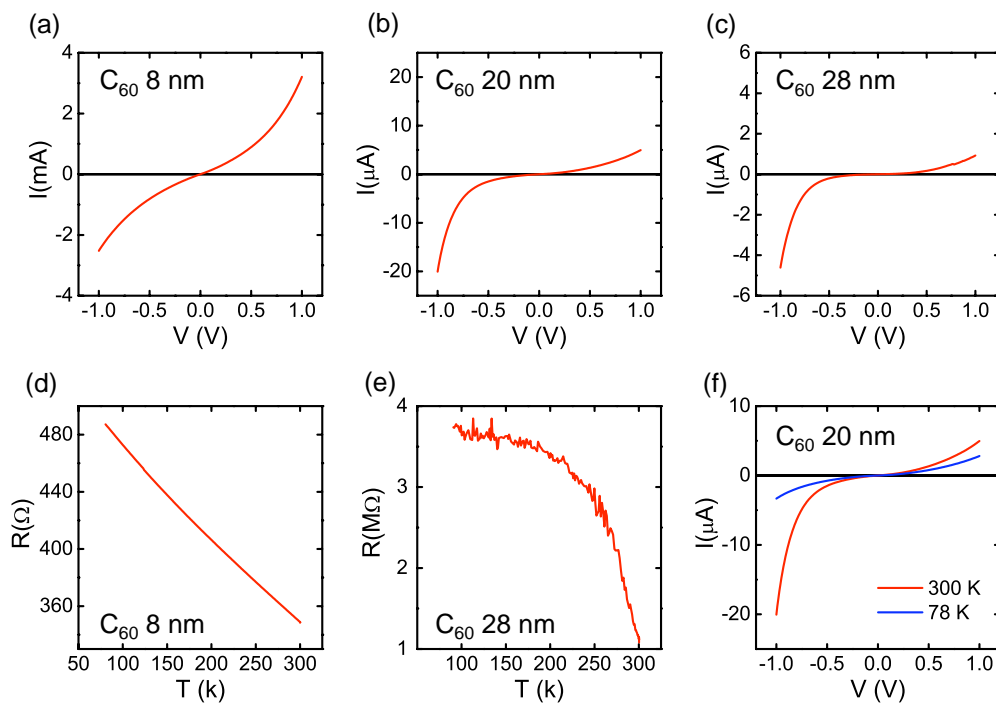


Figure 4.4. Electrical characterization of  $C_{60}$  based spin valves. (a), (b), (c) Room temperature Current-Voltage (I-V) traces for samples with 8 nm, 20 nm and 28 nm of  $C_{60}$  respectively. (c), (d) Temperature dependence of the resistance measured at 10 mV for samples with 8 and 28 nm  $C_{60}$  thicknesses. (f) I-V trace of the 20 nm sample measured at 300 K and 78 K.

Inspecting figures 4.4 (a)-(c), it is evident that the current diminishes when increasing the  $C_{60}$  layer thickness. Indeed, the resistance-area  $RA$  product of all our samples (measured at 10 mV) increases exponentially with  $C_{60}$  thickness in the range from 5 to 28 nm, spanning almost six orders of magnitude (fig. 4.5(a)). An exponential increase of the resistance with the interlayer thickness is expected in a quantum mechanical tunnelling framework. For example, the standard Simmons model for coherent

tunnelling [26] is based on the approximation that the probability ( $D$ ) for an electron to penetrate a potential barrier can be expressed as:

$$D \propto e^{-\frac{\sqrt{m\phi}}{h}d} \quad (1)$$

where  $d$  is the barrier thickness,  $\phi$  is the mean barrier height above the Fermi level of the negatively biased electrode,  $m$  is the electron mass and  $h$  is the Planck's constant. From this approximation, a formula is derived for the current density  $J$  through a tunnelling barrier of thickness  $d$  and height  $\phi$  as a function of the applied voltage  $V$ . This formula can be written as:

$$J = \frac{A}{d^2} \left[ (2\phi - V) e^{-kd\sqrt{2\phi - V}} - (2\phi + V) e^{-kd\sqrt{2\phi + V}} \right] \quad (2)$$

with constants  $A = e/(4\pi h\beta^2)$  and  $k = 4\pi\beta\sqrt{m}/h$  ( $e$  is the electron charge,  $h$  is the Planck's constant,  $m$  is the electron effective mass and  $\beta$  a constant with value around 1).

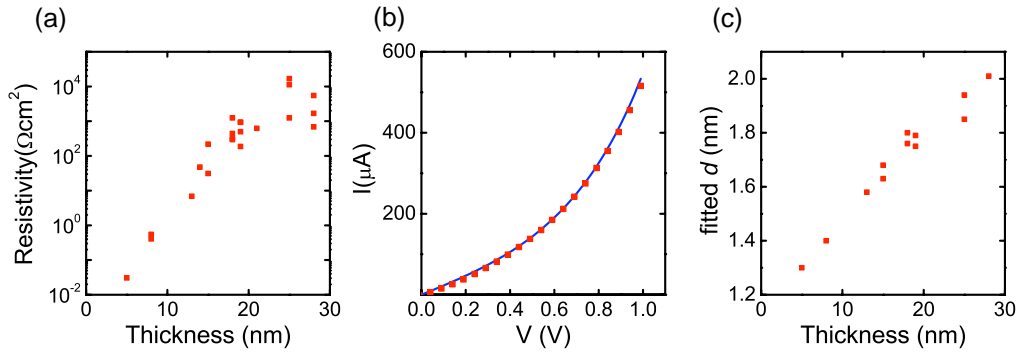


Figure 4.5. (a) Room temperature low-bias resistance vs thickness of C<sub>60</sub> layer. (b) Room temperature I-V trace of a device with a 13-nm-thick C<sub>60</sub> layer: experimental points (red dots) and fitting to the Simmons formula (blue line). (c) Tunnel barrier thicknesses obtained by fitting the room temperature I-V traces with the Simmons equation (see equation 2) as a function of the nominal C<sub>60</sub> thicknesses.

We fitted 14 individual room temperature I-V traces corresponding to different C<sub>60</sub> thicknesses using equation (2). We fitted only the positive side of the I-V traces in fig. 4.4 (a)-(c), corresponding to electrons injected into the C<sub>60</sub> layer from the Co electrode

### 4.3 Electrical transport in C<sub>60</sub>-based spin valves

---

through the AlO<sub>x</sub> seed layer. From each fit we can extract both  $\phi$  and  $d$  of the tunnel barrier. A typical fit of the experimental data is shown in fig. 4.5 (b) for a device with a 13-nm-thick C<sub>60</sub>. The barrier height  $\phi$  is fairly constant for all thicknesses, with a value averaged over the 14 I-V traces of  $2.4 \pm 0.36$  eV. The effective thickness  $d$  is always much smaller than the nominal C<sub>60</sub> thickness, but there is a linear relation between these quantities (fig. 4.5 (c)). For the interpretation of this linear dependence, we follow a simple multistep tunnelling model [30]. In this model the electrons are injected from the metal through an interface barrier into the first molecular layer, and then they undergo a number of tunnelling steps from molecule to molecule until they reach the second electrode. Hence, the probability of an electron crossing the whole molecular layer will be the product of the probabilities of each tunnelling event:

$$D \propto t_i \times \prod_n t_n \quad (3)$$

where  $t_i$  is the transmission coefficient of the interface between the metal and the organic material and accounts for both the presence of “leaky” AlO<sub>x</sub> layer and for the mismatch between the LUMO and the Fermi energy of the electrode.  $n$  is the number of molecules that an electron encounters in its path from the first to the second electrode, whereas  $t_n$  represents the transmission coefficient of each tunnelling process between adjacent molecules.  $D$  can be expressed following Eq. (1), so that:

$$D \propto e^{-a_i} \times \prod_n e^{-a_n} = e^{-(a_i + na_n)} \quad (4)$$

where  $a_n$  is the effective intermolecular distance and  $a_i$  is the thickness of the interfacial barrier. This model allows us to separate the contribution to the resistance of the interface from that of the molecular layer. By comparing equations (1) and (3), we can deduct that in this model the relevant tunnelling thickness is not the whole C<sub>60</sub> thickness, but rather the effective thickness  $d = a_i + na_n$ , i.e. the sum of an interfacial contribution plus each intermolecular distance multiplied by the number  $n$  of molecules in the electron path.  $n$  can be estimated as  $n = 2x / c$ , where  $x$  is the actual C<sub>60</sub> thickness, and  $c = 14.17$  Å is the lattice parameter of the C<sub>60</sub> face-centered cubic (fcc) crystal structure [31]. The factor 2 accounts for the fact that electrons encounter two molecules in every single fcc cell (Fig. 4.1(b)). Since  $n$  increases linearly with the layer thickness  $x$ , also  $d$  should scale linearly with the actual C<sub>60</sub> layer thickness, in good agreement with our finding obtained by fitting the I-V traces to the Simmons equation (fig. 4.5(c)). In this same panel 4.5(c), the interception at zero C<sub>60</sub> thickness is 1.15 nm,

which represents the thickness of the interfacial barrier  $a_i$ . The value of the effective intermolecular distance  $a_n$  can be simply obtained as  $a_n = (d - a_i) / n = 0.2 \text{ \AA}$ . This very small effective intermolecular distance can be explained considering that at RT the tunnel electron might access empty states, which have energy higher than LUMO and a different charge density distribution in the molecule. At a certain empty state, the charge density may be located very close to its neighbor molecule.

A similar thickness dependence of the resistance was observed in early stages of the research on fullerene samples, although a simpler explanation was provided then [32]. Here, our simple model is capable of explaining also the observed temperature dependence of the resistance (see above). Tunnelling processes present only a weak temperature dependence, deviating from a thermally activated behaviour which is observed in organic bulk-dominated samples.

We should highlight that each tunnelling process is inherently spin-conserving; hence, our interpretation of the electronic transport between molecules, together with the very small intramolecular spin relaxation mechanisms, suggests that coherent spin transport over relatively long distances should be observed in our C<sub>60</sub>-based spin valves.

## 4.4 Magnetoresistance in C<sub>60</sub>-based spin valves

After the discussion of the electrical properties of C<sub>60</sub>-based devices, we move to their magnetic characterization. MR signals are recorded at RT for every C<sub>60</sub> thickness sampled (up to 28 nm). This constitutes a very relevant point, since a substantial MR (>1%) at RT has been typically ascribed only to organic tunnel junctions with ultra-thin molecular layers. On the contrary, for molecular layers with a thickness above the tunnelling limit (say  $t > 15 \text{ nm}$ ), MR has only been reported at low temperatures and often in combination with ferromagnetic manganites with an extremely high spin polarization [4–8,33–38].

Figure 4.6 shows different MR traces measured at room temperature for different C<sub>60</sub> thicknesses  $t_{C60}$ . In fig. 4.6 (a), we show MR for  $t = 8 \text{ nm}$ ; in this case the MR shape is clearly very similar to that of the AlO<sub>x</sub> tunnel junction of fig. 4.2 (b), with an AP state not fully achieved. This MR shape is representative for the samples with  $t_{C60} < 15 \text{ nm}$ . Most probably, in this thickness range the ferromagnetic metals are still coupled, and the problems discussed in section 4.1 apply.

#### 4.4 Magnetoresistance in $C_{60}$ based spin valves

For thicknesses  $t_{C_{60}} > 15$  nm, other features appear in the MR traces. At low magnetic fields we always observe steps in the resistance that roughly correspond to the coercive fields of Py and Co. In this thickness regime, the AP resistance state is more flat, which means, more stable. Indeed, the magnetic electrodes are further away from each other, so their coupling is less strong.

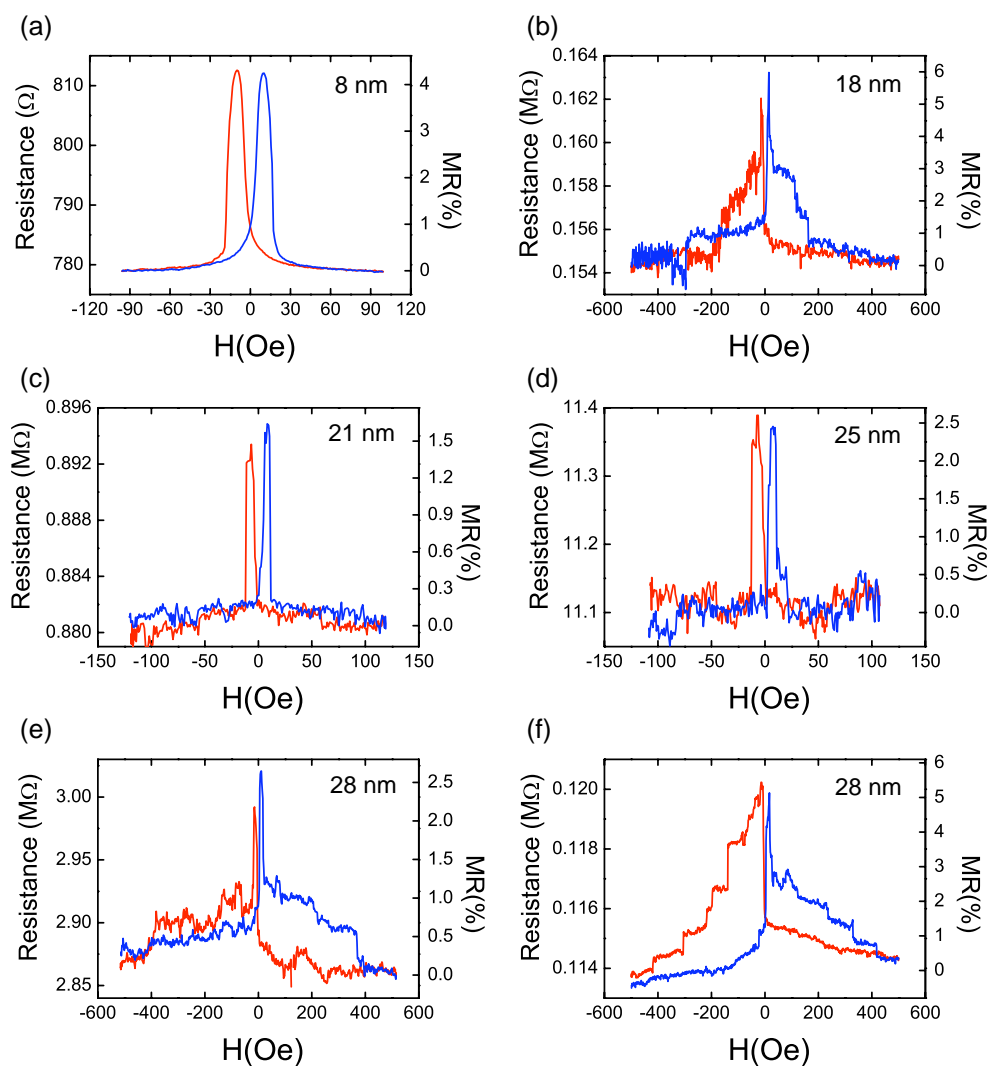


Figure 4.6. Magnetoresistance measured with a bias voltage  $V = 10$  mV for  $C_{60}$ -based spin valves with different  $C_{60}$  thicknesses: (a) 8 nm, (b) 18 nm, (c) 21 nm, (d) 25 nm, (e) and (f) 28 nm.

When higher magnetic fields are applied, several other steps are always observed in the transition from the AP to the P state (fig. 4.6 (b)-(f)). These steps do not correspond to the coercive fields of neither Py nor Co thin films (see section 3.1.2). Most probably, the magnetization reversal of the top Py contact differs from that of the Py thin film deposited on the flat SiO<sub>2</sub> substrate, because of the roughness of the low-lying C<sub>60</sub>. In fact, the C<sub>60</sub> surface roughness can cause the presence of sites in which the magnetization is locally kept pinned. These pinning sites alter the intrinsic coercive field of the magnetic layers, giving rise to a pseudo-stochastic behaviour in the MR [39,40].

In any case, and irrespective of the micromagnetic details of the magnetization reversal process in the electrodes, significant MR is measured at RT in every sample up to a C<sub>60</sub> thickness  $t_{C60} = 28$  nm. MR varies in the range between 1 % - 6 % in samples with different thicknesses, without following a clear trend (fig 4.6 (a)-(f)). Even in devices with the same C<sub>60</sub> thickness in the same chip and grown in the same run, MR varies in the different devices (e)-(f).

Following the discussion of section 4.1, we can conclude that MR can be taken as a demonstration that the current spin polarization is maintained in the C<sub>60</sub> layer in every tested device. These results compare very positively with the data available in the literature in two main aspects: on one hand, MR is usually negligible at room temperature in samples whose electrodes are highly spin-polarized magnetic oxides (such as manganites). On the other hand, we report RT MR values for thicknesses at least one order of magnitude higher than for samples composed of 3d-ferromagnetic metals and of prototypical spin transport organic semiconductors as Alq<sub>3</sub>. We believe that the improved device performance is intrinsically related to the superior spin transport properties of the C<sub>60</sub> molecular interlayer.

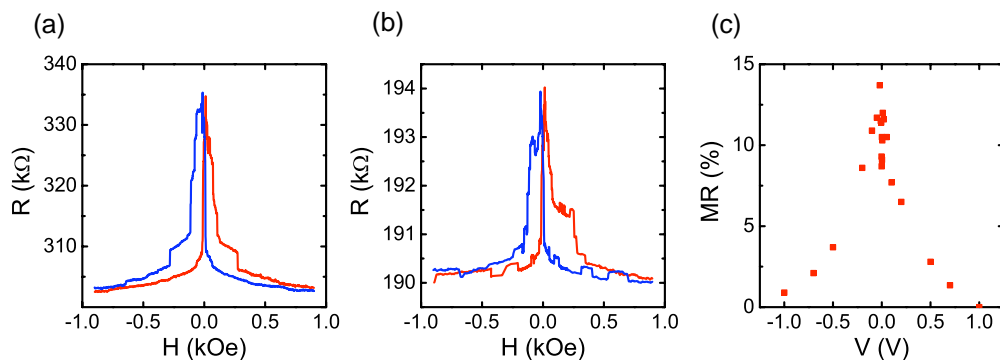


Figure 4.7. (a) and (b) MR measured for the sample with 18 nm of C<sub>60</sub> at 80 K with bias  $V = 10$  mV and  $V = -700$  mV, respectively.

MR is found to increase in all the devices tested at low temperature. Fig 4.7 (a) and fig 4.6 (b) show MR for the same 18-nm- $C_{60}$  device, measured at 300 K and at 80 K. For this device, MR is below 6 % at 300 K and above 13 % at 80 K. A similar increase in MR was measured for several other devices. Fig. 4.6 (b) shows the MR measured for the same sample at 80 K with a rather high bias voltage,  $V = -700$  mV. Though smaller, the effect is still clearly visible. Fig 4.7 (c) shows that MR is maximum at low bias voltages, and it is still measurable at a bias of  $V = -1$  V. Such a voltage dependence for MR is as relevant as the room temperature MR values for thick  $C_{60}$  samples. Indeed, in several molecular based tunnel junctions, MR effects are only measured at low bias voltages ( $V < 100$  mV) [37]. The slow decay of the MR with applied bias is important since the overall output current increases simultaneously with the bias, and relatively large current values are needed for possible applications in spin devices.

## 4.5 Conclusions

The large values (>5%) of RT MR in relatively thick (>25 nm) fullerene- based spin valves demonstrate spin coherent transport in fullerenes at room temperature. To interpret our experimental results we present a multi-step tunnelling model capable of explaining both electronic and spin coherent transport in our samples. The spin transport is robust, as MR is measured even at high bias voltages. We believe that both the large MR values and the small decrease of this MR with applied bias are related to the robust intrinsic properties of fullerenes for spin transport.

## 4.6 References

- [1] I. Zutic, J. Fabian, and S. D. Sarma, *Reviews of Modern Physics* **76**, (2004).
- [2] B. Dieny, V. S. Speriosu, S. S. P. Parkin, B. A. Gurney, D. R. Wilhoit, and D. Mauri, *Physical Review B* **43**, 1297 (1991).
- [3] T. Valet and A. Fert, *Physical Review B* **48**, 7099 (1993).
- [4] T. Santos, J. Lee, P. Migdal, I. Lekshmi, B. Satpati, and J. Moodera, *Physical Review Letters* **98**, 016601 (2007).

- [5] J. Shim, K. Raman, Y. Park, T. Santos, G. Miao, B. Satpati, and J. Moodera, *Physical Review Letters* **100**, 226603 (2008).
- [6] J. Schoonus, P. Lumens, W. Wagemans, J. Kohlhepp, P. Bobbert, H. Swagten, and B. Koopmans, *Physical Review Letters* **103**, 146601 (2009).
- [7] G. Szulczewski, H. Tokuc, K. Oguz, and J. M. D. Coey, *Applied Physics Letters* **95**, 202506 (2009).
- [8] R. Lin, F. Wang, J. Rybicki, M. Wohlgenannt, and K. A. Hutchinson, *Physical Review B* **81**, 195214 (2010).
- [9] Y. Zhan, E. Holmström, R. Lizárraga, O. Eriksson, X. Liu, F. Li, E. Carlegrim, S. Stafström, and M. Fahlman, *Advanced Materials* **22**, 1626 (2010).
- [10] S. Braun, W. R. Salaneck, and M. Fahlman, *Advanced Materials* **21**, 1450 (2009).
- [11] S. S. P. Parkin, K. P. Roche, M. G. Samant, P. M. Rice, R. B. Beyers, R. E. Scheuerlein, E. J. O'Sullivan, S. L. Brown, J. Bucchigano, D. W. Abraham, Y. Lu, M. Rooks, P. L. Trouilloud, R. a. Wanner, and W. J. Gallagher, *Journal of Applied Physics* **85**, 5828 (1999).
- [12] C. Tiusan, M. Hehn, K. Ounadjela, Y. Henry, J. Hommet, C. Meny, H. V. D. Berg, L. Baer, and R. Kinder, **85**, 15 (1999).
- [13] S. Gider, B.-U. Runge, A. C. Marley, and S. S. P. Parkin, *Science* **281**, 797 (1998).
- [14] W. J. Gallagher, S. S. P. Parkin, Y. Lu, X. P. Bian, A. Marley, K. P. Roche, R. A. Altman, S. A. Rishton, C. Jahnes, T. M. Shaw, and G. Xiao, *Journal of Applied Physics* 3741 (1997).
- [15] S. Yuasa and D. D. Djayaprawira, *Journal of Physics D: Applied Physics* **40**, R337 (2007).
- [16] S. Yuasa, T. Nagahama, A. Fukushima, Y. Suzuki, and K. Ando, *Nature Materials* **3**, 868 (2004).
- [17] S. S. P. Parkin, C. Kaiser, A. Panchula, P. M. Rice, B. Hughes, M. Samant, and S.-H. Yang, *Nature Materials* **3**, 862 (2004).
- [18] F. J. Jedema, a T. Filip, and B. J. van Wees, *Nature* **410**, 345 (2001).
- [19] N. Tombros, C. Jozsa, M. Popinciuc, H. T. Jonkman, and B. J. van Wees, *Nature* **448**, 571 (2007).
- [20] C. Reese, M. Roberts, M. Ling, and Z. Bao, *Materials Today* **7**, 20 (2004).
- [21] J. S. Moodera, L. R. Kinder, T. M. Wong, and R. Meservey, *Physical Review Letters* **74**, 3273 (1995).
- [22] T. Miyazaki and N. Tezuka, *Journal of Magnetism and Magnetic Materials* **139**, L231 (1995).
- [23] P. LeClair, *Fundamental Aspects of Spin Polarized Tunneling*, PhD Thesis, Technische Universiteit Eindhoven, 2002.

## 4.6 References

---

- [24] J. S. Moodera, E. F. Gallagher, K. Robinson, and J. Nowak, *Applied Physics Letters* **70**, 3050 (1997).
- [25] P. LeClair, H. J. M. Swagten, J. T. Kohlhepp, R. J. M. V. D. Veerdonk, and W. J. M. D. Jonge, *Physical Review Letters* **84** 2933 (2000).
- [26] J. G. Simmons, *Journal of Applied Physics* **34**, 1793 (1963).
- [27] J. J. Akerman, R. Escudero, C. Leighton, S. Kim, D. A. Rabson, R. Whig, J. M. Slaughter, and I. K. Schuller, *Journal of Magnetism and Magnetic Materials* **34**, 86 (2002).
- [28] C. Kittel, *Introduction to Solid State Physics* (2005).
- [29] T. L. A. Tran, T. Q. Le, J. G. M. Sanderink, W. G. van der Wiel, and M. P. de Jong, *Advanced Functional Materials* **22**, 1180 (2012).
- [30] C. Colesniuc, R. Biswas, S. Hevia, A. Balatsky, and I. Schuller, *Physical Review B* **83**, 1 (2011).
- [31] S. Saito and A. Oshiyama, *Physical Review Letters* **66**, 2637 (1991).
- [32] A. Hamed, y. y. Sun, Y. K. Tao, R. L. Meng, and P. H. Hor, *Physical Review. B, Condensed Matter* **47**, 10873 (1993).
- [33] V. A. Dediu, L. E. Hueso, I. Bergenti, and C. Taliani, *Nature Materials* **8**, 707 (2009).
- [34] Z. H. Xiong, D. Wu, Z. V. Vardeny, and J. Shi, *Nature*, **427** 821 (2004).
- [35] L. E. Hueso, I. Bergenti, a. Riminucci, Y. Q. Zhan, and V. Dediu, *Advanced Materials* **19**, 2639 (2007).
- [36] F. Wang and Z. V. Vardeny, *Synthetic Metals* **160**, 210 (2010).
- [37] C. Barraud, P. Seneor, R. Mattana, S. Fusil, K. Bouzehouane, C. Deranlot, P. Graziosi, L. Hueso, I. Bergenti, V. Dediu, F. Petroff, and A. Fert, *Nature Physics* **6**, 615 (2010).
- [38] J.-W. Yoo, H. W. Jang, V. N. Prigodin, C. Kao, C. B. Eom, and a. J. Epstein, *Physical Review B* **80**, 1 (2009).
- [39] S. Majumdar, R. Laiho, P. Laukkanen, I. J. Vaayrynen, H. S. Majumdar, and R. Osterbacka, *Applied Physics Letters* **89**, 122114 (2006).
- [40] Y.-L. Chan, Y.-J. Hung, C.-H. Wang, Y.-C. Lin, C.-Y. Chiu, Y.-L. Lai, H.-T. Chang, C.-H. Lee, Y. J. Hsu, and D. H. Wei, *Physical Review Letters* **104**, 1 (2010).

## Chapter 5

# C<sub>60</sub>-based magnetic tunnel transistors

*In this chapter I focus on the C<sub>60</sub> based magnetic tunnel transistors (MTT). In such devices, a thick C<sub>60</sub> layer is used as the semiconducting collector of a metal base transistor with a metallic spin valve base.*

*In section 1, I describe in details the operation of MTTs and the multilayer structure of our devices. The electrical and magnetic characterizations of our devices are presented in section 2. First, I explain how the device allows an accurate measurement of the energy level alignment at the metal/C<sub>60</sub> interface. Afterwards, I show that a huge (up to 89%) change in the collector current is measured at room temperature in a magnetic field sweep. Moreover, this variation can be enhanced by the application of a proper voltage at the collector, reaching in principle an infinite value due to a negligible current in the off-state.*

*In section 4, I describe how different parameters affect the performances of the device. In particular, I focus on the effects of temperature, base pressure before evaporation, bias voltage and external illumination.*

## 5.1 Device operation and structure

Magnetic Tunnel Transistors (MTT) are 3-terminal devices with the same scheme of a metal base transistor, in which a hot-electron current is injected into the device by an emitter, and a metal base modulates the amount of current reaching the semiconducting collector [1] (fig. 5.1(a)). The electrons in the metal base are *hot* in the sense that they possess an energy that is higher than the metal Fermi energy.

In metal base transistors, a possible way to inject hot electrons into the metal base is to employ a metal emitter separated from the metal base by a tunnel junction (TJ). In this way, the voltage applied at the tunnel junction terminals determines the energy of

## 5.1 Device operation and structure

the electrons entering into the metal base (figure 5.1 (a)). This emitter geometry has the advantage of allowing the injection of hot electrons with any energy. A semiconductor could also be used as hot electron emitter; but in that case the energy of the hot electrons would be fixed, determined by the energy barrier at the semiconductor/metal interface [1,2].

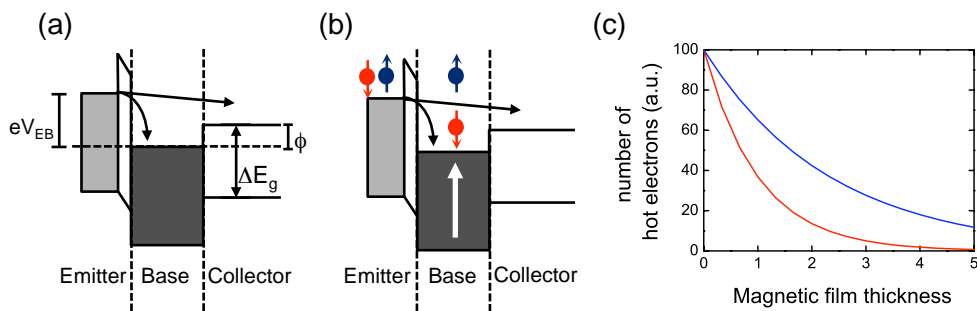


Figure 5.1. (a) Energy level alignment in a metal base transistor. A metal emitter injects hot electrons into the metal base through a tunnel barrier, and a semiconducting collector is used to collect those electrons that have energy above the Schottky barrier. (b) When the base is a ferromagnetic metal, ideally all the minority electrons are attenuated in the base, so that the only electrons entering the collector are majority electrons. (c) The energy attenuation of hot electrons in ferromagnetic metals is spin polarized (adapted from reference [2]).

Inside the metal base, the hot electrons undergo scattering events that lower their energy [2]. A semiconductor terminal is placed at the other side of the base, and it is used to collect those electrons that have retained their energy while crossing the metal. Indeed, at the metal/semiconductor interface an energy barrier  $\phi$  forms, so that only electrons with energy above it can enter the semiconductor, i.e. those electrons that are still hot (fig. 5.1 (a)). The hot electron energy decays exponentially in the metals, with typical length scale in the nanometer range [3]. Therefore, the thickness of the base must be in that same range, otherwise no electron would retain enough energy to enter into the collector. Due to this requirement, metal-base-transistor structures are typically vertical. In this way, hot electrons travel through the base across its thickness, which can be kept in the few nanometer range without technological problems.

The MTT is based on the fact that when a ferromagnetic (FM) metal is used in the base, it acts as a spin filter (figure 5.2 (b)). Indeed, the scattering events that cause the energy attenuation of the hot electrons are spin-dependent in FM metals. In fact, the inelastic mean free path is longer for majority electrons [4]. This is schematically shown in figure 5.1 (c). The spin asymmetry in the hot-electron attenuation lengths leads to the

dominant transmission of majority spins in FM layers. After travelling a few nanometers (< 5 nm) in the FM base, most hot electrons lose their energy, but those electrons that retain it exhibit an extremely high spin polarization, which can exceed 90% for FM layers thicker than 3 nm [5]. In this case, the energy barrier at the FM metal/semiconductor interface collects only the spin filtered electrons.

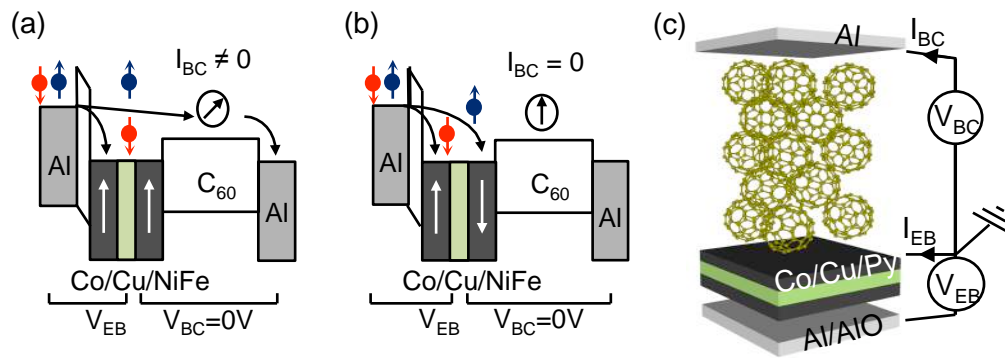


Figure 5.2. Energy diagram of the MTT when the spin valve is in the parallel state (a) and in the antiparallel state (b). Assuming a perfect spin filtering effect, the current enters the C<sub>60</sub> collector only when the spin valve is in the parallel state (see text). (c) Scheme of the device. The 3 terminals are highlighted and the voltage names are defined.

In MTTs<sup>1</sup>, the base is composed by an all-metallic spin valve (fig. 5.2) [6]. When the spin-valve base is in parallel (P) state, a fraction of the majority electrons can travel through both layers without losing its energy, getting collected as electrical current at the semiconducting terminal (Figure 5.2 (a)). When the spin-valve base is in antiparallel (AP) state, electrons are filtered in either one or the other FM layer, leaving ideally a negligible current in the collector (figure 5.2(b)). Under these conditions, the current change in the collector due to the magnetic state of the spin valve (SV) is called magnetocurrent (MC), and is defined as

$$MC(\%) = 100 \times \frac{I_p - I_{ap}}{I_{ap}} \quad (1)$$

Assuming a perfect spin filtering, MC should approach infinite, because  $I_{ap}$  should approach 0 (figure 5.2(b)).

<sup>1</sup> This kind of devices are usually called 'spin valve transistors' when the emitter is a semiconductor, and 'magnetic tunnel transistor' when the emitter is a metal/tunnel junction bilayer, as in this case. [2]

## 5.1 Device operation and structure

---

A cartoon of our device is shown in figure 5.2 (c). In every chip, six devices are patterned by deposition through shadow masks on  $10 \times 10 \text{ mm}^2$   $\text{SiO}_2$  (150 nm)/Si substrates. The emitter is composed by a 10-nm-thick Al layer, which is plasma-oxidized to form an insulating  $\text{AlO}_x$  barrier at the interface with the metal base. The base is a metallic SV, composed by a  $\text{Co}$ (4 nm)/ $\text{Cu}$ (4 nm)/ $\text{Ni}_{80}\text{Fe}_{20}$ (4 nm) trilayer grown on top of the Al/ $\text{AlO}_x$  emitter. As in conventional metallic SVs, the electrical resistance of the trilayer changes a few percent (in our devices typically  $<2\%$ ) depending on the relative alignment of the magnetization of the two FM layers (see the introduction). The voltage  $V_{\text{EB}}$  applied at the TJ terminals defines the energy of electrons injected into the SV (fig. 5.1(a)). In the following, the measurements are performed with the SV base grounded, so that  $V_{\text{EB}} < 0\text{V}$  corresponds to electrons injected by the Al emitter into the base. The current flowing between the emitter and the base will be named  $I_{\text{EB}}$ . The collector is a 200-nm-thick  $\text{C}_{60}$  layer with a 20-nm-thick Al top electrode for the actual electric contact placed above. Between the SV base and the top electrode, the bias voltage  $V_{\text{BC}}$  can be applied. As a convention for the polarities, in this thesis the base is grounded (fig. 5.2 c), so when  $V_{\text{BC}} < 0\text{V}$  electrons are injected into the  $\text{C}_{60}$  layer by the top Al electrode. The current flowing in the  $\text{C}_{60}$  collector is called  $I_{\text{BC}}$  (see figure 5.2(c)).

Before this work, only MTTs based on conventional bulk inorganic semiconductors such as Si or GaAs had been experimentally demonstrated [3,5–11]. We were the first group to produce MTTs employing the molecular  $\text{C}_{60}$  layer as semiconducting collector, taking advantage of the properties that make it ideal for metal-base transistors [12–14]. I would like to stress the importance of this difference. While all the effects happening at the interface between metals and inorganic semiconductors are well established [1], the metal/molecules interfaces are by far less controlled. Indeed, metal/inorganic semiconductor interface have been subject of intense study in the last 50 years. Such metal/inorganic interfaces with ultrahigh quality are regularly produced in semiconductor industry. This high quality was thought to be fundamental for the hot electrons filtering at the base of the operations of MTTs [2].

On the contrary, metal/molecule interfaces are typically rough and disordered. In this context, a variety of situations can take place, depending on the interaction between the specific molecular species and the metal. At the molecule/metal interface several effects have been reported [15], such as the formation of dipoles [16], the variation of the metal work functions [17], or the energy shift and broadening of molecular levels [17]. These effects depend on the details of the specific metal and molecular species in use, and are a priori difficult to predict [15]. In principle, it is not even straightforward that the energy barrier at the molecule/metal interface would act as a filter for hot electrons. Therefore, the molecular based MTT does not only represent an interesting spintronic device, but can also be used as a tool for characterizing metal/molecules interfaces from

a fundamental point of view, as will be shown in more detail in the next section and in the next chapter.

## 5.2 Device Characterization

### 5.2.1 Electrical characterization

The current-voltage (I-V) characteristics of our devices are shown in figure 5.3. Figure 5.3 (a) shows the emitter-base current  $I_{EB}$  flowing through the TJ when the voltage  $V_{EB}$  is swept between the emitter and the spin-valve base. This non-linear I-V trace is typical of TJs (see chapter 4). We found that the I-V traces of TJs grown in different devices were well reproducible and similar to the representative curve in figure 5.3 (a). In (b) we show the current  $I_{BC}$  flowing across the C<sub>60</sub> layer when the voltage  $V_{BC}$  is applied directly between the base and the C<sub>60</sub> top terminal. In the case of the device shown in (b), the 200-nm-thick C<sub>60</sub> layer is highly resistive ( $R > 20M\Omega$  at low bias voltage) and the I-V trace is again highly non-linear. A common feature in all the devices produced is an asymmetry in the I-V trace; figure 5.3 (b) shows that the current is higher in the region of negative biases, which corresponds to the Al top contact injecting electrons into the C<sub>60</sub> layer. This fact suggests that the barrier for electron injection is lower for Al than for Py; indeed, Al is known to inject efficiently electrons into C<sub>60</sub> [18]. However, in the case of C<sub>60</sub>, the I-V traces were not as reproducible as for the TJ case. Variation up to two orders of magnitude in the current flowing into the device were found in devices grown in different runs. In the next section I will comment on the origin of this lack of reproducibility and its effect on the device performances.

Finally, figure 5.3 (c) shows the base-collector current  $I_{BC}$  when the voltage  $V_{EB}$  is swept at the emitter-base terminals (with zero set voltage across the C<sub>60</sub>,  $V_{BC}=0$ ). The I-V trace is highly asymmetric and in particular, higher current flows when the emitter is negatively biased – i.e., it is injecting electrons and not holes. This is in good agreement with the well-accepted n-type nature of C<sub>60</sub>, meaning that the majority carriers are electrons. [19] Furthermore, the attenuation length of hot holes in FM layers is from 2 to 5 times shorter than the electron attenuation length [9].

## 5.2 Device characterization

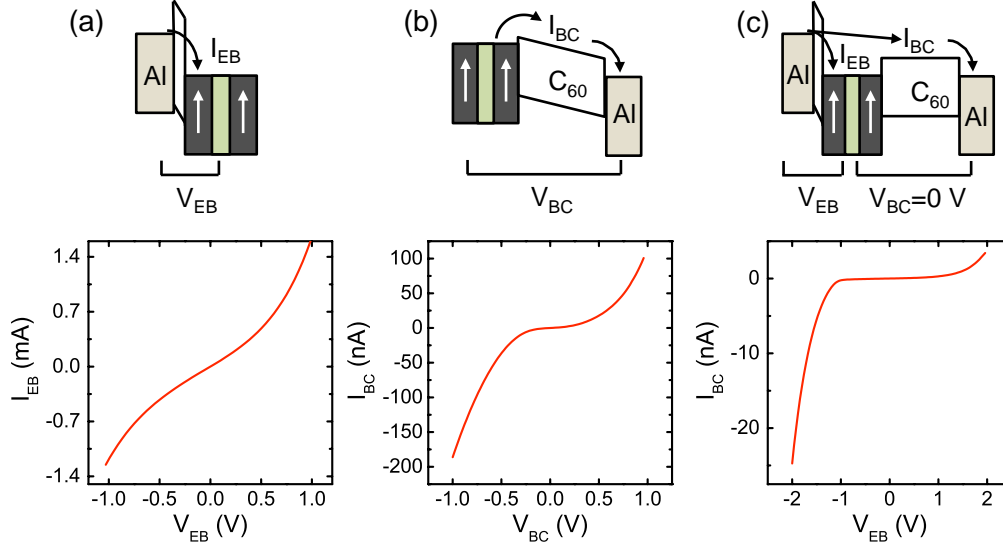


Figure 5.3. I-V traces measured across the tunnel junction (a) and the C<sub>60</sub> layer (b). (c) Hot-electron current  $I_{BC}$  measured at the collector terminal when the emitter-base voltage  $V_{EB}$  is swept and the base-collector voltage  $V_{BC}$  is kept at 0V. The energy diagrams at the top illustrate how the voltages are applied at the different terminals.

In the region of negative bias voltages  $V_{BC} < 0V$ ,  $I_{BC}$  is due to those hot electrons that have retained enough energy to overcome the barrier at the metal/C<sub>60</sub> interface. When  $V_{EB}$  is close to 0, the hot electrons have an energy below the Py/C<sub>60</sub> Schottky barrier, so they are reflected at the interface and leave a vanishing small current  $I_{BC}$  into the C<sub>60</sub> collector. For more negative  $V_{EB}$ , electrons are permitted to flow into the C<sub>60</sub> as soon as they acquire an energy above the Schottky barrier. Consequently, the threshold voltage at which  $I_{BC}$  rises represents the height of the Schottky barrier at the Py/C<sub>60</sub> interface. In the device in figure 5.3 (c), we estimate the NiFe/C<sub>60</sub> energy barrier to be around 1.0 eV. Comparing the hot electron current  $I_{BC}$  and the emitter current  $I_{EB}$ , we find that the current intensity decreases almost 6 orders of magnitude while crossing the base electrode. Indeed, not only the minority spin electrons are attenuated in the SV, but also the majority electrons. In this sense, the picture in figure 5.2 (a) is not accurate: almost all the electrons lose their energy in the base, both minority and majority [2]. The point is that the few electrons that retain their energy are preferentially majority spin.

In the region of positive bias voltages  $V_{BC} > 0V$ , the current flowing has no hot-electron origin. Its origin is schematically visualized in figure 5.4. An undesired voltage drop develops across the C<sub>60</sub> when a bias voltage is applied to the Al emitter, and the

SV base and the top Al electrode are grounded, as in figure 5.3 (c). In the emitter-base TJ a high current is flowing (in the mA range), which causes a non-negligible voltage drop  $V_L$  inside the metal base. For geometrical reasons, the same  $V_L$  drops across the  $C_{60}$  layer (see figure 5.4). In turn,  $V_L$  drives a leakage current  $I_L$  across the  $C_{60}$ , which has no hot origin and stands as a background in the measurements.  $V_L$  has the same order of magnitude in every device, because it is determined by the current  $I_{EB}$  in the TJ and by the resistance of the SV base, which are similar in different devices. On the contrary, the magnitude of  $I_L$  depends on the resistance of the  $C_{60}$  layer; with equal  $V_L$ , lower current corresponds to higher resistance. Finally, I want to point out that  $V_L$  acts as an internal  $V_{BC}$ . Its polarity is opposite to  $V_{EB}$ , meaning that when  $V_{EB} > 0V$ ,  $V_L$  acts as an effective  $V_{BC} < 0V$ .

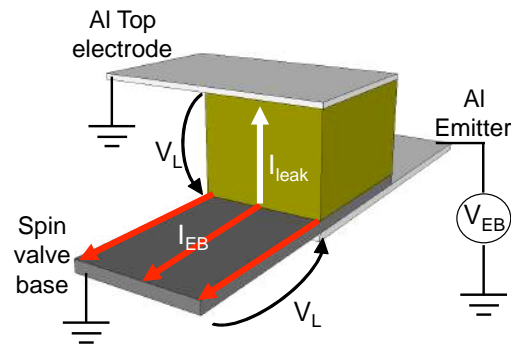


Figure 5.4. The leakage current  $I_L$  is due to the voltage  $V_L$  introduced by the high current  $I_{EB}$  flowing into the metal base.

## 5.2.2 Magnetic Characterization

We analyze the case in which a bias voltage is applied at the emitter-base terminals, with the collector kept at the same potential of the base. This situation is shown in figure 5.5 (b). In a magnetic field sweep it is possible to measure at the same time the emitter-base current  $I_{EB}$  and the base collector current  $I_{BC}$ .

$I_{EB}$  shows the typical magnetoresistive behavior (figure 5.5 (a)), due to the change in the resistance of the spin-valve contact. However, the variation in  $I_{EB}$  is small, below  $MC_{EB} < 0.3\%$ , because the resistance change of the SV itself is around  $2\%$ , and it is measured in series with the more resistive and non-magnetic-field-dependent TJ, where most of the voltage drops.

The variation of  $I_{BC}$  measured at the same time is more than two orders of magnitude higher, with  $MC_{BC}$  values up to  $89\%$  (figure 5.5 (c)) at room temperature. As

## 5.2 Device characterization

pointed out above, a naive analysis would expect the current in the AP state to be exactly zero (figure 5.2 (b)), but this ideal case can hardly be realized in actual devices due to the leakage current mentioned in the previous section. Further, in our particular case, the rounded shape of the MC trace suggests that again the AP state is not fully reached, as discussed in the previous chapter for the SVs. For this reason, a MC value of 89% at room temperature is especially remarkable, as in many cases the leakage current is too high to even permit any sizable magnetic effect at room temperature [3,5,6,8–10].

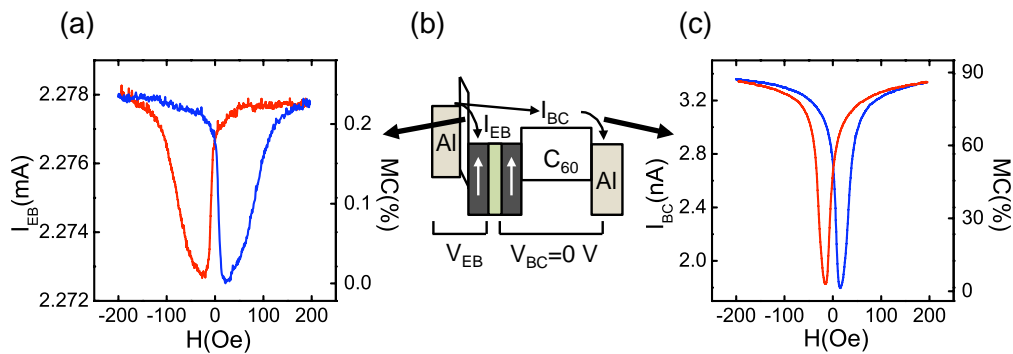


Figure 5.5. Magnetocurrent measured in the emitter base terminal (a) and in the collector (c). The picture in (b) shows how the voltages are applied.

Comparing figure 5.5 (a) and (c), one realizes that not only the magnitude of MC is different, but also the shape; in particular, the resistance of the P state is recovered at higher magnetic fields in figure 5.5 (a). In fact, the physical mechanisms at the basis of the magnetoresistive effect is subtly different in the two cases. In the case of the metallic SV base, the variation of the current is the result of different (spin dependent) scattering events that involve electrons at the Fermi level in the P and AP state [20]. In the case of the collected current, the variation is due to the different energy attenuation of the hot electrons in the magnetic layers.

I highlight here that the injection of hot electrons through ferromagnetic layers is one of the most successful methods to inject highly-spin-polarized current into semiconductors [21,22]. Under the assumption of a perfect spin filtering and no leakage current, the hot-electron current entering the semiconductor is 100% spin-polarized (see fig. 5.1(b)). In our devices, considering the relatively low value of  $I_{ap}$ , we expect a high spin polarization of  $I_{BC}$  entering the  $C_{60}$  layer. However, in order to verify whether the spin polarization is maintained across the  $C_{60}$  layer, a different device geometry would be necessary [22].

The dependence of MC with the emitter-base bias voltage is shown in figure 5.6 (a). In agreement with the I-V measurements (fig. 5.3 (c)), no hot-electron MC is recorded

in the C<sub>60</sub> collector for  $V_{EB} > 0$ . At negative voltages, the MC rises for  $V_{EB} < -1V$ , being  $V_{EB} = -1V$  the minimum bias needed to inject hot-electrons into the C<sub>60</sub>. The MC bias dependence is non-monotonic and the maximum value of 89% is reached at  $V_{EB} = -1.5V$ , while for more negative voltages the MC decreases. This behavior has been already observed in fully inorganic MTTs and has been successfully explained using a model based on spin-dependent inelastic scattering in the FM layers of the base [3].

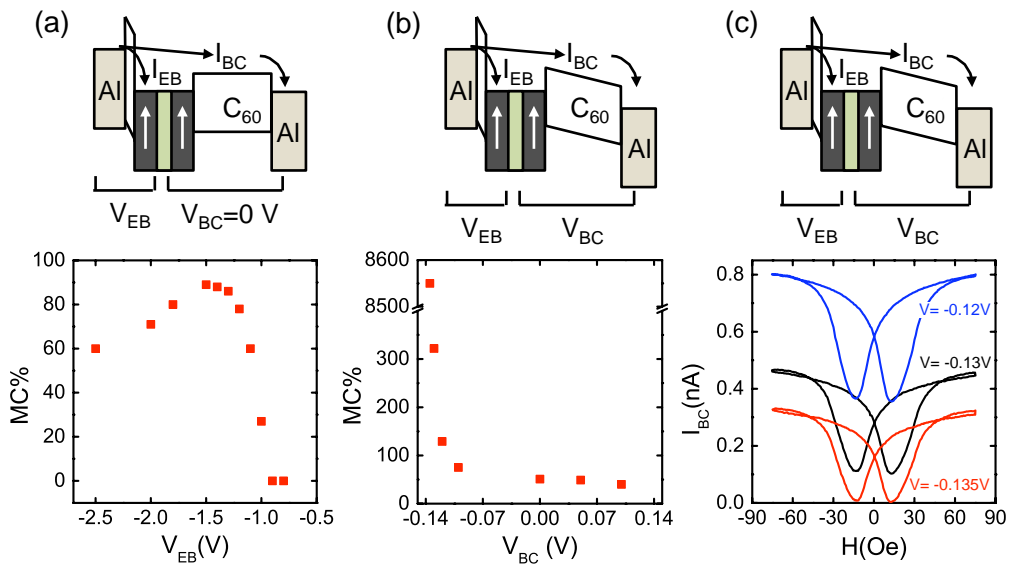


Figure 5.6. (a) Dependence of MC measured at the collector terminal with the emitter-base voltage  $V_{EB}$ , with fixed  $V_{BC} = 0V$ . (b) Dependence of the magnetocurrent with the base-collector voltage  $V_{BC}$  and fixed  $V_{EB} = -1.5V$  (c) Magnetocurrent curves for different  $V_{BC}$  values. The energy diagrams at the top illustrate how the voltages are applied at the different terminals.

Finally, we demonstrate that MC can be modulated by the application of a proper voltage between the base and the collector. The highest reported values of MC are measured at low temperatures when the leakage current flowing into the collector in the AP state is minimized [3,5–11]. In fact, at low temperatures the semiconductor resistance is extremely high, so that the leakage current  $I_L$  caused by the voltage spread is very low, as explained in the previous section. On the contrary, the hot electron current does not change much with the temperature [22]. Therefore, lowering the temperature is a way to get rid of the leakage current and keep only the hot electron current, as further discussed in section 5.3.2.

## 5.2 Device characterization

---

We show that a similar outcome can be obtained at room temperature by applying a base-collector voltage  $V_{BC}$ . Fig. 5.6 (b) shows the MC change by varying  $V_{BC}$  while keeping  $V_{EB}$  constant. In the device shown in fig. 5.6 (b), we measured 50% MC with  $V_{BC}=0$  V. By setting  $V_{BC}\neq 0$  V, an additional current contribution flows between the base and the collector. In the case of  $V_{BC}>0$  (i.e., accelerating the electrons in the  $C_{60}$  layer), the current reaching the collector increases because some electrons enter the  $C_{60}$  directly from the base. However, since the  $C_{60}$  resistance is not extremely high, a current driven by  $V_{BC}$  flows from the base and the collector with no hot origin. This current does not actually improve the MC as it just adds to the leakage current, effectively lowering the MC ratio (Fig. 5.6(c),  $V_{BC}>0$ ). In the case of  $V_{BC}<0$ , the current in the AP state ( $I_{ap}$ ) shifts towards zero (fig. 5.6 (c)). As a consequence, the MC increases to values higher than 50% (fig. 5.6 (b),  $V_{BC}<0$ ). In that way, the MC curve can be arbitrarily displaced choosing the right  $V_{BC}$  value. In Fig. 5.6 (c), we show how the MC curves evolve for three different selected  $V_{BC}$ ; the red curve corresponding to  $V_{BC}=-0.135$  V has very low current in the AP state, giving rise to extremely high MC (8550%).

## 5.3 Effects of external parameters

### 5.3.1 Temperature dependence

The temperature evolution of the I-V traces of a device similar to that described in the previous section is shown in figure 5.8. The device is composed by the following stack: Al(15 nm)/  $AlO_x$  / Co(4 nm) / Cu(4 nm) / Py(4nm) /  $C_{60}$ (200 nm) / Al(15 nm). The TJ resistance increases when lowering the temperature from 280K to 130 K (figure 5.8 (a)). The variation is small (<10 %), as expected for TJs with continuous insulating barriers [23]. On the contrary, the current flowing into the  $C_{60}$  measured at two terminals decreases dramatically when lowering the temperature (figure 5.8 (c)). Such a behavior is typical of semiconductors in general, and of organic semiconductor in particular [17].

Figure 5.8 (c) shows the temperature evolution of  $I_{BC}$  versus  $V_{EB}$ . Following the discussion in the previous section, for  $V_{EB} > 0$  V,  $I_{EB}$  is the leakage current, while for  $V_{EB} < 0$  V, it is the hot electron current. The spurious voltage spread  $V_L$  that causes the leakage current (see figure 5.4) is roughly constant in the whole temperature range,

because it is due to the current  $I_{EB}$ , which has minor temperature dependence. In turn, the leakage current  $I_L$  depends on  $V_L$  and on the resistance of the C<sub>60</sub>, which increases exponentially at low temperatures. Therefore, the leakage current decreases rapidly when lowering the temperature, following the increase in the C<sub>60</sub> resistance.

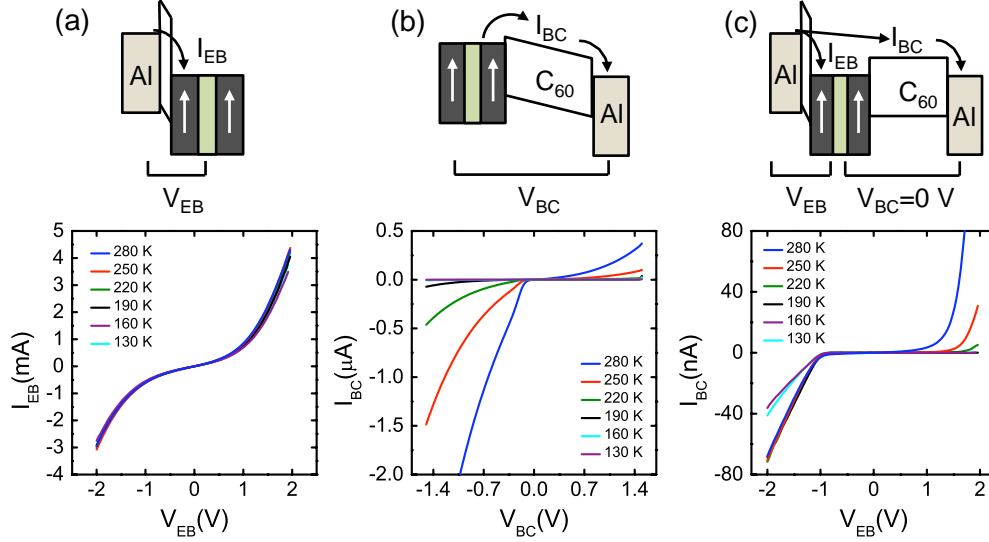


Figure 5.7. Temperature dependence of the I-V traces of (a) the Emitter-Base tunnel junction, (b) the C<sub>60</sub> layer, (c) the hot electron current and the leakage current.

For  $V_{EB} < 0$  V,  $I_{BC}$  does not change significantly in the temperature range 280 K – 190 K. This behavior demonstrates that all the current in this voltage region is hot-electron current, as any additional leakage current would decrease following the C<sub>60</sub> resistance increase, as for  $V_{EB} > 0$  V. The temperature dependence of  $I_{EB}$  can be therefore used to distinguish between the hot electron current and the leakage current. At some point, even the hot electron current begins to decrease. Probably the C<sub>60</sub> mobility becomes so low that electrons get trapped into it and cannot reach the Al top contact. In this case, the current begins to flow into the C<sub>60</sub> layer at  $V_{EB} = -0.9$  V, so that the barrier height is slightly different from the device described in the previous section. A possible explanation for this irreproducibility is given in the next section.

Figure 5.9 (a) and (b) shows the MC of the device of figure 5.7 measured at 280 K (a) and 130 K (b) with a bias voltage  $V_{EB} = -1.5$  V. Again, it is clear that at this voltage the contribution of the leakage current is small compared to the hot electron current. At 280 K, MC=85 %, on top of  $I_{BC} = 34$  nA (figure 5.9 (a)). Such a MC trace remains very similar for measurements between 280 K and 190 K. Below 190 K, the hot electron

### 5.3 Effect of external parameters

current begins to decrease (see also figure 5.9 (c)), and MC becomes similar to figure 5.9 (b). Once more, the reason for which the current in the AP state is not exactly 0 is that a complete AP state is not achieved. The leakage current mentioned previously has a minor role at  $V_{EB} = -1.5$  V. This is clearly shown in figure 5.9 (c), where the temperature dependence of MC at  $V_{EB} = -1.5$  V is shown in black dots. If the current in the AP state were due to the leakage current, then it would rapidly go to 0, and MC would increase to extremely high values. Instead, the MC increases from the 85 % at 280 K to just above 115 % at 190 K. This slight increase in MC is probably due to a better achievement of the AP state, because at low temperatures the coercive fields of the FM metals increase and become more separated.

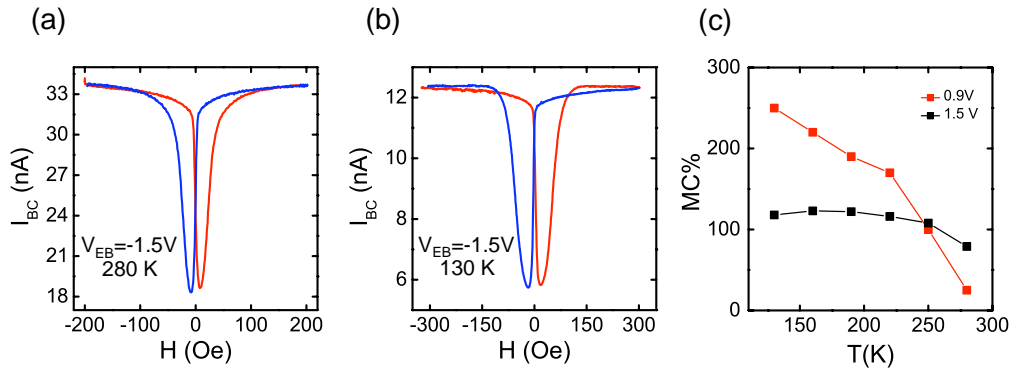


Figure 5.8. MC measured with  $V_{EB} = -1.5$  V at 280 K (a) and 130 K (b). The temperature dependence of MC is shown in (c) for a bias  $V_{EB} = -1.5$  V and  $V_{EB} = -0.9$  V.

The behavior of MC measured at  $V_{EB} = -0.9$  V is very different, and it is shown in red dots in figure 5.9 (c). At 280 K, MC is around 25%. I want to highlight that in the device described in the previous section no MC could be measured at  $V_{EB} = -0.9$  V, because in that case it was measurable from -1 V. This further confirms that the energy barrier at the metal/ $C_{60}$  interface was different in the 2 cases. Interestingly, MC keeps on rising when lowering the temperature, getting to above 240% at 130 K. Such a behavior could be due to a slight variation of the barrier height with the temperature. Indeed, MC measured at -0.9 V is extremely sensitive to even tiny changes in the barrier height, because it is just above the barrier, where the MC is steeply rising (see figure 5.6 (a)). However, other effects cannot be ruled out, and further work in this direction is necessary.

### 5.3.2 Dependence on the evaporator base pressure

As already mentioned in the previous section, in different devices the barrier heights at the Py/C<sub>60</sub> interface are found to be different. For example, in the device of figure 5.3 the barrier height is 1 eV; in the device of figure 5.7 it is 0.9 eV. In general, the barrier height is found to vary between 0.7 and 1.0 eV. In this section, I show that the barrier at the Py/C<sub>60</sub> interface is strongly affected by the formation of an oxide layer at the Py surface. The reactions between the Py surface and the residual oxygen in the chamber are likely to account for the differences measured in the various devices.

For investigating the effect of an oxidized Py surface on the device characteristics, a MTT is employed with a base composed only by a Py layer instead of a SV trilayer. The device is composed by the following stack: Al(15 nm)/ AlO<sub>x</sub> / Py(7nm) / C<sub>60</sub>(200 nm) / Al(15 nm), and is fabricated as follows. First, the emitter (Al layer) is deposited and plasma oxidized, following the optimized recipe described in the previous sections. Then, a 7-nm-thick Py base is deposited through shadow masks only onto two emitters, leaving the other emitter without base. At this stage, the device is exposed to an oxygen pressure  $p=10^{-1}$  mbar for two minutes without plasma, with the purpose of oxidizing the two Py bases. Afterwards, another 7-nm-thick Py layer is deposited only onto the emitters that are left without base during the first Py deposition. The 200-nm-thick C<sub>60</sub> layer is then deposited onto two oxidized and two fresh Py surfaces in the same chip. The devices are terminated with the deposition of the top Al electrode at the same time on all the devices.

Figure 5.9 (a) shows the I-V traces measured across the C<sub>60</sub> layer in a device with an oxidized interface (red trace) and with a clean interface (blue trace), both kept at 245 K. The current flowing in the device with the oxidized Py is several orders of magnitude higher than the current in the device with the clean Py/C<sub>60</sub> interface at positive V<sub>BC</sub>. A zoom of the low current part of the same figure is shown in panel 5.7 (b). The IV trace of the device with the clean interface has the diode-like shape similar to that found in the MTTs shown in the previous section (compare for instance fig. 5.7 (b) and the blue line in 5.9 (b)). The device with the oxidized Py surface has a completely different behavior. The current I<sub>BC</sub> flowing into the C<sub>60</sub> layer is extremely high at positive V<sub>BC</sub>. With the conventions used in this thesis, the positive polarity corresponds to the injection of electrons into C<sub>60</sub> by the Py contact. Therefore, the comparison between the IV traces shows that the barrier for electron injection at the oxidized Py/C<sub>60</sub> interface is much lower than the barrier at the clean one. On the contrary, the current at negative V<sub>BC</sub> does not change drastically in the two devices. In fact, this polarity

### 5.3 Effect of external parameters

corresponds to injection of electrons by the top Al contact, which has the same interface with the  $C_{60}$  film in the two devices.

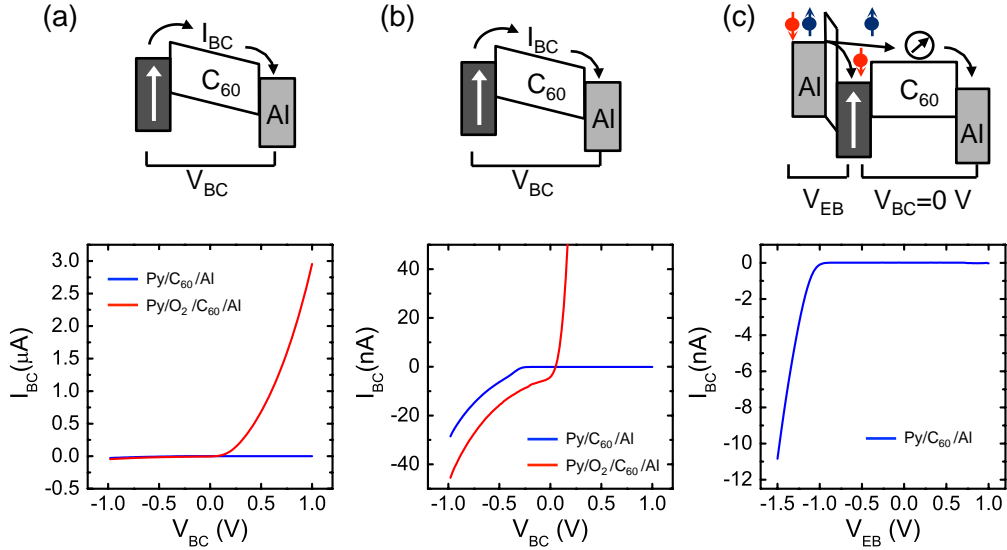


Figure 5.9. Comparison between the IV traces of a device with oxidized or with clean Py surface at 245 K. (a) IV trace across the  $C_{60}$  film; (b) zoom of (a) in the region of low current; (c) the hot electron current flowing in the device with the clean interface. The red (blue) curve refers to the sample with the oxidized (clean) surface.

The hot electron current for the clean Py/ $C_{60}$  interface is shown in figure 5.9 (c). In this case, the current begins to enter the  $C_{60}$  layer at roughly 0.95 V, which is the barrier height at this interface similar to the devices of fig. 5.3 and 5.7. It was not possible to measure the barrier height at the oxidized Py/ $C_{60}$  interface. The reason is that the resistance of the  $C_{60}$  layer is several orders of magnitude lower than the device with the clean interface. For the discussion in section 5.3.1, the low resistance of  $C_{60}$  introduces a high leakage current that hides the real hot electron current.

Being the barrier height so sensitive to the Py oxidation, we ascribe the differences in the barrier height measured in different devices to a different degree of oxidation of the Py surface. Ideally, the cleanest surface possesses the highest barrier height, which we could refer to as the “clean” Py/ $C_{60}$  barrier height. Given our data, such clean barrier height might be estimated around 1 eV. A partially oxidized Py surface results in lowering the barrier height. The Py surface can indeed react with the residual oxygen in the chamber, and the degree of oxidation depends on the amount of oxygen in the chamber, i.e. on the base pressure. Furthermore, other parameters influence the Py

oxidation, such as the wait time between the deposition of Py and the C<sub>60</sub> layer, during which the Py is exposed to the base pressure. Therefore, the irreproducibility in the barrier height is intrinsic in the fabrication procedure, because it is rather difficult to keep controlled all the possible parameters that might affect the Py oxidation.

The reason for which the oxidized surface has a much lower barrier height compared to the clean surface is not surprising. Spectroscopy measurements have shown that strong reactions occur at the interface between C<sub>60</sub> and 3d FM films [24], because of the reactivity of the clean metal surface. The reactions create an interface dipole that effectively behaves as a Schottky barrier. On the contrary, the oxidized surface is less reactive, so the position of the molecular levels with respect to the Fermi energy of the electrode is defined by the vacuum level alignment. A similar behavior has been observed in contaminated vs clean surfaces of gold and silver [15]. Further work is necessary to deeply understand the details of the reactions at the Py/C<sub>60</sub> interface, and the metal base transistor might be a useful instrument for this investigation.

### 5.3.3 Bias and light dependence

Figure 5.10 shows the effect of bias voltage  $V_{BC}$  and illumination on the device electrical and magnetic properties. For this study, we made our measurements at 200 K. At this temperature, the C<sub>60</sub> layer is already very resistive ( $R > 1 \text{ G}\Omega$ ), so the leakage current is negligible. The usual  $I_{BC}(V_{EB})$  is shown in black in figure 5.10 (a). The hot electron current begins to enter the C<sub>60</sub> layer at  $V_{EB} = -0.7 \text{ V}$ , which is the value of the barrier for injection in this case. The hot electron current getting to the top Al contact is rather low compared with the two samples discussed in the previous section. When a bias voltage  $V_{BC} = 0.2 \text{ V}$  is applied at the base-collector to accelerate the electrons towards the Al top contact, the hot electron roughly current doubles (blue lines in figure 5.10 (a)). In section 5.3.1, I pointed out that the extra current introduced by such a potential is a leakage current not due to hot electrons. That was the case at room temperature, when the C<sub>60</sub> layer has a lower resistance and  $V_{BC}$  introduces a sizable non-hot  $I_{BC}$ . At low temperatures, the C<sub>60</sub> resistance is so high that  $V_{BC} = 0.2 \text{ V}$  introduces a current  $I_{BC} < 1 \text{ nA}$ . The extra current introduced by  $V_{BC}$  in this case is mainly a hot electron current.

We have also noticed that the current flowing in the device is increased when the device is illuminated with a light source placed 30 cm far from the sample. The effect of the external light is the red curve in 5.10 (a).  $I_{BC}$  increases for both  $V_{EB} > 0$  and  $V_{EB} < 0$ . Moreover, at  $V_{EB} = 0 \text{ V}$  there is a non-zero current flowing into the C<sub>60</sub>. This current is

### 5.3 Effect of external parameters

due to photo-generated carriers that move under the influence of an internal electric field. Indeed,  $C_{60}$  is known to be sensitive to light and is often used in organic photovoltaic cells [25]. The combined effect of light and the bias  $V_{BC}=0.2V$  is the green line in figure 5.10 (a). The current at  $V_{EB}>0V$  is clearly positive, indicating that a leakage current is indeed flowing in the device.  $I_{BC}$  is actually much amplified in all the voltage range, and it is difficult to distinguish the leakage current and the hot electron current by just looking at the IV characteristics.

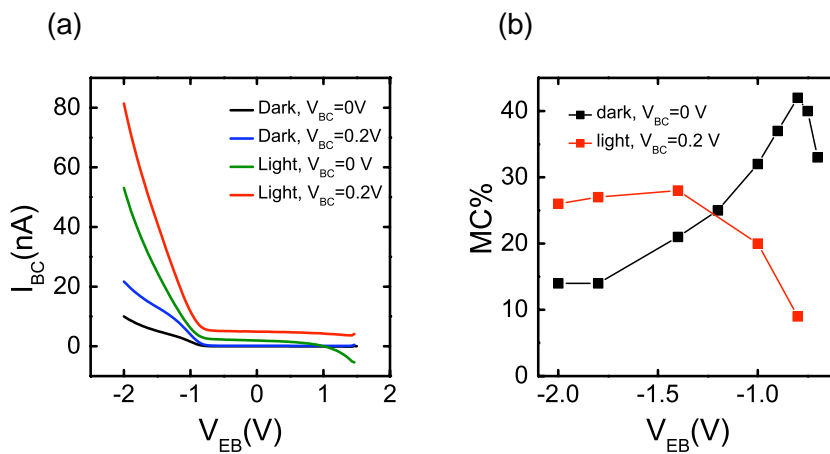


Figure 5.10. (a)  $I_{BC}(V_{EB})$  measured in dark, with  $V_{BC}=0V$  (black line), in dark with  $V_{BC}=0.2V$  (blue line), under illumination with  $V_{BC}=0V$  (green line), under illumination with  $V_{BC}=0.2V$  (red line). (b) MC dependence on  $V_{EB}$  for the device measured in dark with  $V_{BC}=0V$  (black dots) and under illumination and  $V_{BC}=0.2V$  (red dots). Measurements carried out at 200 K.

The variation of MC with the voltage  $V_{EB}$  is shown in 5.9 (b). In dark and with  $V_{BC}=0V$  (red dots), MC is lower than the MC of the devices described in the previous section, probably again because of the not complete AP state. The behavior of MC measured in this condition is similar to that of figure 5.6 (a), with a peak at  $V_{EB}=0.9V$ . The difference is that, in this case, MC is measurable from 0.7 V, as expected by the electrical characterization. The arguments of section 5.3.2 hold for accounting this difference. MC measured with  $V_{BC}=0.2V$  and under illumination is shown in black. In this case, at voltages just above the barrier height, MC is diminished compared with the MC measured in dark and with  $V_{BC}=0V$ . This means that the extra current introduced in this case is mainly leakage current. Interestingly, at higher  $V_{EB}$  biases, MC measured under illumination and with  $V_{BC}=0.2V$  is higher than the corresponding dark value. For instance, at  $V_{EB}=-2V$  in dark one measures  $MC=15\%$  with a low hot-electron current

$I_{BC}=10\text{nA}$  (figure 5.10 (a)); with light and  $V_{BC}=0.2\text{V}$  it becomes 25% on top of 100 nA. Therefore, at this high bias, the extra current is mainly hot electron current. In this sense, the effect of bias and light is to enhance the collector current  $I_{BC}$  while keeping its hot electron origin, at least at high bias. This effect can be useful for applications, where not only the MC value matters but also the current intensity.

## 5.4 Conclusions

In this chapter, the realization of a magnetic tunnel transistor employing C<sub>60</sub> as semiconducting layer has been demonstrated, with performances comparable to conventional inorganic MTTs. We have recorded a zero-collector-bias magnetocurrent of 89% at room temperature, which can be increased to any arbitrary value by applying a voltage at the collector terminal. The device geometry allowed us the determination of the energy barrier at the NiFe/C<sub>60</sub> interface, which varies in the range between 0.7 eV - 1 eV in different devices depending on the oxidation of the Py base. The temperature dependence of the electrical characteristics can be used to distinguish between hot electron current and leakage current.

We expect our results to be reproduced by other molecular semiconductors, opening novel pathways for the development of organic spintronics.

## 5.5 References

- [1] S. M. Sze and K. K. Ng, *Physics of Semiconductor Devices*, Third edit (2007).
- [2] R. Jansen, *Journal of Physics D: Applied Physics* **36**, R289 (2003).
- [3] S. van Dijken, X. Jiang, and S. Parkin, *Physical Review Letters* **90**, 4 (2003).
- [4] J. C. Grobli, D. Oberli, and F. Meier, *Physical Review B* **52**, R13095 (1995).
- [5] S. van Dijken, X. Jiang, and S. S. P. Parkin, *Applied Physics Letters* **83**, 951 (2003).
- [6] D. J. Monsma, J. C. Lodder, T. J. A. Popma, and B. Dieny, *Physical Review Letters* **74**, 5260 (1995).

## 5.5 References

---

- [7] R. Jansen, P. S. Anil Kumar, O. M. van't Erve, R. Vlutters, P. de Haan, and J. C. Lodder, *Physical Review Letters* **85**, 3277 (2000).
- [8] S. van Dijken, X. Jiang, and S. S. P. Parkin, *Journal of Applied Physics* **97**, 043712 (2005).
- [9] B. G. Park, E. Haq, T. Banerjee, B. C. Min, J. C. Lodder, and R. Jansen, *Journal of Applied Physics* **99**, 08S703 (2006).
- [10] T. Nagahama, H. Saito, and S. Yuasa, *Applied Physics Letters* **96**, 112509 (2010).
- [11] B. Park, T. Banerjee, J. Lodder, and R. Jansen, *Physical Review Letters* **99**, 217206 (2007).
- [12] M. S. Meruvia, I. a. Hummelgen, M. L. Sartorelli, a. a. Pasa, and W. Schwarzacher, *Applied Physics Letters* **84**, 3978 (2004).
- [13] M. S. Meruvia, M. L. Munford, I. A. Hummelgen, a. S. da Rocha, M. L. Sartorelli, A. A. Pasa, W. Schwarzacher, and M. Bonfim, *Journal of Applied Physics* **97**, 026102 (2005).
- [14] M. S. Meruvia and I. a. Hümmelgen, *Advanced Functional Materials* **16**, 459 (2006).
- [15] J. Hwang, A. Wan, and A. Kahn, *Materials Science and Engineering: R: Reports* **64**, 1 (2009).
- [16] X. Crispin, V. Geskin, A. Crispin, J. Comil, R. Lazzaroni, W. R. Salaneck, and J.-L. Brédas, *Journal of the American Chemical Society* **124**, 8131 (2002).
- [17] M. Baldo and S. Forrest, *Physical Review B* **64**, 085201 (2001).
- [18] L. Ma, J. Ouyang, and Y. Yang, *Applied Physics Letters* **84**, 4786 (2004).
- [19] C. D. Dimitrakopoulos and P. R. L. Malenfant, *Advanced Materials* **14**, 99 (2002).
- [20] T. Valet and A. Fert, *Physical Review B* **48**, 7099 (1993).
- [21] X. Jiang, R. Wang, S. van Dijken, R. Shelby, R. Macfarlane, G. Solomon, J. Harris, and S. Parkin, *Physical Review Letters* **90**, 25 (2003).
- [22] I. Appelbaum, B. Huang, and D. J. Monsma, *Nature* **447**, 295 (2007).
- [23] J. J. Akerman, R. Escudero, C. Leighton, S. Kim, D. A. Rabson, R. Whig, J. M. Slaughter, and I. K. Schuller, *Journal of Magnetism and Magnetic Materials* **34**, 86 (2002).
- [24] T. L. a. Tran, P. K. J. Wong, M. P. de Jong, W. G. van der Wiel, Y. Q. Zhan, and M. Fahlman, *Applied Physics Letters* **98**, 222505 (2011).
- [25] P. Peumans and S. R. Forrest, *Applied Physics Letters* **79**, 126 (2001).

## Chapter 6

# Beyond the spin valve structure

*In this chapter I summarize some recent results, highlighting the guidelines of the research of my last year of PhD. As I comment in section 1, the simple spin valve structure of chapter 4 has some limitations for the study of spin transport in  $C_{60}$ . In section 2, I explain why another structure based on the tunnel transistor of chapter 5 might allow further spin manipulation, and I present some partial results towards its fabrication.*

### 6.1 Limitation of the spin valve structure

The vertical spin-valve geometry described in chapter 4 is by far the most employed in spintronics based on molecular layers (see for instance ref [1–9]). The advantages of this geometry principally lie in its simplicity and universality. Indeed, it is the easiest conceivable device capable of providing information on the spin transport in almost all class of materials (see chapter 1). Furthermore, its wide range of application makes it attractive from the technological point of view, and any improvement in the figures of merit might find immediate impact in the market.

In particular, for the case of organic and molecular spintronics, this geometry presents two main advantages. First, it is extremely sensitive on the details of the interface between the ferromagnetic and the non-magnetic layer. In the case of molecules, this sensitivity can be exploited to study the influence of surface effects (such as hybridization and energy level shift) on the device characteristics [5,10]. Second, in the vertical spin valve geometry the magnetoresistance effect can be coupled to other effects, intrinsic to the organic interlayer, such as the electrical bistability [6,11,12] or the light emission [13,14]. However, other properties of the simple spin valve structure are not ideal for the study of spin transport in organic semiconductors. Two main issues about organic spin valves are matter of debate in the spintronic community.

## 6.1 Limitation of the spin-valve structure

---

First, the problem of the conductivity mismatch discussed in section 1.2.3 for inorganic semiconductor should in principle also apply to organics, because they are also characterized by a much higher resistivity than common FM metals. Therefore, magnetoresistance would only be expected when a thin organic layer behaves as a tunneling barrier. In fact, in most cases the transport through the organic is described in a multistep tunneling framework [3,5,7,15,16], as in this thesis, so that the organic layer thickness is limited at most to a few tens of nanometers. However, vertical spin valves have been also reported with the organic layer thickness above 100 nm, hence far from a tunneling regime [2,4,6], where magnetoresistance would *not* be expected. For this reason, it is debated whether the results obtained in organic spin valves can be described with the standard model of spin injection, transport and detection.

Second, the temperature dependence of the resistance in most reported organic spin-valves is weak [1–9,11,12,14–16], even when the organic layer thickness is far above the tunneling regime [2,4,6]. On the contrary, an exponential increase of the resistance of organic layers at low temperatures is expected and observed in the great majority of other devices based on organics (see [17] for a model of transport in organics). No formal explanation has been proposed for solving this controversy, and a tunneling formalism has been used even for the thickest organic thicknesses [2,4,6]. This issue is very important, because the weak temperature dependence might also be caused by the penetration of the top metal contact into the organic. If the top metal penetrates deeply into the organic layer, it might form a metallic filament and eventually pinholes that could dominate the device resistance. Therefore, careful control experiments must be performed in order to avoid artifacts in organic spin valves (such as the reference junction in our devices).

A definitive proof of spin transport in the organic layer would be the electrical detection of spin precession around a perpendicular external field (Hanle effect), as explained in section 1.2.2. A neat experiment in which such precession is detected in an organic semiconductor has remained elusive. In fact, the simple spin valve geometry is not the most suitable for such experiments. The reason is explained with the help of figure 6.1, which shows the magnetoresistance measured at 80 K in one of our spin valves of chapter 4 (Co/AIO<sub>x</sub>/C<sub>60</sub>/Py, C<sub>60</sub> 25 nm thick). In (a), the spin valve is measured in the standard way; the resistance change is monitored during a sweep of an in-plane magnetic field. As usual, the parallel and antiparallel states are characterized by different resistances. In (b), the MR measurement is performed during a sweep of an out-of-plane magnetic field. In principle, this configuration would allow the observation of the Hanle precession. The magnetization of the electrodes remains in-plane even for small out-of-plane magnetic fields, thanks to the shape anisotropy. The electrons would be injected in the C<sub>60</sub> layer with an in-plane spin polarization, and they would precess around the

(perpendicular) out-of-plane field. In principle, a vertical magnetic field should not even cause the in-plane reversal of the magnetization of the electrodes. If the spin valve is in a P state at zero external field, one should measure the lowest resistance. When the vertical field is applied, the spins precess around it. During the precession, two effects take place: the direction of the majority spin rotates and the spin coherence is partially lost [18]. Because of these two effects, the resistance increases. If, on the contrary, the initial state is in the AP state, one should measure the maximum resistance at zero field, and then a decrease due to the Hanle precession. Both the resistance increase from the P state and the AP state should give rise to a resistance change with a variation that can be approximated by a Lorentzian curve at low field [19]. At high out-of-plane magnetic fields, the magnetizations are forced to align out-of-plane, and the electrons are injected with the spin parallel to the external field, so they do not precess around it anymore. The P state is recovered, with its resistance.

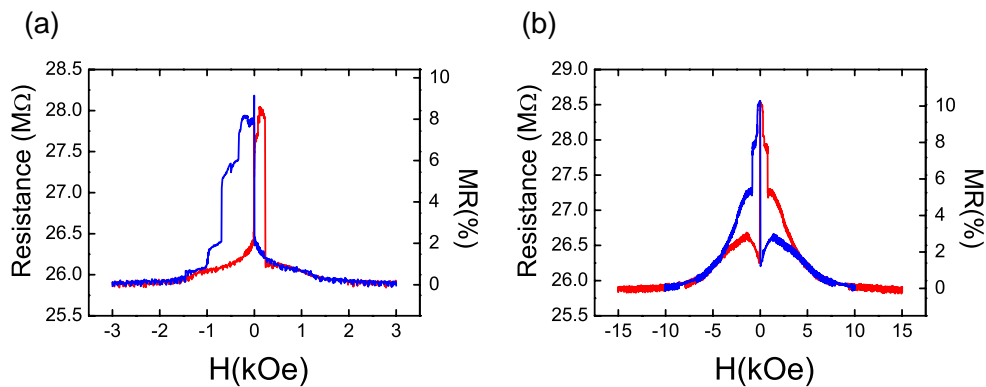


Figure 6.1. Magnetoresistance measured in a Co (15 nm)/AlO<sub>x</sub> (0.9 nm)/C<sub>60</sub> (25 nm)/Py (15 nm) spin valve. The measurements are performed in the same device, with the magnetic field swept in plane (a), or out-of-plane (b).

The actual measurement of the out of plane magnetoresistance is shown in figure 6.1 (b). First, we record steps in the MR at low fields. These steps are most probably due to a non-perfect out-of-plane alignment of the magnetic field, so that an in-plane component causes the electrode magnetization to switch in plane. Superimposed to it, a continuous resistance variation is measured both in the P and in the AP states. Such a variation might be fitted by a Lorentzian. Nevertheless, the Hanle precession is not the unique effect that might give rise to a similar signal. A simpler explanation is that the magnetization of the Py electrode is taken out of plane before the Co magnetization. The different resistance would be therefore due to different alignment of the top and bottom electrodes, from parallel in plane to slightly antiparallel out of plane. In

conclusion, it is difficult to separate the various contributions and get a neat Hanle precession signal with the simple spin valve geometry.

## 6.2 Towards the hot-electron spin valve

Following the works performed for inorganic semiconductors, one finds that there exist alternative ways for the electrical injection of spin polarized current into semiconductors. One of the most successful was already introduced in section 1.2.3, and is based on the magnetic tunnel transistor. As widely explained in section 5.1, if a thin metal layer is used as a base in a metal-base transistor, it acts as a spin filter (figure 6.2 (a)). The hot electron current entering the collector has a high spin-polarization due to the spin-dependent energy attenuation in the metal base. As a result, a highly spin-polarized current flows into a semiconductor, circumventing the conductivity mismatch problem. Moreover, the spin polarized current flows in the semiconductor through thicknesses well above the tunneling regime. A collector thickness above 200 nm can be employed, so that any artifact due to the metal penetration in the molecular layer can be avoided. Actually, I have already shown in section 5.3.1 that in this thickness range the resistance of the  $C_{60}$  increases exponentially when lowering the temperature.

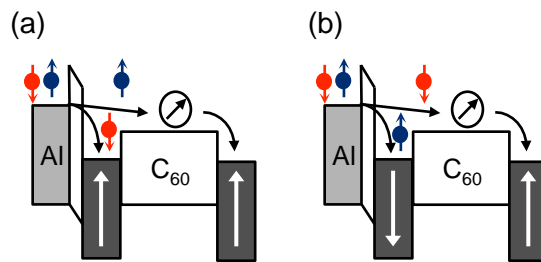


Figure 6.2. A magnetic tunnel transistor with a single ferromagnetic metal in the base and a second FM metal detector. The hot electron current entering the semiconductor is highly spin-polarized. The spin polarization changes with the magnetization of the base metal, but its magnitude does not.

The problem of this configuration is that the detection of the spin polarization is not trivial. Naively, one might think that a second ferromagnetic metal would be enough to measure a resistance difference, in analogy with the spin valve case (figure 6.2). However, there are subtle reasons that make the detection more complicated. First, the

spin polarization of the current depends on the direction of the magnetization of the FM metal base, but its intensity does not. The same current flows into the  $C_{60}$ , irrespective of the alignment of the magnetization of the two FM metals (see figure 6.2(a) and (b)). One might wonder if the resistance of the second FM metal itself would change depending on the different polarization of the incoming current, or if there would be some spin dependent scattering at the second semiconductor/FM metal interface, in analogy with what explained in section 1.2.2. However, those mechanisms hold for equilibrium current, i.e., for electrons with energy close to the Fermi level. In this case we deal with hot electrons, and the mechanisms explained in 1.2.2 at the basis of the MR effect might not directly apply to this case.

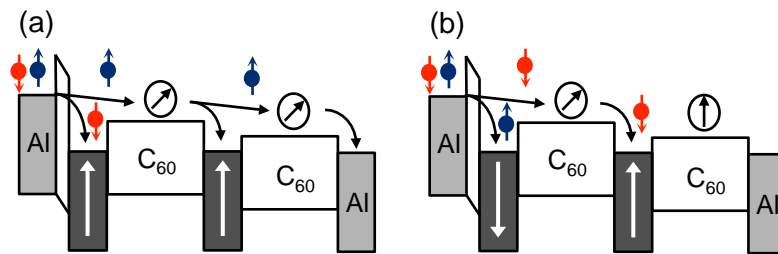


Figure 6.3. The injection and detection of spin-polarized current can be achieved by the series of 2 hot electron transistors. The hot electron current is injected by the Al contact, it becomes spin polarized in the first FM contact and reaches the second FM metal after travelling through the first  $C_{60}$  layer. This layer therefore acts as a collector for the first transistor and as a base for the second one. Assuming perfect spin filtering and spin coherence through the  $C_{60}$  layer, current only reaches the second collector when the two FM are in the P state.

As a matter of fact, no detection of spin polarization has been reported in a device similar to figure 6.2. Instead, an elegant way of detecting the spin polarization of the hot electron current was demonstrated by Appelbaum [20] in a more sophisticated device based on silicon. Figure 6.3 shows the energy alignment for its  $C_{60}$  counterpart. It is a vertical device with a tunnel junction at the bottom of a  $C_{60}$ /FM-metal/ $C_{60}$ /NM-metal stack on top. In such a device two ferromagnetic films act as the bases of two metal base transistors in series, so that the semiconductor collector of the first transistor ( $C_{60}$  in our case) becomes the emitter of the second one. In more detail, the electrical current injected by the first emitter (the tunnel junction) becomes spin polarized while crossing the first metal base. After travelling through the first  $C_{60}$  collector, it eventually gets to the second FM base retaining its spin coherence. At the second base, the current is injected above the metal Fermi level from the conduction band of the semiconductor.

For this reason, the electrons are again “hot” in the base, and a second spin filtering effect takes place. A fraction of the incoming current will reach the second collector only if magnetizations in the two bases are P (see figure 6.3 (a) and (b)). In this way, the *second* FM base in combination with the *second* semiconductor can be used to detect the spin polarization of the current flowing in the *first*  $C_{60}$  semiconductor.

In reference [20], the two semiconducting collectors are both Silicon. This detection scheme was extremely successful: spin coherence was demonstrated across long distances (through the whole 350  $\mu\text{m}$  thick silicon wafer in [21]) and also in lateral devices [22]. Furthermore, spin manipulation by the Hanle effect was demonstrated with unprecedented resolution [21]. In my last year of PhD, I explored the possibility of fabricating a double transistor device as the one in figure 6.3, with  $C_{60}$  instead of Silicon. Prior to the demonstration of the final device, some intermediate steps are necessary. The exact energy level alignment at the different  $C_{60}$ /metal interfaces must be precisely known. Indeed, the second FM base is sandwiched between two  $C_{60}$  layers, and hot-electron current will only flow if the injecting Schottky barrier is higher than the collecting one. Otherwise, hot electrons would be injected with energies above the Fermi level of the base, but not above the second energy barrier, so they would not penetrate into the second collector even in the P state. In Si, this requirement was fulfilled by employing a base composed by two metals (one of which FM) with different energy barriers at the interface with Si. For Si, the energy level alignment with various metals has been known for decades; for  $C_{60}$ , the matter is more complicated, and the level energy alignment must be characterized in different devices. Besides, one should make sure that the current reaching the second collector is high enough to be measurable. As already shown in chapter 5, the hot electron current intensity decreases exponentially in the FM layer, and in a few nanometers (8 nm) it gets attenuated by a factor of roughly  $10^{-5}$ . For having a measurable current after the second filter, a current of at least 100 nA should flow into the first semiconductor. With the transistors in chapter 5, this requirement was never fulfilled.

Finally, I would like to remark that the spin transport takes place in the first  $C_{60}$  layer of figure 5.3. The second semiconductor is only needed to increase the sensitivity of the detection, but in principle it can be any semiconductor, also Si. In fact, geometries different to the multilayer stack mentioned above can be considered. For instance, in another strategy a hot electron current could be injected from a top emitter into a  $C_{60}$  layer on a Si substrate; using the Si substrate as the second collector. In theory, this strategy is easier because one could take profit from the well-known energy level alignment at the metal/silicon interfaces. But, it is practically difficult to create a tunnel junction emitter on top of the thick and rough  $C_{60}$  layer; and the electrical insulation between the top electrodes and the bottom Silicon would also be problematic.

Whatever strategy is followed, the control of the energy level alignment at different metal/ $C_{60}$  interfaces is fundamental, as is the amount of current reaching the collector.

In the following part of the chapter, I describe some intermediate steps towards the fabrication of the structure in figure 6.3.

## 6.2.1 Permalloy base transistors

In this chapter, I describe a metal base transistor with the same geometry described in chapter 5, but with a single Py layer as base. The single Py layer base acts as a spin injector, and represents the first part of the structure in figure 6.3, as explained in the previous section. A scheme of the device is shown at the top of figure 6.4 (a). It is composed by the following stack: Al (15 nm)/AlOx/Py (6 nm)/ $C_{60}$  (200 nm)/ Al(20 nm). The details of the fabrication have been given in the chapter 5.

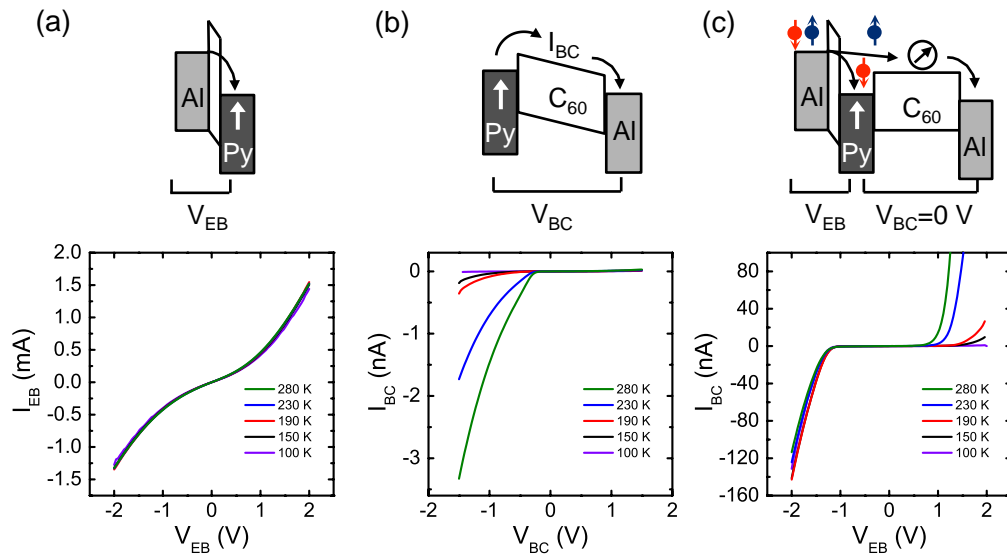


Figure 6.4. Electrical characterization of a metal base transistor with an Al emitter, a Py base and a  $C_{60}$  collector. I-V traces measured at different temperatures across the tunnel junction (a) and the  $C_{60}$  layer (b). (c) Hot-electron current  $I_{BC}$  measured at the collector terminal when the emitter-base voltage  $V_{EB}$  is swept and the base-collector voltage  $V_{BC}$  is kept at 0V.

The electrical characterization of the device at different temperatures is shown in figure 6.4. The current flowing in the tunnel junction is reproducibly in the range

between 1-5 mA at 2 V bias voltage, and does not vary much with the temperature (figure 6.4(a)). The resistance of the thick  $C_{60}$  layer increases exponentially when the temperature is lowered (figure 6.4(b)). The I-V traces are very asymmetric, similar to those shown in chapter 5. This similarity is expected, because here and in chapter 5 the  $C_{60}$  layer is sandwiched between the same two materials (Py and Al). The same argument holds for the description of the behavior of the hot electron current, shown in figure 6.4(c). At negative  $V_{EB}$ , the hot-electron current enters the  $C_{60}$  when the emitter bias is roughly above 1.0 V, that is the barrier height at the clean Py/ $C_{60}$  interface (see chapter 5). The hot electron current is roughly constant with the temperature between 100 K and 280 K. At positive  $V_{EB}$ , the leakage current is huge at 280 K, but it decreases rapidly and it becomes negligible at 100 K. Again, for these devices the temperature dependence for the hot electron current and the leakage current is very different. The origin of the leakage current  $I_L$  was already discussed in chapter 5; at low temperature,  $I_L$  is negligible because the resistance of the  $C_{60}$  layer becomes extremely high. One important difference is that the hot electron current in the device in figure 6.4 is higher than in the devices in chapter 5. The current is less attenuated in the base because the Py base is thinner than the spin valve base of chapter 5.

For the fabrication of the device in figure 6.3, not only a FM metal base is required, but also a FM top contact. In principle, one would expect that the top contact material had a minor role in the determination of the device performances. On the contrary, it is found that the device characteristics radically change when materials other than Al are employed as top electrode. Figure 6.5 shows  $I_{BC}(V_{EB})$  for two different devices with the same base (Py, 7 nm) and different top contact FM material: Co (a) and Py (b). The Co-top electrode device in (a) performs as a hot electron transistor: for  $V_{EB} > 0$  V, a leakage current flows in the device that becomes negligible below 220K; for  $V_{EB} < 0$  V, the current might be hot-electron current. Its temperature dependence is different from the temperature dependence of the leakage current. In this case the barrier height is 0.9 V, similar to the barrier height measured in other devices with a Py base. However, while the hot electron current for a device with an Al top electrode is roughly constant in a wide range of temperatures (from 280 K to 100 K in figure 6.4 (c)), in the device of figure 6.5 (a) it decreases more rapidly, and at 150 K becomes negligible.

The situation is even more different when a Py top electrode is employed. In this case (shown in figure 6.5(b)), the current reaching the collector is very low even at room temperature. In particular, at  $V_{EB} < 0$  V the current is below 150 pA. In addition, when  $V_{EB}$  is below the barrier height at the first Py/ $C_{60}$  interface, no current should arrive at the collector. Instead, in figure 6.5 (b), already at very low bias  $V_{EB} < 0$  V there is a detectable current flowing in  $C_{60}$  – the current possess a non-zero slope, while it should equally zero until a  $V_{EB}$  is above the Shottky barrier. For this reason, the current

flowing in  $C_{60}$  must be therefore a leakage current, possibly added to a real hot-electron current. Even at  $V_{EB} > 0V$ , the current is very low: this means that the  $C_{60}$  layer is extremely resistive even at room temperature. For the sample in figure 6.5(b), the temperature dependence has not been measured, because the current at room temperature was already too low to be used in any device.

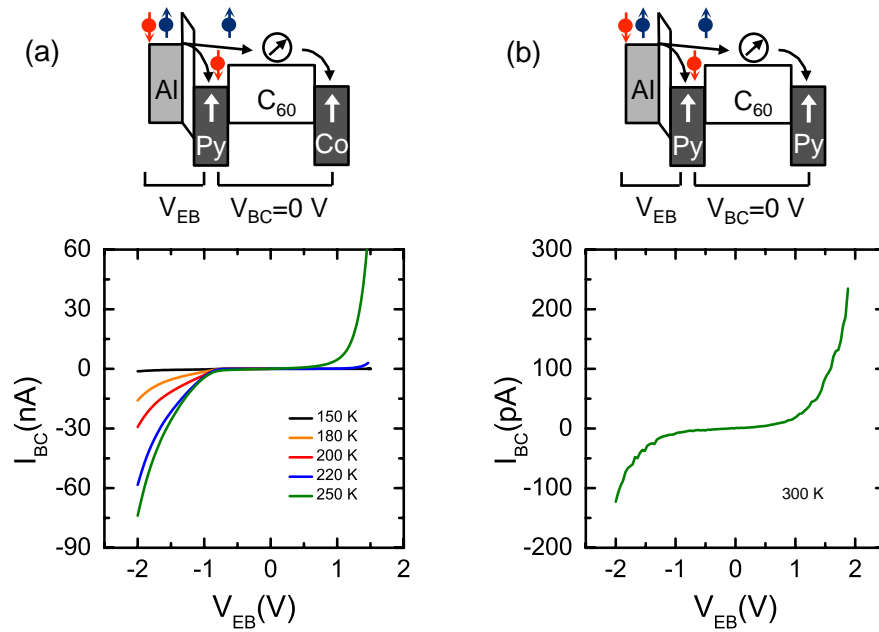


Figure 6.5. (a) Hot-electron current  $I_{BC}$  measured at the collector terminal when the emitter-base voltage  $V_{EB}$  is swept in transistors with Py base and different top electrodes: (a) Co top electrode, different temperatures; (b) Py top electrode, room temperature.

The reasons for such a change in the device characteristics when different top layers are employed is not fully understood, and represents the most challenging problem in the fabrication of the device in figure 6.3. As a final comment to the devices in figure 6.5, MC was measured for both samples in figure 6.5, but in both cases no signal was found – at least not higher than the noise level (roughly 0.2 % relative error in the two cases). Indeed, for such a configuration the absence of detectable MC was expected, as explained in the previous section.

Finally, I show that annealing a sample is a simple way for increasing the hot electron current. The test sample was a “normal” transistor with a 7-nm-thick Py base, a 200-nm-thick collector and an Al top contact. Figure 6.6 (a) and (b) shows a comparison between the transport characteristics of the same device before and after an annealing

process, measured at 150 K. First, the transport properties of the  $C_{60}$  layer itself change drastically. At 150 K, the current flowing before annealing is extremely low, almost below the detection limit (red line in figure 6.6(a)). After annealing at 200°C for one hour in vacuum ( $10^{-6}$  mbar), the current flowing into the  $C_{60}$  layer increases two orders of magnitude. Such an increase in the  $C_{60}$  conductivity upon annealing had already been observed [23]. In our case, we notice that the increased conductivity of  $C_{60}$  reflects into a higher hot electron current, as shown in figure 6.6(b). Before annealing, the hot electron current reaches  $I_{BC} = 50$  nA at  $V_{EB} = -2$  V and  $V_{BC} = 1$  V. After annealing, the hot electron current becomes  $I_{BC} = 225$  nA at  $V_{EB} = -2$  V and  $V_{BC} = 1$  V, being amplified for a factor 4.5. A 200 nA current in this  $C_{60}$  transistor is comparable to the current measured in Silicon in [20]. I highlight that the leakage current at the positive  $V_{EB}$  is negligible before and after annealing (see figure 6.6 (a) and (b)).

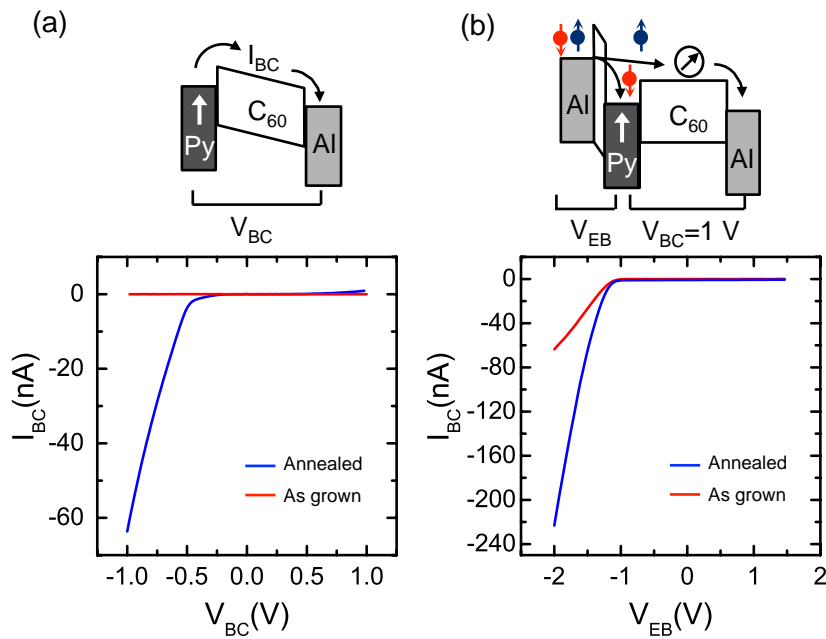


Figure 6.6. Py base transistor characteristics measured at 150 K. (a) IV trace across the 200-nm-thick  $C_{60}$  layer before and after annealing (red and blue curve, respectively). (b) Hot electron current before and after annealing, measured with a bias voltage  $V_{BC} = 1$  V.

## 6.2.2 Cobalt base transistor

For the fabrication of the device in figure 6.3, two FM metal/ $C_{60}$  spin-filters are necessary. The Py/ $C_{60}$  interface is suitable for the spin filtering effect, as shown in the previous section. The most obvious choice for the second spin filter would be the Co/ $C_{60}$  interface. In this final section, I show the transport properties of a Co base transistor. The device was analogous to the Py base transistors described in the previous section, but using a 7-nm-thick Co layer as base. Figure 6.7 shows a comparison with a Py-base transistor and a Co-base transistor. The devices behave very differently. The  $C_{60}$  conductivity is very different in the case of a Co and a Py injector. As can be clearly observed in figure 6.7 (a).

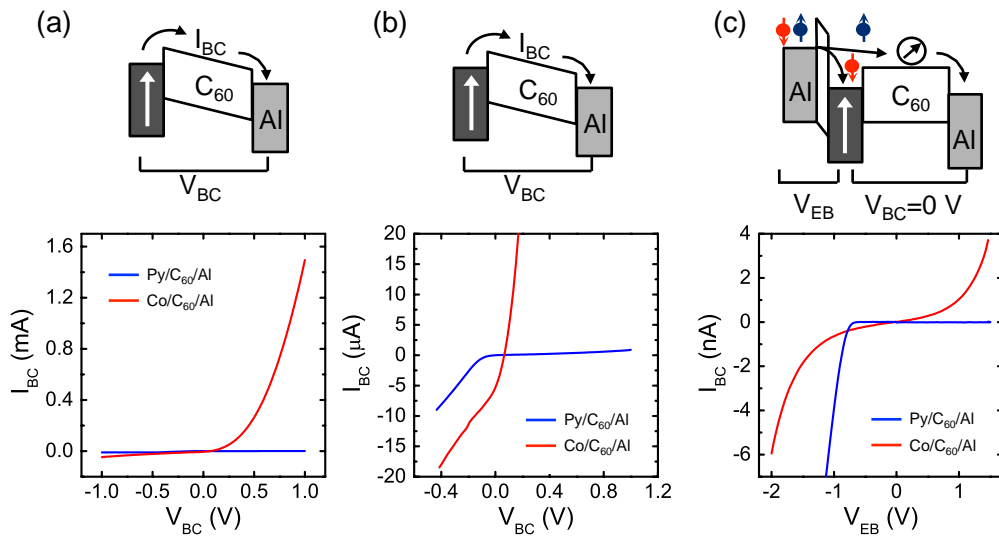


Figure 6.7. Comparison between a Co base transistor (red lines) and a Py base transistor (blue lines). (a)  $I$ - $V$  trace of  $C_{60}$  measured at 300 K; (b) zoom of (a) for the low current region. For  $V_{BC} < 0$  V, Al injects electrons into  $C_{60}$ ; for  $V_{BC} > 0$  V either Py or Co injects electrons. The big difference in the device characteristics is for  $V_{BC} > 0$  V. (c)  $I_{BC}(V_{EB})$  for the two transistors, measured at 150 K. For the Py base, the current begins to flow into  $C_{60}$  when  $V_{EB} < -0.9$  V, signature of hot electron current. For the Co base transistor such a behavior is not observed.

As a reminder, in the conventions used in this thesis positive polarity in the voltage  $V_{BC}$  corresponds to the bottom layer injecting the current (either Co or Py). At room temperature, the Co electrode injects 3 orders of magnitude more current than Py.

Figure 6.7 (b) is a zoom of figure 6.7 (a) at low current. In the negative polarity region  $V_{BC} < 0V$ , corresponding to the electron injection from Al, the current flowing in the device has the same order of magnitude for the two devices. Instead, in the positive region, an extremely high current flows even at small  $V_{BC}$  bias for the Co base device. This IV characteristic is extremely similar to that of the oxidized Py/ $C_{60}$ /Al described in section 5.3.2. Possibly, Co reacts with the residual oxygen in the chamber more than Py, so that we never deal with completely clean Co surfaces.

Figure 6.7 (c) shows the dependence of the collector current  $I_{BC}$  on the emitter-base voltage  $V_{EB}$  for the two devices measured at 150 K. For the Py base device, the current is zero when  $V_{EB}$  is below the barrier height at the Py/ $C_{60}$  interface, and then it begins to enter the  $C_{60}$  layer, as explained in the previous section (blue line). For the Co base transistor,  $I_{BC}(V_{EB})$  shows no evidences of hot electron current (red line). This behavior was encountered also for the oxidized Py transistor described in section 5.3.2. A non-zero current flows in the  $C_{60}$  even at low bias voltage  $V_{EB}$ , and a current with the same order of magnitude flows in both the positive and negative bias voltages, suggesting that all the measured current is a leakage current. Therefore, the barrier at the Co/ $C_{60}$  interface does *not* behave as a classical Schottky barrier, and Co *cannot* be used in a structure as in figure 6.3. In this sense, one might choose another FM electrode; Nickel might be a wise choice, because its surface reactivity is similar to Py but it possesses a different coercive field.

## 6.3 Conclusions

In this chapter, I explained why the simple vertical spin valve geometry is not the ideal structure for the measurement of spin diffusion lengths through thick  $C_{60}$  films, neither it is for spin manipulation. I have described a more sophisticated multilayer geometry that has been used for the electrical spin injection and detection in Silicon, highlighting some of its advantages. I have shown that in principle the same injection/detection scheme can be applied to  $C_{60}$ , and described the first partial steps towards the fabrication of the entire structure.

## 6.4 References:

- [1] V. A. Dediu, L. E. Hueso, I. Bergenti, and C. Taliani, *Nature Materials* **8**, 707 (2009).
- [2] Z. H. Xiong, D. Wu, Z. V. Vardeny, and J. Shi, *Nature* **427**, 821 (2004).
- [3] T. Santos, J. Lee, P. Migdal, I. Lekshmi, B. Satpati, and J. Moodera, *Physical Review Letters* **98**, 016601 (2007).
- [4] V. Dediu, L. Hueso, I. Bergenti, a. Riminucci, F. Borgatti, P. Graziosi, C. Newby, F. Casoli, M. De Jong, C. Taliani, and Y. Zhan, *Physical Review B* **78**, 115203 (2008).
- [5] C. Barraud, P. Seneor, R. Mattana, S. Fusil, K. Bouzehouane, C. Deranlot, P. Graziosi, L. Hueso, I. Bergenti, V. Dediu, F. Petroff, and A. Fert, *Nature Physics* **6**, 615 (2010).
- [6] M. Prezioso, A. Riminucci, I. Bergenti, P. Graziosi, D. Brunel, and V. a Dediu, *Advanced Materials (Deerfield Beach, Fla.)* **23**, 1371 (2011).
- [7] T. L. A. Tran, T. Q. Le, J. G. M. Sanderink, W. G. van der Wiel, and M. P. de Jong, *Advanced Functional Materials* **22**, 1180 (2012).
- [8] M. Galbiati, C. Barraud, S. Tatay, K. Bouzehouane, C. Deranlot, E. Jacquet, A. Fert, P. Seneor, R. Mattana, and F. Petroff, *Advanced Materials* **24** 6429 (2012).
- [9] K. V. Raman, A. M. Kamerbeek, A. Mukherjee, N. Atodiresei, T. K. Sen, P. Lazić, V. Caciuc, R. Michel, D. Stalke, S. K. Mandal, S. Blügel, M. Münzenberg, and J. S. Moodera, *Nature* **493**, 509 (2013).
- [10] S. Sanvito, *Nature Physics* **6**, 562 (2010).
- [11] L. E. Hueso, I. Bergenti, a. Riminucci, Y. Q. Zhan, and V. Dediu, *Advanced Materials* **19**, 2639 (2007).
- [12] M. Prezioso, A. Riminucci, P. Graziosi, I. Bergenti, R. Rakshit, R. Cecchini, A. Vianelli, F. Borgatti, N. Haag, M. Willis, A. J. Drew, W. P. Gillin, and V. a Dediu, *Advanced Materials* **25**, 534 (2013).
- [13] I. Bergenti, V. Dediu, E. Arisi, T. Mertelj, M. Murgia, a. Riminucci, G. Ruani, M. Solzi, and C. Taliani, *Organic Electronics* **5**, 309 (2004).
- [14] T. D. Nguyen, E. Ehrenfreund, and Z. V. Vardeny, *Science* **337**, 204 (2012).
- [15] J. Shim, K. Raman, Y. Park, T. Santos, G. Miao, B. Satpati, and J. Moodera, *Physical Review Letters* **100**, 226603 (2008).
- [16] J. Schoonus, P. Lumens, W. Wagemans, J. Kohlhepp, P. Bobbert, H. Swagten, and B. Koopmans, *Physical Review Letters* **103**, 146601 (2009).

## 6.4 References

---

- [17] M. Baldo and S. Forrest, *Physical Review B* **64**, 085201 (2001).
- [18] F. J. Jedema, H. B. Heersche, a T. Filip, J. J. a Baselmans, and B. J. van Wees, *Nature* **416**, 713 (2002).
- [19] S. P. Dash, S. Sharma, R. S. Patel, M. P. D. Jong, and R. Jansen, **462**, 491 (2009).
- [20] I. Appelbaum, B. Huang, and D. J. Monsma, *Nature* **447**, 295 (2007).
- [21] B. Huang, D. Monsma, and I. Appelbaum, *Physical Review Letters* **99**, 177209 (2007).
- [22] H. Jang and I. Appelbaum, *Physical Review Letters*, **103**, 117202 (2009).
- [23] L. Ma, J. Ouyang, and Y. Yang, *Applied Physics Letters* **84**, 4786 (2004).

## 7. List of publications

This thesis is based on the following publications:

1. "Room-Temperature Spin transport in C<sub>60</sub> based spin valve"  
M. Gobbi, F. Golmar, R. Llopis, F. Casanova, L. Hueso  
*Adv. Mater.* 23, 1609-1613 (2011)  
(chapter 4)
2. "Non-conventional metallic electrodes for organic field-effect transistors"  
M. Gobbi, A. Pascual, F. Golmar, R. Llopis, P. Vavassori, F. Casanova, L. Hueso  
*Org. Elec.* 13, 366-372 (2012)  
(chapter 3)
3. "C<sub>60</sub> based hot electron magnetic tunnel transistor"  
M. Gobbi, A. Bedoya-Pinto, F. Golmar, R. Llopis, F. Casanova, L. Hueso  
*Appl. Phys. Lett.* 101, 102404 (2012)  
(chapter 5)

Other publications:

"Non-conventional metallic electrodes for organic field-effect transistors"  
F. Golmar, M. Gobbi, R. Llopis, P. Stoliar, F. Casanova, L.E. Hueso  
*Org. Elec.* 13, 2301-2306 (2012)

"Electronic transport in sub- micron square area organic field-effect transistors"  
F. Golmar, P. Stoliar, M. Gobbi, F. Casanova, L.E. Hueso  
*Appl. Phys. Lett.* 102, 103301 (2013)



## 8. Acknowledgements

I would like to express my sincere gratitude to my supervisor Prof. Luis E. Hueso for his constant support and guidance. He has been able to keep me always motivated and content though the difficulties of experimental science. Indeed, that was not an easy task. I am particularly grateful for the liberty he granted me in conducting the research projects, always respecting my thoughts and giving me the chances to explore new ideas. I highly value his teachings about the importance of reading, studying and thinking. In great part, he taught me how to be a scientist.

This project would not have been possible without the other people of the NanoDevices group. In particular, I am extremely thankful to Prof. Felix Casanova, for the many stimulating discussion we had. I enjoyed very much working with him during these years. Almost all I know about metals comes from his side. He has always been open to give his advices and suggestions, being involved in my projects almost as a second supervisor.

Many thanks to Roger Llopis, the group technician. If Luis taught me how to think, Roger had to teach me how to screw, especially in the two first years of my PhD, when we were starting up the lab. He has been definitely more than a technician, and he deserved all the cookies I gave him.

To the post-docs of the group for their daily help. In particular, to Federico Golmar and Amilcar Bedoya Pinto, who have been with me from almost the beginning, discussing ideas or in experimenting in the lab. I had much to learn from the two of them (the Kirchoff law, for instance). Their support has been essential for the work presented in this thesis. To Xiangnan Sun, for the nice common projects we worked on in the relatively short period we have been together. And to David Ciudad, for being extremely nice in the time we spent together in the US.

To Oihana Txoperena, for listening to my suggestions and helping me in whatever she could. And to the other colleagues in the Nanodevices group: Estitxu, Miren, Mano, Luca, Mariana, Raul and Libe (in order of seat). Thanks for the nice atmosphere at work and (more importantly) thanks for the beers out of work.

## Acknowledgements

---

Outside my group, I have been collaborating with Thales de Oliveira, Prof. Paolo Vavassori and Pablo Stolar. I thank them for the effort they put in pushing forward the common projects.

I would like to thank Prof. Txema Pitarke for the opportunity to work and carry out my experiments at CIC nanoGUNE Consolider (Donostia). I also acknowledge the financing from CIC nanoGUNE during my PhD.

Greetings to all the people working in nanoGUNE for the nice atmosphere at work. To Marie, for the coffees she offered me. To Txema, for leading the “football tomorrow” crew. To the nanomag people (Olatz, Jon Ander, Ania, Juan) for peacefully sharing the same lab. To Donolato, for the nice time he spent here. And to everybody else, for making nanoGUNE such a nice place of work. I will miss it.

Thanks to all the friends that I met in the Basque Country, for making my years here so intense. I cannot name them all, it would be longer than the thesis.

Un ringraziamento enorme va alla mia famiglia, per essermi stata sempre vicino durante i miei anni lontano. Grazie alle mie sorelle Chiara, Laura e Serena, ai loro mariti Fabio, Ennio e Alberto, e ai piccoli Elia, Pietro, Martino e Diego per i momenti stupendi che passo ogni volta che torno in Italia. E specialmente, un grande ringraziamento a mio padre Gianmario, che mi è vicino ogni giorno, e non mi ha mai fatto sentire solo. E a mia madre, a cui sarebbe piaciuto tanto vedermi dottore.

A big hug to (Txipi) Maider, for making my last year here so beautiful. You make me so happy! I feel very lucky. Thank you for everything!!

Marco,  
February 2013